Measurement of the generalized polarizabilities of the proton by virtual Compton scattering at MAMI and $Q^2 = 0.2\ GeV^2$

Loup Correa

July 29, 2016

Abstract

This work presents the measurement of the generalized electric $\alpha_E(Q^2)$ and magnetic $\beta_M(Q^2)$ polarisabilities (GPs) of the proton. The GPs are defined in the Virtual Compton Scattering (VCS) context, i.e. the reaction $\gamma^* p \rightarrow \gamma p$, where Q^2 is the four-momentum transfer of the virtual photon. The GPs are a generalization of polarizabilities measured in real Compton scattering (RCS) by taking into account the Q^2-dependency. They are dynamical properties of the proton when it is deformed by an applied electromagnetic field. $\alpha_E(Q^2)$ (or $\beta_M(Q^2)$) gives access to the local polarization (or magnetization) density of the deformed proton. The studied VCS process is accessible by the photon-electroproduction reaction ($ep \rightarrow ep\gamma$). The GP effect is a $1-15\%$ contribution to the the $ep \rightarrow ep\gamma$ cross section, requiring a high-precision measurement.

The present work is a part of an experiment conducted by the A1 collaboration at MAMI. The goal is to extract the electric and magnetic GPs at three new Q^2 values: $0.1, 0.2$ and $0.45\ GeV^2$. This thesis details the extraction at $0.2\ GeV^2$. The experiment uses the $1\ GeV$ electron beam, the 5 mm liquid hydrogen target and spectrometers A (B) to detect the final electron (proton).

The first-level analysis includes a detailed calibration of experimental data, and the use of a simulation of the experiment. The measurement of the unpolarized $ep \rightarrow ep\gamma$ cross section is described with two of its important features: the correction of the radiative effects and the renormalization.

Two different frameworks are used to extract the GPs. The first one is based on the Low Energy Theorem (LET) and is model independent. The second one relies on the dispersion relation model (DR). The two extractions lead to results in good agreement. The world data still raises question about the Q^2-behavior of the GPs.

Keywords: electromagnetic probe, generalized polarizabilities, virtual Compton scattering, Hadron physics, proton structure, low energy expansion, dispersion relations.

Zusammenfassung

Diese Arbeit stellt die Messung der elektrische $\alpha_E(Q^2)$ und magnetische $\beta_M(Q^2)$ Generalisierte Polarisierbarkeiten (GPs) des Protons. Die GPs sind in der Virtuellen Comptonstreuung (VCS) Kontext definiert, das heißt die $\gamma^* p \to \gamma p$ Reaktion, und Q^2 ist das Quadrat des Viererimpulsübertrags des virtuellen Photons. Die GPs sind eine Ausweitung der Polarisierbarkeit in Reelle Comptonstreuung fur $Q^2 \neq 0$. Sie sind dynamische Eigenschaften des Protons in Antwort eines elektromagnetisches Feld. $\alpha_E(Q^2)$ ($\beta_M(Q^2)$) beschreibt die lokale Polarisation (Magnetisierungs) Dichte des verformten proton. Der studiert VCS Prozess ist durch die Photonenelectroproduction Reaktion ($ep \to ep\gamma$). Der GP-Effekt ist nur ein $1-15\%$ Beitrag zu das $ep \to ep\gamma$ Wirkungsquerschnit so daß hochgenaue Messungen nötig sind.

Der vorliegenden Arbeit ist ein Teil des "vcsq2" Experiments geführt an MAMI, durch die A1 Zusammenarbeit. vcsq2 Ziel ist, die elektrischen und magnetischen GPs für drei neue Q^2 Werte zu messen: $0.1, 0.2$ und 0.45 GeV^2. Diese Arbeit beschreibt die Extraktion für 0.2 GeV^2. Das Experiment verwendet die 1 GeV Elektronenstrahl, die 5 mm von flüssigem Wasserstoff Kryp-Target und Spektrometer A (B) das endgültige Elektron (Proton) zu detektieren. Die erste Ebene Analyse beinhaltet eine detaillierte Kalibrierung von experimentellen Daten, und die Verwendung einer Simulation des Experiments. Die Messung des unpolarisierten $ep \to ep\gamma$ Wirkungsquerschnitt ist mit zwei wichtigen Korrekturen: die Strahlungskorrektur und der Renormierung.

Zwei verschiedene Rehmen werden verwendet, um die GP heraus zu ziehen. Die erste stützt sich auf dem Low-Energy-Theorem (LET) und ist Modell unabhängig. Die zweite stützt sich auf die Dispersionsrelation Modell (DR). Die beiden Extraktionen führen zu Ergebnissen in guter Übereinstimmung. Die Welt Daten werfen noch Fragen zu den Q2 -Verhalten der GPs.

Contents

Introduction

In 1911 Ernest Rutherford discovered that the atoms have a heavy nucleus [1]. Ten years later he was able to perform the first artificial transmutation and by this way proved that these nuclei were composed of elementary bricks: the protons. Thereafter he even anticipated the existence of the neutron which was later discovered by Chadwick in 1932 [2].

One century after its discovery the proton is still under investigation, and nowadays it is the proton internal structure which is a source of questioning. We know that its structure is governed by the strong interaction but we have to face a dichotomy: the coupling constant of the strong interaction decreases at high energy and allows for an interpretation of the experiments in terms of perturbative Quantum ChromoDynamics (QCD), while at low energy, the coupling constant increases and asks for a description in terms of the hadronic degrees of freedom, such as Chiral Perturbation Theory.

In between, at excitation energies from ≈ 100 to ≈ 2000 MeV, both perturbation schemes are powerless to fully describe the proton interactions. This is the region of nucleon resonances which are still not described by a consensual theory. In order to improve our knowledge, it is therefore essential to precisely extract hadronic structure information. In this aim the Compton scattering experiments are precious tools.

The strength of the Compton scattering experiments is that a part of the reaction relies on the electromagnetic interaction which is described by the extremely precise theory of Quantum ElectroDynamics (QED) [3]. Thus, thanks to its excellent precision, the electromagnetic probe will provide observables which are well understood and have an unambiguous physical interpretation.

The proton Generalized Polarizabilities (GPs) are one of those observables accessible via Compton scattering, more precisely via Virtual Compton Scattering (VCS) when a virtual photon scatters on a proton and a real photon is emitted. The GPs depend on the virtuality Q^2 of the initial photon. In this context the GPs are dynamical properties which describe the collective behavior of the proton components when it is submitted to an applied electromagnetic field. The emitted photon, of small energy, can then be seen as the quasi-static electromagnetic field while the virtual photon will be the probe of the deformed proton.

The GPs were first introduced for nuclei by Arenhövel and Drechsel [4] as a concept analogous to the classical description of the light scattering on atoms and molecules. Later, in 1995, P.A.M Guichon et al. studied the case of the nucleon, and derived a Low Energy Theorem for VCS on the proton [5], in a formalism that involves six independent GPs [6] at lowest-order. This triggered a series of

dedicated VCS experiments throughout the world.

Among the six proton GPs the electric and magnetic GPs are the main topic of this work. They are scalar quantities which provide information on the proton local distribution of induced electric and magnetic dipoles and will help to understand its internal structure. For instance polarizabilities play a role in the proton charge radius puzzle, through the two-photon exchange process. More specifically, the GPs are probes which help us to understand the contributions from the proton mesonic cloud and its quark core.

The VCS process $\gamma^* p \to \gamma p$ is accessible via the reaction of exclusive photon electroproduction $ep \to ep\gamma$. Studies of such a low cross-section process became possible with high duty-factor electron accelerators, and high-resolution spectrometers. The electric and magnetic GPs were measured for the first time at MAMI [7], later, Bates and JLab experiments were able to provide new values at different observation scales. However the current world data have shown an unexpected behavior with respect to the observation scale in the region around $Q^2 = 0.33\ GeV^2$.

The present work is a part of the experiment done at MAMI from 2011 to 2015, with the aim to understand better the Q^2-behavior of the electric and magnetic GPs of the proton [8]. Measurements were performed at three new values of Q^2: 0.1, 0.2 and 0.45 GeV^2 and the present work covers the analysis of the data at $Q^2 = 0.2\ GeV^2$.

The thesis content is as follows. First the theoretical context and physics motivations are introduced. Then the MAMI accelerator, the high-resolution spectrometers and the data-taking conditions are explained. Finally the data analysis is presented in detail and divided in two parts. The first-level analysis concerns the treatment of experimental data: calibrations and event selection. The second-level analysis consists in determining the five-fold differential cross section $d^5\sigma(ep \to ep\gamma)$ and in extracting the VCS observables: the structure functions $P_{LL} - P_{TT}/\epsilon$ and P_{LT}, and the electric and magnetic GPs $\alpha_E(Q^2)$ and $\beta_M(Q^2)$ at $Q^2 = 0.2\ GeV^2$.

Chapter 1

Introduction to Real and Virtual Compton Scattering

In this chapter the GPs will be presented from their phenomenological description to the theoretical tool which made possible their extraction from experiments.

In section 1.1 more basic nucleon observables are first introduced, i.e. the electromagnetic form factors. This is because they directly intervene in the GP extraction and their phenomenological description simplify the physical understanding of GPs.

Then in section 1.2 the Real Compton scattering polarizabilities are described in order to introduce the GP formalism.

Finally, in the last section 1.3 the GPs are detailed together with the Virtual Compton Scattering process which allows to access them.

1.1 Proton form factors

The electric form factor $G_E^p(\mathbf{q}^2)$ and the magnetic form factor $G_M^p(\mathbf{q}^2)$ are the most basic quantities which describe the proton's internal structure. They naturally intervene in quantum electrodynamics (QED) processes when a charged particle interacts with the proton. The virtual photon is the vector boson of such electromagnetic interactions and carries a four-momentum squared $\mathbf{q}^2$ ($\mathbf{q}^2 = q^{0^2} - \vec{q}^2$ being negative for a space-like photon). The form factors will then depend on $\mathbf{q}^2$ which defines the scale of the interaction.

The form factors express the spatial properties of the proton. More precisely, they contain the information about how the charges and the currents are distributed in the proton volume. This spatial information is encoded in the $\mathbf{q}^2$ dependency. To understand how, it is common to express the momentum carried by the virtual photon in terms of its wavelength. According to de Broglie, the relation between the wavelength and the momentum is :

$$\lambda = \frac{h}{|\vec{q}|}, \tag{1.1}$$

with h the Planck's constant. The de Broglie equation defines the link between the momentum exchanged and the interaction scale. The larger the momentum is the smaller the wavelength becomes, and so, the more localized the interaction

9

is. If the virtual photon's wavelength is large compared to the proton size, the interacting charged particle will be only sensitive to its global properties, the total proton charge and magnetic moment. If the photon's wavelength is small enough, the internal structure of the proton can be probed. The same reasoning can be applied to the four-momentum $\mathbf{q}^2$, yielding: $\lambda = h/\sqrt{-\mathbf{q}^2}$.

Then the $\mathbf{q}^2$-dependency of form factors can be translated in terms of spatial distribution via a Fourier transform[1]. The Fourier transform of the electric or magnetic form factors will lead to the radial distribution of, respectively, the charge or the current :

$$G_E^p(\mathbf{q}^2) \xrightarrow{FT} \rho_{electric}(\vec{r}),$$
$$G_M^p(\mathbf{q}^2) \xrightarrow{FT} \rho_{magnetization}(\vec{r}). \tag{1.2}$$

In equation 1.2, $\rho_{electric}(\vec{r})$ is the charge density along $\vec{r}$. However this non-relativistic representation of the proton charge density is criticized [9].

Indeed at relativistic energy, like in most hadron physics experiments nowadays, the scattered proton moves at high velocity. As the proton size and shape are not relativistically invariant quantities, its structure looks different in different frames. Also the relativistic process of pair creation further compromises a non-relativistic density interpretation. In his paper, Miller [9] presents another density representation which is valid in a particular dynamics, the light-front dynamics. Its use in association with a particular frame, called the Drell-Yan frame, will allow a relativistic interpretation of the proton charge density: $\rho(b)$ with b the transverse distance in the frame. Unlike the density from equation 1.2, this new density is two-dimensional and so is the Fourier transform defined in this formalism.

This interpretation has also the advantage to use directly the more fundamental form factors $F_1(\mathbf{q}^2)$ and $F_2(\mathbf{q}^2)$ called the Dirac and Pauli form factors. Indeed $G_E^p(\mathbf{q}^2)$ and $G_M^p(\mathbf{q}^2)$ are not as fundamental, they are linear combinations of $F_1(\mathbf{q}^2)$ and $F_2(\mathbf{q}^2)$ built to avoid the interferences due to the $F_1 \times F_2$ product in the $(ep \rightarrow ep)$ elastic cross-section. The physical meaning and the preferential use of $G_E^p(\mathbf{q}^2)$ and $G_M^p(\mathbf{q}^2)$ is then emphasized by the non-relativistic interpretation of equation 1.2. The linear combinations are, for a space-like virtual photon:

$$G_E^p(\mathbf{q}^2) = F_1(\mathbf{q}^2) + \frac{q^2}{4m_p^2}F_2(\mathbf{q}^2), \tag{1.3a}$$

$$G_M^p(\mathbf{q}^2) = F_1(\mathbf{q}^2) + F_2(\mathbf{q}^2), \tag{1.3b}$$

where m_p is the proton mass. So the density interpretation of form factors is still discussed nowadays. More generally the proton structure can be represented by two different pictures: a non-relativistic one, described by effective field theory, and a relativistic one which uses the quantum theory of quarks and gluons (QCD). Anyway, none of these descriptions are fully correct [10]. As will be explained in section 1.3 the two interpretations also impact our representation of generalized polarizabilities.

---

[1]this property of the Fourier transform is shown in a particular frame: the Breit frame. It is the frame in which the proton momentum is reversed in the scattering process.

1.1.1 Elastic electron-proton scattering

Elastic electron-proton scattering is the main process to measure the proton form factors, for two reasons. First the electron is a pointlike particle, so the structure effects in the cross section will only be due to the proton. The second reason is the simplicity of the process, i.e. both the electron and the proton stay in their ground state and no other particles are created. So in the one-photon exchange approximation we can perfectly describe the interaction using QED.

In this framework, elastic electron scattering is illustrated in figure 1.1. The process contains an incident electron with a four-momentum $\mathbf{k} = (E, \vec{k})$ which exchanges a virtual photon γ^* with the proton target. The outgoing electron has a four-momentum $\mathbf{k'} = (E', \vec{k'})$. The protons are defined by the four-momenta $\mathbf{p}$ and $\mathbf{p'}$. The four-momentum transferred by the virtual photon is $\mathbf{q} = \mathbf{k} - \mathbf{k'} = \mathbf{p'} - \mathbf{p}$.
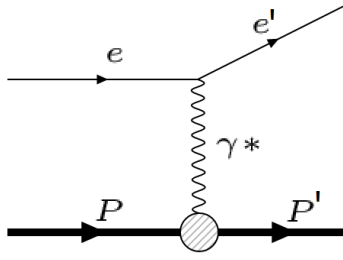
Figure 1.1: Diagram of elastic electron scattering off the proton. The blob indicates that the proton's internal structure is probed.

It is common practice to define the quantity Q^2, as the opposite of $\mathbf{q}^2$ (when Q^2 is smaller the scale of the interaction is also larger). We recall where the form factors $G_E^p(Q^2)$ and $G_M^p(Q^2)$ intervene in the elastic cross section.

The general case of elastic electron scattering off a target is characterized by the following cross section:

$$\left(\frac{d\sigma}{d\Omega}\right)_{lab} = \left(\frac{d\sigma}{d\Omega}\right)_{Mott} \frac{E'}{E} |F(Q^2)|^2, \tag{1.4}$$

where $\left(\frac{d\sigma}{d\Omega}\right)_{Mott}$ is the Mott cross section [11] corresponding to the particular case of a spinless-particle target in the relativistic case. It takes the following form:

$$\left(\frac{d\sigma}{d\Omega}\right)_{Mott} = \frac{Z^2 \alpha_{QED}^2 cos^2 \frac{\theta_e}{2}}{4E^2 sin^4 \frac{\theta_e}{2}}, \tag{1.5}$$

with Z the charge of the target in units of the elementary charge, α_{QED} the fine structure constant [2], and θ_e the scattering angle of the electron in the laboratory frame.

In the general case of equation 1.4 the term $\frac{E'}{E}$ is the target recoil correction term: $\frac{E'}{E} = \frac{1}{1 + 2\frac{E}{M_{target}} sin^2 \frac{\theta_e}{2}}$ which tends to 1 when $M_{target} >> E$.

---

[2] $\alpha_{QED} = e^2/4\pi\epsilon_0 \hbar c$, with ϵ_0 the vacuum permittivity and $\hbar = h/2\pi$.

The last term of equation 1.4, $|F(Q^2)|^2$, depends on the target internal structure. $F(Q^2)$ is the target form factor that we can express specifically for the proton. According to [12], in the case of an elastic electron scattering off the proton, equation 1.4 becomes the Rosenbluth formula:

$$\left(\frac{d\sigma}{d\Omega}\right) = \left(\frac{d\sigma}{d\Omega}\right)_{Mott} \frac{E'}{E} \left[\frac{G_E^p(Q^2)^2 + \tau G_M^p(Q^2)^2}{1+\tau} + 2\tau G_M^p(Q^2)^2 tan^2(\frac{\theta_e}{2}) \right], \qquad (1.6)$$

with $\tau = Q^2/4m_p^2$.

In the limit $Q^2 = 0$, the form factors are normalized to the proton total charge in units of the electron charge, and to the proton total magnetic moment in units of the nuclear magneton μ_N:

$$G_E^p(0) = 1 ,$$
$$G_M^p(0) = 2.793.$$

1.1.2 Form factor measurements and particular values at $Q^2 = 0.2~GeV^2$

Experimental procedure

Elastic electron scattering off the proton was measured since the fifties [13] and continues nowadays, at Mainz [14] and other laboratories in the world (see [15] for a review).

There are two kinds of experiments that can access form factors. The first ones measure directly the electron scattering cross section and use equation 1.6 to extract form factors separately. The second ones require a polarized electron beam and the knowledge of outgoing-proton polarization to measure the asymmetry and then deduce the ratio G_E/G_M.

For the experiments dedicated to cross section measurement the classical way to extract form factors from cross section is called the Rosenbluth separation (equation 1.6). This method uses cross sections comparison at the same Q^2 but different angles θ_e to obtain linear combinations of $G_E^p(Q^2)$ and $G_M^p(Q^2)$ which allow their extraction. The Rosenbluth separation has the advantage to provide model-independent results. But one can also do a direct fit of form factors based on a model shape as it has been done at MAMI [14] recently.

The polarization experiments consist in measuring the longitudinal and transverse polarization components of the recoil proton. The two components are obtained simultaneously by the single measurement of the azimuthal angular distribution of the scattered proton in a focal-plane polarimeter. The ratio G_E/G_M is then directly deduced with reduced systematic uncertainties. This constitutes the major advantage of this method, compared to cross-section measurement.

There is an inconsistency between the results from unpolarized cross-section and polarization experiments. It is believed to be a consequence of the one-photon-exchange approximation. Because of the diverging results in the two-photon exchange correction, it is so far an unresolved puzzle [14].

There is actually a third method to measure the proton form factors which has been explored at MAMI recently. It is based on (e, e') cross-section measurements in the radiative tail and aimed at determining the form factors at very low Q^2 [16].

Values at $Q^2 = 0.2 \ GeV^2$

Many experiments led to different $G_E^p(Q^2)$ and $G_M^p(Q^2)$ results over time, thus there are many different parametrizations of the form factors versus Q^2. However in order to extract the proton GPs at $Q^2 = 0.2 \ GeV^2$ we need to fix a form-factor parametrization. In section 5.4.3 we will see how the choice of proton form factors impacts our VCS analysis.

At small Q^2, the form-factor behavior follows more or less the standard dipole parametrization defined as :

$$G_D = (1 + \frac{Q^2}{0.71})^{-2}, \tag{1.7}$$

with Q^2 expressed in GeV^2. Most parametrizations exhibit a few percent deviation from the standard dipole. The agreement between various "reliable" parametrizations is not better than 1-2%.

So, for our GP extraction, it was decided to use three different parametrizations of form factors at $Q^2 = 0.2 \ GeV^2$. The Friedrich-Walcher parametrization [17] gives "central" values of form factors. The Arrington et al. [18] and Bernauer et al. [19] parametrizations were chosen for their very different values of $G_E^p(Q^2)$ and $G_M^p(Q^2)$ at $Q^2 = 0.2 \ GeV^2$. The Q^2-behavior of those three parametrizations is presented in figure 1.2.
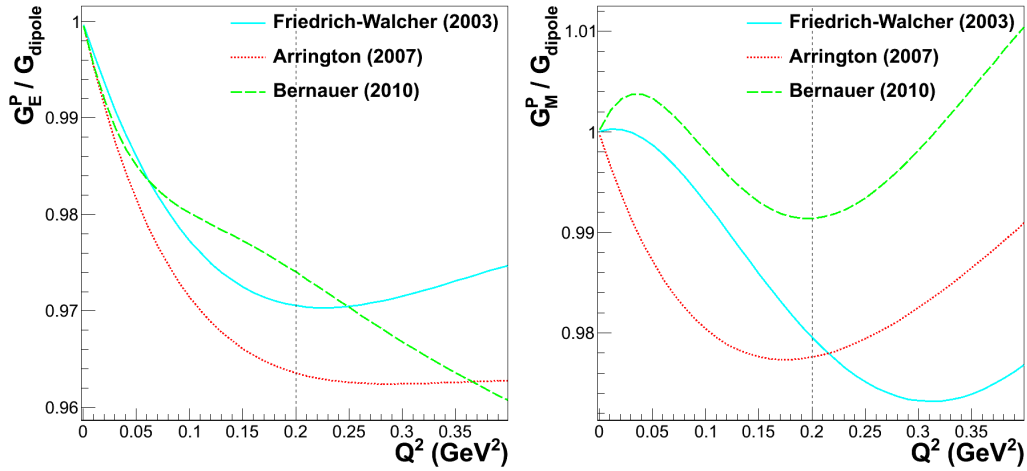
Figure 1.2: Behavior of electric (left) and magnetic (right) proton form factors, divided by the dipole, as a function of Q^2. The parametrizations are from Bernauer et al. [19] (dashed green line), Arrington et al. [18] (red dotted line) and Friedrich-Walcher [17] (blue full line). The vertical line shows the value at $Q^2 = 0.2 \ GeV^2$.

At $Q^2 = 0.2 \ GeV^2$ the use of Arrington et al. or Bernauer et al. parametrizations induces a 1% variation in G_E and a 1.4% variation in G_M.

13

1.2 Polarizabilities of the proton: Real Compton scattering

Like the form factors, the polarizabilities are fundamental structure constants of the proton; they are a consequence of its composite nature and characterize the proton stiffness in an external electromagnetic field.

The polarizabilities are defined in the real Compton scattering (RCS) context, illustrated in figure 1.3, when an incident real photon with a four-momentum $\mathbf{q} = (q^0, \vec{q})$ interacts with the proton by the reaction $\gamma p \to \gamma p$. There is an infinite number of polarizabilities and so far only the six first ones[3] were extracted. The electric and magnetic polarizabilities α_E and β_M describe the response of, respectively, the proton charge and magnetic moment distributions to the static external field. The four other polarizabilities: $\gamma_{E1}, \gamma_{M1}, \gamma_{E2}$ and γ_{M2} are quantities of higher dimension that describe the proton behavior when a flip of its spin is involved. Recently, the spin polarizabilities were measured for the first time separately at MAMI [20]. The physical meaning of some other polarizabilities is detailed in [21].

To better understand the role of the electric and magnetic polarizabilities α_E and β_M it is convenient to use the pion cloud model. In this model, neither proved to be valid or not [10], the proton is represented by three valence quarks surrounded by a pion cloud. The pions are spinless and considered as neutral or charged (positively or negatively). The valence quarks are, of course, charged and do have an intrinsic magnetic moment due to their spin.

One considers that initially the positive and negative charges are distributed in such a way that they share the same center of distribution. When an electric field $\vec{E}$ is applied to the proton the positive and negative charges are pushed in opposite directions. This generates an induced electric dipole moment $\vec{d}$ which is proportional to $\vec{E}$:

$$\vec{d} = \alpha_E \vec{E}, \tag{1.8}$$

and the factor of proportionality α_E is the electric polarizability. α_E is expressed in units of a volume (fm^3). Its value is fixed by the proton stiffness, the stronger the proton's constituents are bound the smaller α_E is.

Now if one applies a magnetic field $\vec{H}$ to the proton the valence-quarks magnetic moment tends to become aligned with $\vec{H}$ and creates a paramagnetic moment $\vec{\mu}$, whereas $\vec{H}$ will induce currents in the pion cloud which will oppose a diamagnetic moment to $\vec{H}$ and reduce $\vec{\mu}$. One can express the induced magnetic dipole as:

$$\vec{\mu} = \beta_M \vec{H} = (\beta_M^{dia} + \beta_M^{para})\vec{H}, \tag{1.9}$$

and due to these opposite effects the magnetic polarizability β_M will be smaller than α_E.

---

[3]First to appear in the q' development, detailed in section 1.2.1.

1.2.1 RCS amplitude and cross-section

The RCS process is the tool to access polarizabilities. Its kinematics is defined by the incoming real photon four-momentum $\mathbf{q} = (q^0, \vec{q})$, the one of the outgoing real photon $\mathbf{q'}$ and by the initial and final protons four-momenta $\mathbf{p}$ and $\mathbf{p'}$.
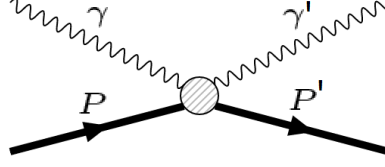
Figure 1.3: Diagram of Real Compton Scattering.

The blob represented in figure 1.3 illustrates the production of "proton excited states". Although there is not enough energy to produce such states at low energies (typically below the pion threshold) they intervene in the process as virtual intermediate states. So the magnitude of the proton deformation, expressed by the polarizabilities, depends on the proton excited states and the expression of a "deformed" proton adopted in this thesis refers to the virtual states effect. This is expressed by the general relation (in a non-relativistic approach at the first-order perturbation), e.g. for the electric polarizability:

$$\alpha_E = 2 \sum_{N^* \neq N} \frac{|<N^*|d_z|N>|^2}{E_{N^*} - E_N},\tag{1.10}$$

where N^* indicates a nucleon resonance and d_z the electric dipole-moment operator [22].

At very low incident photon energy $q^0 \to 0$ the RCS amplitude is perfectly described by the Thomson amplitude [23]. It depends only on proton's static properties such as the mass, the charge and the anomalous magnetic moment κ. When the photon energy increases, but is still below the pion production threshold ($q^0_\pi = 144.7\ MeV/c$ in the lab frame where the proton is at rest), the amplitude can be expressed as an expansion of terms ordered in powers of q^0 and q'^0. This expansion is based on the Low Energy Theorem which first appears in the article of F. E. Low [24]. The complete amplitude was then developed by Petrun'kin [25] up to the order $q'^0 q^0$, in the lab frame. The amplitude is therefore:

$$
\begin{aligned}
f_{Pet} = \ & -\frac{e^2}{m_p}\vec{\epsilon'} \cdot \vec{\epsilon} \\
& +i(q'^0 + q^0)\frac{e^2}{4m_p^2}(1 + 2\kappa)\vec{\sigma} \cdot (\vec{\epsilon'} \times \vec{\epsilon}) \\
& -i(q'^0 + q^0)\frac{e^2}{4m_p^2}(1 + \kappa)^2\vec{\sigma} \cdot [(\vec{n'} \times \vec{\epsilon'}) \times (\vec{n} \times \vec{\epsilon})] \\
& +i\frac{e^2}{2m_p^2}(1 + \kappa)[q'^0(\vec{n'} \cdot \vec{\epsilon})\vec{\sigma} \cdot (\vec{n'} \times \vec{\epsilon'}) - q^0(\vec{n} \cdot \vec{\epsilon'})\vec{\sigma} \cdot (\vec{n} \times \vec{\epsilon})] \\
& +q'^0 q^0 \frac{e^2}{4m_p^3}(2\kappa + \kappa^2)\vec{\epsilon'} \cdot \vec{\epsilon} \\
& -q'^0 q^0 \frac{e^2}{4m_p^3}(1 + \kappa)^2(\vec{n'} \times \vec{\epsilon'}) \cdot (\vec{n} \times \vec{\epsilon})(\vec{n'} \cdot \vec{n}) \\
& +q'^0 q^0 \frac{e^2}{4m_p^3}(\vec{n'} \times \vec{\epsilon'}) \cdot (\vec{n} \times \vec{\epsilon}) \\
& +q'^0 q^0 [\bar{\alpha}_E \vec{\epsilon'} \cdot \vec{\epsilon} + \bar{\beta}_M(\vec{n'} \times \vec{\epsilon'}) \cdot (\vec{n} \times \vec{\epsilon})]
\end{aligned}
\tag{1.11}
$$

with $\vec{\epsilon}$ and $\vec{\epsilon'}$ the polarization vectors of the incoming and scattered photons, $\vec{n}$ and $\vec{n'}$ their unit momentum vector and σ the Pauli spin matrices. In the Petrun'kin amplitude of equation 1.11 the first term is the Thomson scattering amplitude, the six following lines are due to the proton magnetic moment. The polarizabilities arise in the last line through $\bar{\alpha}_E$ and $\bar{\beta}_M$. $\bar{\alpha}_E$ and $\bar{\beta}_M$ are the polarizabilities that are experimentally accessible, also called "dynamical". They differ from the "static" polarizabilitites α_E and β_M of the previous subsection by a corrective term called the retardation correction[4]. For instance one can write:

$$\bar{\alpha}_E = \alpha_E + \frac{e^2}{3m_p} < r^2 >, \qquad (1.12)$$

with $< r^2 >$ the mean squared radius of the charge distribution.

The Petrun'kin expansion is valid for $q^0 \lesssim 80$ MeV; at higher energy other terms arise, especially the next-order terms are described by the spin polarizabilities γ_{E1}, γ_{M1}, γ_{E2} and γ_{M2}. Keeping every higher-order term in the squaring of the Petrun'kin amplitude will lead to the Real Compton Scattering cross section [23]:

$$\left(\frac{d\sigma}{d\Omega}\right)_{Lab} = \left(\frac{d\sigma}{d\Omega}\right)_{Powell} - q^0 q'^0 (\frac{q'^0}{q^0})^2 \frac{e^2}{m_p} \left[\frac{\bar{\alpha}_E + \bar{\beta}_M}{2}(1+z)^2 + \frac{\bar{\alpha}_E - \bar{\beta}_M}{2}(1-z)^2\right] + o(q^3) \quad (1.13)$$

where $z = cos(\theta_\gamma)$. The term $o(q^3)$ contains other polarizabilities (among which the spin polarizabilities), it is neglected in the low-energy regime. The Powell cross section that appears in equation 1.13 expresses the scattering of the photon on a pointlike proton :

$$\left(\frac{d\sigma}{d\Omega}\right)_{Powell} = \frac{1}{2}(\frac{q'^0}{q^0})^2 \left(\frac{e^2}{m_p}\right)^2 \left[1 + z^2 + \frac{q^0 q'^0}{m_p^2}((1-z)^2 + a_0 + a_1 z + a_2 z^2)\right], \quad (1.14)$$

with the coefficients :

$$a_0 = 2\kappa + \frac{9}{2}\kappa^2 + 3\kappa^3 + \frac{3}{4}\kappa^4, \qquad (1.15a)$$

$$a_1 = -4\kappa - 5\kappa^2 - 2\kappa^3, \qquad (1.15b)$$

$$a_2 = 2\kappa + \frac{1}{2}\kappa^2 - \kappa^3 - \frac{1}{4}\kappa^4. \qquad (1.15c)$$

Measuring the RCS cross section at different kinematics (different angles θ_γ and different q^0) will then allow to extract the polarizabilities thanks to equation 1.13.

1.2.2 Proton polarizabilities measurement

The proton polarizabilities in RCS are extracted since 1960, with the first pioneering experiment [26], and nowadays they are still under investigation. In order to improve measurements an additional constraint may be added to the global extraction procedure. It requires the measurement of the total photo-absorption

---

[4]The retardation correction is related to the propagation of the electromagnetic wave, of non-zero frequency, through the finite size of the nucleon [22].

cross section $\sigma_\gamma(q^0)$. Indeed the uncertainty on polarizabilities may be reduced by using the Baldin sum rule [27] for the proton:

$$\bar{\alpha}_E + \bar{\beta}_M = \frac{1}{2\pi} \int_{q_\pi^0}^\infty \frac{\sigma_\gamma(q^0)}{q^{0^2}} dq^0 = (13.8 \pm 0.4) \cdot 10^{-4} fm^3, \qquad (1.16)$$

where the sum rule value is taken from [23].

The 2014 Particle Data Group [28] gives the following value for the electric and magnetic polarizabilities of the proton:

$$\bar{\alpha}_E = (11.5 \pm 0.4) \cdot 10^{-4} \ fm^3 \ ,$$
$$\bar{\beta}_M = (2.5 \pm 0.4) \cdot 10^{-4} \ fm^3.$$

These results demonstrate the extreme proton stiffness. To better understand this, it is convenient to compare the proton polarizability to its volume. α_E is of the order of 10^{-4} times its volume, therefore the proton's internal structure is barely deformed by quasi-static electric fields. For an atom the electric polarizability is of the order of its volume, therefore the proton components are considerably more linked by the strong interaction than the atom components are by the electromagnetic interaction.

1.3 Generalized polarizabilities of the proton

Just like for the form factors, the polarizabilities can be described as a function of a four-momentum transfer $\mathbf{q}^2$. Taking into account this dependency will lead to Generalized Polarizabilities (GPs). They are fundamental quantities which describe the proton deformation in an applied electromagnetic field, but unlike the RCS polarizabilities, which express the global deformation, the generalized polarizabilities contain the information about the local deformation. The mechanism of how this local information is encoded in the $\mathbf{q}^2$-dependency is similar to the one described in section 1.1 for form factors.

The generalization of the electric polarizability will then be $\alpha_E(\mathbf{q}^2)$ and will contain information about the local electric deformation (for simplification the generalized polarizabilities are written without their bar). Thereafter, in the same way it was shown for form factors, applying a Fourier transform to $\alpha_E(\mathbf{q}^2)$ will allow us to draw a representation of this electric deformation along $\vec{r}$.

Figure 1.4 from [29][30] is one of these representations. It is a theoretical picture obtained in the framework of the heavy-baryon chiral perturbation theory (HBχPT $O(p^3)$). The figure shows the local induced electric dipole moments as an electric field is applied along the x axis; as we can see the local deformation also possesses a component transverse to the electric field.

Similar considerations with an applied magnetic field will lead to pictures of the local magnetic polarization, which is described through the $\mathbf{q}^2$-dependency of the magnetic polarizability, the so-called generalized magnetic polarizability $\beta_M(\mathbf{q}^2)$. The other RCS polarizabilities, such as spin polarizabilities, can also be extended to their $\mathbf{q}^2$-dependency.

As mentioned in section 1.1 there are two possible representations of the proton: one in the standard dynamics and the other in the light-front dynamics. Figure 1.4
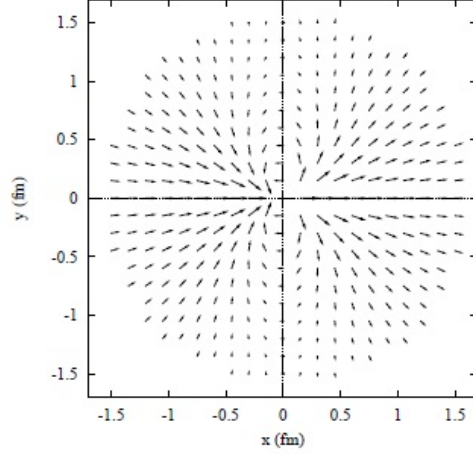
Figure 1.4: Nucleon polarization induced by an electric field along the x axis, calculated in the framework of HBχPT $O(p^3)$. Figure taken from [29].

is obtained with the standard dynamics. A recent interpretation of the GPs, which was performed in the light-front dynamics by Gorchtein et al. [31], is presented in figure 1.5. The figure shows the induced polarization in a proton submitted to an electric field along the x-axis, which is globally a dipole pattern. In ref [31] it is shown how different parametrizations of the electric GP modify the local polarization distribution.
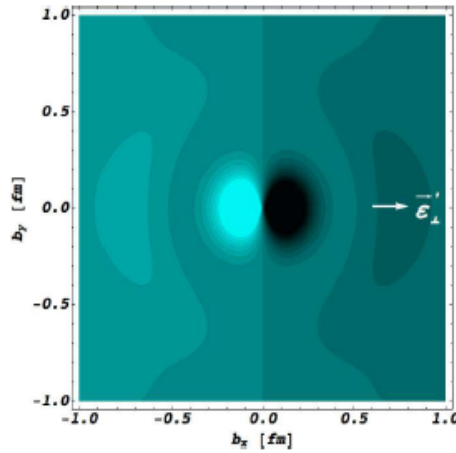
Figure 1.5: Induced polarization in a proton of definite light-cone helicity when submitted to an electromagnetic field. The light (dark) regions correspond to the largest (smallest) values. Figure taken from [31].

These two representations of the proton allow us to visualize the deformation of the charge density in an external field and map out the transverse position space dependence of the induced polarization. But, once again, figures 1.4 and 1.5 cannot be compared since they are obtained in completely different formalisms.

1.3.1 Virtual Compton scattering off a proton

The tool we used to extract GPs is the Virtual Compton scattering process (VCS) $\gamma^* + p \rightarrow p' + \gamma$, represented in figure 1.6 (b) and (c). Indeed, just like for form factors, it is the virtuality of the photon that allows to explore the local information inside the nucleon. So the experimentally studied process is $e + p \rightarrow e' + p' + \gamma$, the so-called photon electroproduction which is fully detailed in figure 1.6.

This reaction is the combination of three sub-processes experimentally indiscernible:

- The Bethe-Heitler (BH) process corresponding to electron bremsstrahlung and represented in figure 1.6-a.

- The Born part of VCS that is bremsstrahlung from a "non-deformed" proton, figure 1.6-b.

- The non-Born part of VCS where virtual excited states intervene, figure 1.6-c. In this process the real-photon emission is done by the "deformed" proton and depends on the GPs.
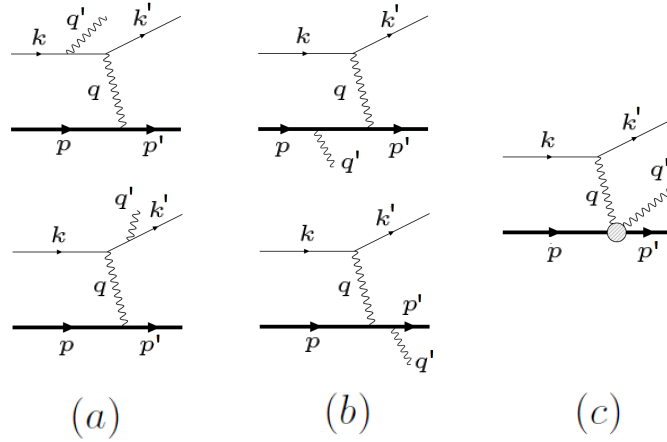
Figure 1.6: Diagrams of the photon electroproduction process: (a) bremsstrahlung from the electrons side, (b) Born part of VCS, (c) non-Born part of VCS.

A theoretical convention defines a last process as a part of non-Born VCS, it is the π^0 exchange in the t-channel represented in figure 1.7 (see also figure 2.5). Therefore this particular process also contributes to the GPs and more exactly to the spin-flip GPs [32].
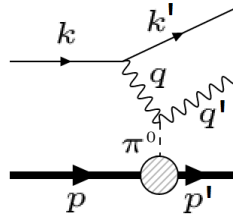
Figure 1.7: π^0 exchange in the t-channel.

VCS Kinematics

In this section we will describe the VCS kinematics and define its main variables. In a VCS event the incident electron with a four-momentum $\mathbf{k} = (E, \vec{k})$ exchanges a virtual photon γ^* with the proton target. The outgoing electron has a four-momentum $\mathbf{k'} = (E', \vec{k'})$. The protons are again defined by the four-momenta $\mathbf{p}$ and $\mathbf{p'}$. The four-momentum transferred by the virtual photon is again $\mathbf{q} = (q^0, \vec{q})$ with $q^0 = E - E'$ and $\vec{q} = \vec{k} - \vec{k'}$. All those notations are summarized in table 1.3.1. One has to note that for the VCS process the photon virtuality is equal to: $\mathbf{q}^2 = (\mathbf{k} - \mathbf{k'})^2$ whereas for the BH process the photon virtuality is equal to: $(\mathbf{p'} - \mathbf{p})^2$.

Particle	e	e'	γ^*	p	p'	γ
Four-momentum	$\mathbf{k}$	$\mathbf{k'}$	$\mathbf{q} = \mathbf{k\text{-}k'}$	$\mathbf{p}$	$\mathbf{p'}$	$\mathbf{q'}$
Mass squared	m_e^2	m_e^2	$q^2 = -Q^2 < 0$	m_p^2	m_p^2	0
Momentum vector	$\vec{k}$	$\vec{k'}$	$\vec{q} = \vec{k} - \vec{k'}$	$\vec{p}$	$\vec{p'}$	$\vec{q'}$
Modulus of momentum vector	k	k'	q	p	p'	q'
Helicity and Spin projection	h	h'	λ	σ	σ'	λ'

Table 1.3.1 : Main variables of the VCS kinematics.

In this thesis the kinematics will be described in two frames, the virtual-photon/target-proton center-of-mass (CM) and the laboratory where the initial proton is at rest. Variables of the CM will be written with the *cm* index. Lab variables will be written with no index.

For VCS two planes, presented in figure 1.8 can be distinguished:
- the scattering plane defined by both electron vectors $\vec{k}$ and $\vec{k'}$.
- the reaction plane defined by the recoiling-proton vector $\vec{p'}$ and the real photon vector $\vec{q'}$.

Both planes contain the virtual-photon vector $\vec{q}$, and so the two planes rotate around the $\vec{q}$-axis defining the angle φ, being the same in the two frames: $\varphi_{cm} = \varphi$. The angle between the real-photon vector $\vec{q'}_{cm}$ and the virtual-photon vector $\vec{q}_{cm}$ is θ_{cm}. The angle between the electron vectors is $\theta_{e,cm}$ (θ_e in the lab frame) .

Because of the Lorentz boost from the CM to the lab system, the recoiling-protons are contained in a narrow cone around the direction of the virtual photon. For instance, at $Q^2 = 0.2 \ GeV^2$ the cone angle varies from $\theta_{cone} = \pm 5°$ to $\theta_{cone} = \pm 14°$. So having a detector with a relatively small acceptance will be enough to cover a large range in θ_{cm}.

To completely determine the kinematics of the photon-electroproduction reaction five independent variables are necessary. Two sets of variables may be used: $(k, k', \theta_e, \theta_{cm}, \varphi_{cm})$ and $(q_{cm}, q'_{cm}, \epsilon, \theta_{cm}, \varphi_{cm})$, where ϵ is the linear polarization parameter of the virtual photon.

The following relations (1.17 and 1.18) are used to switch from a set to the other :
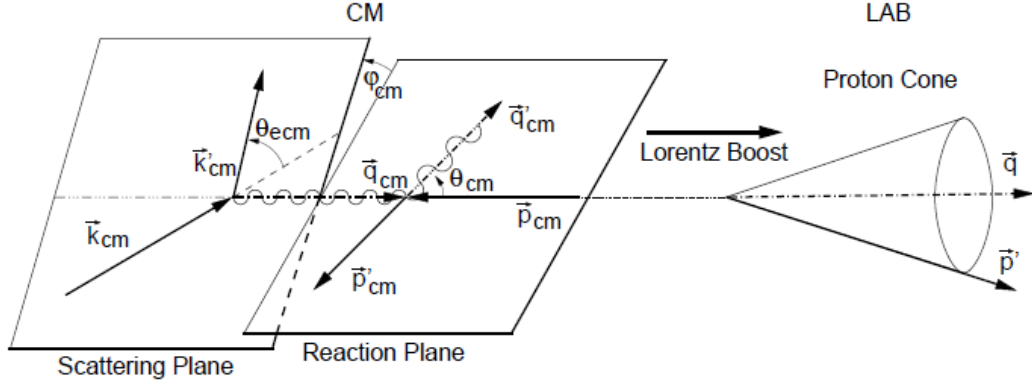
Figure 1.8: VCS represented in the CM and laboratory frames. (Left) VCS variables as they are defined in the CM. (Right) representation of the final proton boosted in a cone around the virtual photon vector $\vec{q}$ as defined in the lab frame.

$$Q^2 = 4kk'\sin^2\left(\frac{\theta_e}{2}\right), \tag{1.17a}$$

$$s = -Q^2 + m_p^2 + 2m_p q^0, \tag{1.17b}$$

$$\epsilon = [1 + 2\frac{q^2}{Q^2}\tan^2\left(\frac{\theta_e}{2}\right)]^{-1}, \tag{1.17c}$$

with $\sqrt{s}$ the total energy in the center-of-mass.

$$\begin{aligned}
q_{cm}^0 &= \frac{s - Q^2 - m_p^2}{2\sqrt{s}}, & q_{cm} &= \sqrt{Q^2 + q_{cm}^0{}^2}, \\
q_{cm}'^0 &= \frac{s - m_p^2}{2\sqrt{s}}, & q_{cm}' &= q_{cm}'^0, \\
p_{cm}^0 &= \frac{s + Q^2 + m_p^2}{2\sqrt{s}}, & p_{cm} &= q_{cm}, \\
p_{cm}'^0 &= \frac{s + m_p^2}{2\sqrt{s}}, & p_{cm}' &= q_{cm}'.
\end{aligned} \tag{1.18}$$

For our experiment we choose to use the $(q_{cm}, q_{cm}', \epsilon, \theta_{cm}, \varphi_{cm})$ set. One also has to consider the $\tilde{Q}^2$ variable, introduced in [5], which is Q^2 at the limit of $q_{cm}' \to 0$ at a fixed q_{cm}:

$$\begin{aligned}
\tilde{Q}^2 &= Q^2|_{q_{cm}' \to 0} = -2m_p \tilde{q}_{cm}^0, \\
\tilde{q}_{cm}^0 &= q_{cm}^0|_{q_{cm}' \to 0} = m_p - \sqrt{m_p^2 + q_{cm}^2}.
\end{aligned} \tag{1.19}$$

As a consequence, GPs can be considered as function of q_{cm} or $\tilde{Q}^2$ equivalently.

In our experiment q_{cm} is considered fixed at 458 MeV/c, which corresponds to $\tilde{Q}^2 \approx 0.199 \ GeV^2$ wgile our experimental $< Q^2 >$ is $0.2 \ GeV^2$. The two quantities are close, for now on $\tilde{Q}^2$ will be labeled as Q^2.

21

The three contributions to the photon electroproduction amplitude

Now that the main variables are defined we will detail the three contributions to the photon-electroproduction amplitude and then write the cross section. The photon-electroproduction contributions, represented in figure 1.6, lead to the total amplitude $T^{ee'\gamma}$:

$$T^{ee'\gamma} = T^{BH} + T^B + T^{NB},\tag{1.20}$$

where T^{BH}, T^B and T^{NB} are respectively the amplitude of the Bethe-Heitler, Born and non-Born processes of figure 1.6.

The BH process is divided in two sub-processes: the real photon emission by the electron which is well described by QED and the virtual photon absorption by the proton which depends on form factors. So to fully calculate the Bethe-Heitler amplitude T^{BH} one needs to choose a form-factor parametrization.

The Born process also depends only on the knowledge of form factors and T^B can be calculated via QED.

The non-Born amplitude (NB) is the unknown term of equation 1.20 that we are interested in. The complete NB amplitude is not known analytically but a first-order calculation was performed by Guichon et al. [5]; in section 1.3.3 we will remind how the GPs arise from the amplitude.

The cross section is of course the object experimentally accessible. For the work presented in this thesis we measured the unpolarized photon electroproduction cross-section defined as [33]:

$$\frac{d^5\sigma^{exp}}{dk'd\Omega_{k'}d\Omega_{p'_{cm}}} = \frac{(2\pi)^{-5}}{64m_p}\frac{k'}{k}\frac{s-m_p^2}{s}\mathcal{M}\tag{1.21}$$

with $d\Omega_{k'}$ the final-electron solid angle in the lab, and $\Omega_{p'_{cm}}$ the final-proton solid angle in the center-of-mass frame. $\mathcal{M}$ is the Lorentz invariant defined by :

$$\mathcal{M} = \frac{1}{4}\sum_{\sigma\sigma'h\lambda'}|T^{ee'\gamma}|^2.\tag{1.22}$$

For an unpolarized beam and unknown final-particles polarization the photon-electroproduction amplitude squared has to be summed over all initial and final spin states. For experimentalist's convenience the cross section of equation 1.21 is then written as :

$$d^5\sigma^{exp} = \Phi q'_{cm} \cdot \mathcal{M}\tag{1.23}$$

where $\Phi q'_{cm}$ is the phase-space factor given by :

$$\Phi q'_{cm} = \frac{(2\pi)^{-5}}{64m_p}\frac{k'}{k}\frac{2}{\sqrt{s}} \cdot q'_{cm}.\tag{1.24}$$

The amplitude squared is :

22

$$
\begin{aligned}
|T^{ee'\gamma}|^2 = \quad & |T^{BH}|^2 + |T^B|^2 + |T^{NB}|^2 \\
& + (T^{BH*}T^B + T^{BH}T^{B*}) + (T^{BH*}T^{NB} + T^{BH}T^{NB*}) \\
& + (T^{B*}T^{NB} + T^B T^{NB*}).
\end{aligned}
\tag{1.25}
$$

In the photon electroproduction total cross section the most occurring process depends on the region of the phase space. T^{BH} is the dominant term in the so-called Bethe-Heitler peaks when the outgoing photon is emitted in the direction of one of the electrons. In this particular region it is impossible to extract anything else than the Bethe-Heitler cross section. In other regions of the phase space the Born process will sometimes dominate over BH, but the non-Born process is always small in comparison. Actually only the interference between the non-Born and the sum of the two other processes allows a GP extraction. So equation 1.25 can be written as:

$$
|T^{ee'\gamma}|^2 = \quad |T^{BH+B}|^2 + |T^{NB}|^2 + (T^{BH+B}T^{NB*} + T^{BH+B*}T^{NB})
\tag{1.26}
$$

with $|T^{BH+B}|^2$ that accounts for Born process, Bethe-Heitler process and their interference.

Figure 1.9 illustrates the importance of each contribution for a given kinematics. The BH peaks are located in-plane, near $\theta_{cm} = 70°$ and $\theta_{cm} = 110°$. The GP effect, theoretically calculated and magnified on the figure, will only modify the complete photon electroproduction cross section by a few percent. It is this small effect that we want to measure.

1.3.2 Low Energy Theorem

The Low Energy Theorem (LET or LEX for Low energy EXpansion) offers a model-independent way to express the photon electroproduction cross-section. It is based on perturbation theory and contains only few hypotheses (for instance the one-photon exchange approximation). The LET for VCS, derived by Guichon et al. [5] was inspired by the work of F.E. Low [34]. Thanks to the theorem the three amplitudes of the photon electroproduction process can be expanded in powers of q'_{cm}, in the vicinity of $q'_{cm} = 0$, i.e. for the Bethe-Heitler amplitude :

$$
T^{BH} = \frac{a^{BH}_{-1}}{q'_{cm}} + a^{BH}_0 + q'_{cm} a^{BH}_1 + O^{BH}(q'^2_{cm}),
\tag{1.27}
$$

with the coefficients a^{BH}_i independent of q'_{cm} and $O^{BH}(q'^2_{cm})$ the higher-order terms. The Born amplitude will follow the same kind of expansion and is also known to start at order q'^{-1}_{cm}.

For the non-Born process, an expansion in powers of q'_{cm} was also proved to be possible [5] and can be summarized as :

$$
T^{NB} = q'_{cm} a^{NB}_1 + O^{NB}(q'^2_{cm}),
\tag{1.28}
$$
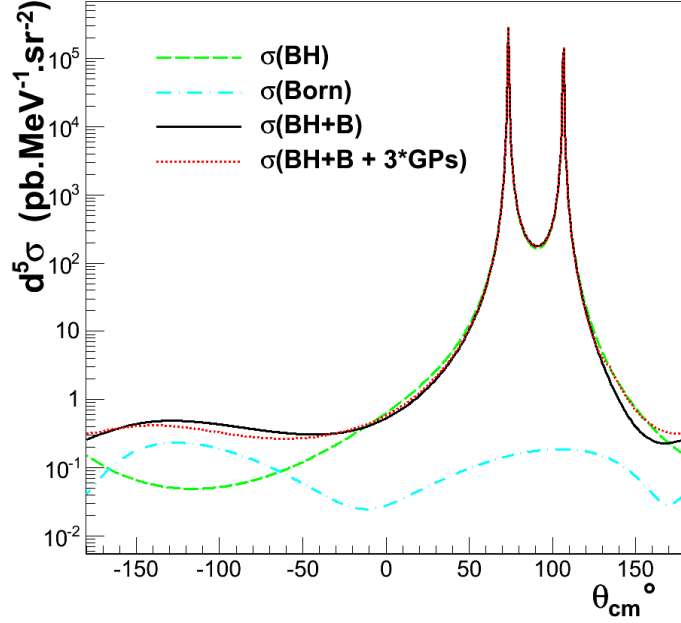
Figure 1.9: In-plane cross section of the photon electroproduction process with respect to θ_{cm}: (green dashed line) BH cross section; (light-blue dashed dotted line) Born cross section; (black full line) cross section of (BH+Born) processes including their interference; (red dotted line) photon electroproduction cross-section considering a theoretical GP effect, multiplied by 3 for visibility. The kinematics are defined by $q_{cm} = 458\ MeV/c$, $q'_{cm} = 100\ MeV/c$, $\epsilon = 0.85$ and $\varphi = 180°$(negative θ_{cm}) or $\varphi = 0°$(positive θ_{cm}), leading to $Q^2 = 0.199\ GeV^2$.

with a_1^{NB} the only coefficient of this expansion that is known analytically. So it appears that in equation 1.25 the only accessible terms are the ones corresponding to $a_{-1}^{BH} \times a_1^{NB}$, $a_{-1}^{B} \times a_1^{NB}$ and $a_1^{NB} \times a_1^{NB}$, this last one being too small to be considered in the first order. As the Born and BH amplitudes are perfectly determined by QED the two amplitudes and their interaction are gathered in a completely known cross-section: σ^{BH+B}.

Then from equation 1.21 one can write a LEX cross-section :

$$\sigma^{LEX} = \sigma^{BH+B} + \Phi q'_{cm}[\mathcal{M}_0 - \mathcal{M}_0^{BH+B}] + O(q'_{cm}{}^2), \tag{1.29}$$

with $[\mathcal{M}_0 - \mathcal{M}_0^{BH+B}]$ the term corresponding to the interference between the BH+B amplitude and the non-Born amplitude at lowest order. $O(q'_{cm}{}^2)$ will then contain every term of higher order.

So the Low Energy Theorem provides a model-independent expression of the photon electroproduction cross section σ^{LEX} which is valid below the pion production threshold: $q'_{cm} \leq 126\ MeV/c$. In the following part we will detail the expression of $[\mathcal{M}_0 - \mathcal{M}_0^{BH+B}]$.

1.3.3 Physical Observables

The way that the GPs arise from T^{NB} is well explained in [5] and [33], in this section we will briefly summarize the results. The non-Born amplitude is:

$$T^{NB}(\lambda',\lambda) = \epsilon'^{*}_{\mu}(\lambda')H_{NB}^{\mu\nu}\epsilon_{\nu}(\lambda), \qquad (1.30)$$

with ϵ_ν the polarization four-vector in the Lorentz gauge as defined in [5]. $H_{NB}^{\mu\nu}$ is the hadronic tensor, it is the unknown object parametrized by the GPs.

In order to get an adequate parametrization of $H_{NB}^{\mu\nu}$ a multipole expansion is used in the CM frame. The multipole expansion is done in a spherical harmonic basis with its coefficients characterized by the multipoles : $H^{(\rho'L',\rho L)S}{}_{NB}(q'_{cm}, q_{cm})$. These unknown quantities will describe the electromagnetic transitions undergone by the proton. L (L') is the angular momentum of the initial (final) electromagnetic transition. S stands for the spin-nature of the transition: $S = 0$ (or $S = 1$) for a non-spin-flip transition (or a spin-flip transition). ρ (and ρ') characterizes the nature of the initial (final) multipole : $\rho = 0$ (charge), $\rho = 1$ (magnetic), $\rho = 2$ (electric) and $\rho = 3$ (longitudinal). But gauge invariance relates the charge and longitudinal multipoles, restricting ρ to (0,1,2).

An important step (detailed in [33]) uses parity symmetry, conservation of angular momentum and kinematical properties to express the expansion with only ten independent multipoles:

$$H^{(11,00)1}{}_{NB}, H^{(11,02)1}{}_{NB}, H^{(11,22)1}{}_{NB}, H^{(11,11)0}{}_{NB}, H^{(11,11)1}{}_{NB},$$
$$H^{(21,01)0}{}_{NB}, H^{(21,01)1}{}_{NB}, H^{(21,21)0}{}_{NB}, H^{(21,21)1}{}_{NB}, H^{(21,12)1}{}_{NB}, \qquad (1.31)$$

all being functions of q_{cm} and q'_{cm}. The low energy behavior of those multipoles is parametrized by introducing functions, which are the ten GPs:

$$P^{(\rho'L',\rho L)S}(q_{cm}) = Lim_{q'_{cm}\to 0} \ \frac{1}{q'_{cm}} \ \frac{1}{q_{cm}^L} H_{NB}^{(\rho'L',\rho L)S}(q'_{cm}, q_{cm}) \qquad (1.32)$$

with ρ', L', ρ L and S corresponding to the upper indices in equation 1.31. Drechsel et al. [35] have shown that some of these multipoles can be expressed as a function of the same GPs, reducing the number of independent GPs [33]:

$$
\begin{aligned}
H^{(11,00)1}{}_{NB}(q_{cm},q'_{cm}) &= q'_{cm}\left(\sqrt{3}\frac{q_{cm}^2}{\tilde{q}_{cm}^0}P^{(01,01)1}(q_{cm}) - \frac{1}{\sqrt{2}}q_{cm}^2 P^{(11,02)1}(q_{cm})\right) + O(q'^2_{cm}), \\
H^{(11,02)1}{}_{NB}(q_{cm},q'_{cm}) &= q'_{cm}q_{cm}^2 P^{(11,02)1}(q_{cm}) + O(q'^2_{cm}), \\
H^{(11,11)S}{}_{NB}(q_{cm},q'_{cm}) &= q'_{cm}q_{cm}P^{(11,11)S}(q_{cm}) + O(q'^2_{cm}), \\
H^{(21,01)S}{}_{NB}(q_{cm},q'_{cm}) &= -q'_{cm}q_{cm}\sqrt{2}P^{(01,01)S}(q_{cm}) + O(q'^2_{cm}), \\
H^{(21,12)1}{}_{NB}(q_{cm},q'_{cm}) &= -q'_{cm}q_{cm}^2\sqrt{2}P^{(01,12)1}(q_{cm}) + O(q'^2_{cm}), \\
H^{(11,22)1}{}_{NB}(q_{cm},q'_{cm}) &= q'_{cm}q_{cm}P^{(11,11)1}(q_{cm}) + O(q'^2_{cm}), \\
H^{(21,21)0}{}_{NB}(q_{cm},q'_{cm}) &= -q'_{cm}\tilde{q}_{cm}^0 P^{(11,11)0}(q_{cm}) + O(q'^2_{cm}), \\
H^{(21,21)1}{}_{NB}(q_{cm},q'_{cm}) &= -q'_{cm}\left(2\frac{q_{cm}^2}{\tilde{q}_{cm}^0}P^{(11,11)1}(q_{cm}) - \sqrt{2}q_{cm}^2 P^{(01,12)1}(q_{cm})\right) + O(q'^2_{cm}).
\end{aligned}
\qquad (1.33)
$$

Finally only 6 GPs are necessary to parametrized the hadronic tensor at first order in q'_{cm}, They are :

$$P^{(01,01)S=0,1}(q_{cm}), \ P^{(11,11)S=0,1}(q_{cm}), \ P^{(11,02)1}(q_{cm}), \ P^{(01,12)1}(q_{cm}). \qquad (1.34)$$

$S = 0$ and $S = 1$ correspond respectively to scalar and spin-flip (or spin) GPs.

This particular definition of GPs allows to find the connection with the polarizabilities from RCS. The electric polarizability is given by:

$$P^{(01,01)0}(q_{cm} = 0) = -\frac{4\pi}{e^2}\sqrt{\frac{2}{3}}\bar{\alpha}_E. \qquad (1.35)$$

The magnetic polarizability is given by:

$$P^{(11,11)0}(q_{cm} = 0) = -\frac{4\pi}{e^2}\sqrt{\frac{8}{3}}\bar{\beta}_M. \qquad (1.36)$$

Those relations can also be written at $Q^2 \neq 0$, e.g. $P^{(11,11)0}(Q^2) = -\frac{4\pi}{e^2}\sqrt{\frac{8}{3}}\beta_M(Q^2)$. The other four GPs are related to the spin-flip polarizabilities of RCS, the detail of this link can be found in [36].

Structure functions

Now that the amplitude is parametrized by the six GPs we are able to detail the term $[\mathcal{M}_0 - \mathcal{M}_0^{BH+B}]$ from equation 1.29. To do this it is convenient to define new observables: the structure functions. They are linear combinations of GPs expressed as :

$$P_{LL}(q_{cm}) = -2\sqrt{6}m_p G_E P^{(01,01)0}(q_{cm}), \qquad (1.37a)$$

$$P_{TT}(q_{cm}) = -3G_M \frac{q_{cm}^2}{\widetilde{q}_{cm}^0}(P^{(11,11)1}(q_{cm}) - \sqrt{2}\widetilde{q}_{cm}^0 P^{(01,12)1}(q_{cm})), \qquad (1.37b)$$

$$P_{LT}(q_{cm}) = \sqrt{\frac{3}{2}}\frac{m_p q_{cm}}{\widetilde{Q}}G_E P^{(11,11)0}(q_{cm}) + \frac{3}{2}\frac{\widetilde{Q}q_{cm}}{\widetilde{q}_{cm}^0}G_M P^{(01,01)1}(q_{cm}). \qquad (1.37c)$$

The important features to remind from these equations are the following:
- P_{LL} is proportional to the electric GP $\alpha_E(Q^2)$.
- P_{TT} is a combination of spin GPs.
- P_{LT} has a term proportional to the magnetic GP $\beta_M(Q^2)$ and a term proportional to a spin GP.
- the electric form factor G_E multiplies the scalar GPs.
- the magnetic form factor G_M multiplies the spin GPs.

The final expression of the photon electroproduction cross-section that we need to extract the GPs is :

$$\begin{aligned} \sigma^{LEX} = \ &\sigma^{BH+B} \\ &+\Phi q'_{cm}[v_{LL}(P_{LL}(q_{cm}) - \frac{P_{TT}(q_{cm})}{\epsilon}) + v_{LT}P_{LT}(q_{cm})] + O(q'^2_{cm}), \end{aligned} \qquad (1.38)$$

where v_{LL} and v_{LT} are kinematical coefficients, detailed in appendix A, which do not depend on q'_{cm} but on $(q_{cm}, \ \epsilon, \ \theta_{cm}, \varphi)$. Here again, σ is a short notation for $d^5\sigma^{exp}/dk'd\Omega_{k'}d\Omega_{p'_{cm}}$.

Chapter 2

Theoretical models and motivations for a VCS experiment

In this chapter the theoretical models and their GP predictions are introduced, then the results obtained by the previous VCS experiments are presented.

Section 2.1 details the dispersion relation model, which has to be separated from the others since it is the only one which allows a direct extraction of GPs from an unpolarized experiment. In contrast, the LEX approach described in chapter 1 only allows to extract structure functions, i.e. linear combinations of GPs.

Section 2.2 introduces the other theoretical models and presents their GP predictions.

Section 2.3 reviews the previous experiments and their results.

In the last section 2.4 the context of our GP extraction is presented and the motivations for performing this new experiment are explained.

2.1 The Dispersion Relation model

The dispersion relation (DR) model was developed by B. Pasquini et al. [37] [38] for RCS and VCS. One of its features is that it cannot predict the scalar GPs behavior versus Q^2. Indeed, in the model, these GPs contain parameters that are free. The positive consequence is that we can use the DR model to realize a GP extraction by comparing its calculation to our experimental data (of course the extraction will then be model-dependent). In this section only the basics of the DR model are introduced, the details of our DR analysis will be discussed later in section 5.6.

2.1.1 Formalism of the model

The polarizabilities are elementary structure constants of every composite system, from protons to macroscopic media. For each system the dipole polarizabilities describe how it reacts to an external electromagnetic field. For a macroscopic medium this phenomenological description is done thanks to the dispersion theory and leads to the Kramers-Kronig dispersion relations. So the idea is to apply the

dispersion theory to the proton in order to describe the VCS process and access the GPs.

The twelve DR model amplitudes

The construction of the model for RCS and VCS is presented in [38], and its particular application to VCS is further detailed in [37]. This part presents only the three important steps which are related to the three physics principles that intervene in the model construction: relativistic covariance, causality and unitarity. The goal is to calculate the particular VCS amplitude:

$$T^{VCS} = T^B + T^{NB}, \tag{2.1}$$

and more precisely to express the VCS tensor :

$$M^{\mu\nu} = M_B^{\mu\nu} + M_{NB}^{\mu\nu}. \tag{2.2}$$

We start with the definition of variables used in the DR formalism, the Mandelstam variables:

$$s = (\mathbf{q} + \mathbf{p})^2, \quad t = (\mathbf{q} - \mathbf{q'})^2, \quad u = (\mathbf{q} - \mathbf{p'})^2 \tag{2.3}$$

and an additional variable, ν, defined as :

$$\nu = \frac{s-u}{4m_p}. \tag{2.4}$$

Then the first step is to construct a complete set of twelve amplitudes in accordance with relativity principles [39]. An important property for setting up a DR formalism is for those twelve amplitudes to not contain kinematical singularities, thereafter the VCS tensor becomes:

$$M^{\mu\nu} = \sum_{i=1}^{12} F_i(Q^2, \nu, t)\rho_i^{\mu\nu}, \tag{2.5}$$

with $\rho_i^{\mu\nu}$ being twelve independent tensors and $F_i(Q^2, \nu, t)$ the amplitudes.

The second step consists in the application of causality that requires certain analytic properties of the amplitudes. This leads to relations connecting the real and imaginary parts of the amplitudes, just like the Kramers-Kronig relation, the so-called unsubtracted dispersion relation:

$$Re[F_i^{NB}(Q^2, \nu, t)] = \frac{2}{\pi}\mathcal{P}\int_{\nu_{thr}}^{+\infty} d\nu' \frac{\nu' Im_s[F_i(Q^2, \nu', t)]}{\nu'^2 - \nu^2}, \tag{2.6}$$

with $Re[F_i^{NB}(Q^2, \nu, t)]$ the real part of the non-Born amplitudes at fixed Q^2 and t. $Im_s[F_i(Q^2, \nu', t)]$ is the imaginary part of the VCS amplitudes above the pion production threshold, defined[1] by: $\nu \geq \nu_{thr} = m_\pi + (m_\pi^2 + t/2 + Q^2/2)/(2m_p)$.

---

[1]m_π is the pion mass.

28

The third and last step is based on the use of unitarity to replace the imaginary part of equation 2.6 by the absorption amplitudes. The absorption amplitudes represented in figure 2.1 represent all possible intermediate states X other than one single nucleon. But being at low energy, only the dominant term of an intermediate pion-nucleon state (πN) is considered in the DR model. The amplitudes for $(\gamma^* p \to \pi N)$ and $(\pi N \to \gamma p')$ are obtained thanks to the MAID model from [40] including both resonant and non-resonant contributions.
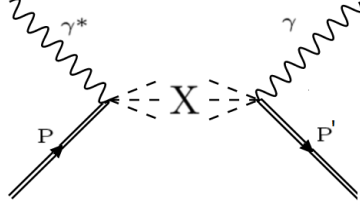
Figure 2.1: The absorptive part of the $\gamma^* p \to \gamma p'$ reaction.

Finally, to express GPs from this formalism one has to consider that GPs are defined at the limit $q'_{cm} \to 0$. In the DR model, this corresponds to the limit: $\nu \to 0$ and $t \to -Q^2$ at finite Q^2. Therefore, the GPs are expressed as linear combinations of the invariant amplitudes $F_i^{NB}(Q^2, \nu = 0, t = -Q^2)$.

The particular case of the F_1, F_5 and F_2 amplitudes

To satisfy the dispersion relation 2.6 the imaginary amplitudes have to drop fast enough at high energy, which is not the case for two of the twelve amplitudes, $F_1(Q^2, \nu, t)$ and $F_5(Q^2, \nu, t)$. Therefore it was decided to add an asymptotic behavior to the dispersion relation 2.6 which becomes:

$$ReF_{1,5}^{NB}(Q^2, \nu, t) = \frac{2}{\pi}\mathcal{P}\int_{\nu_{thr}}^{\nu_{max}} d\nu' \frac{\nu' Im_s F_{1,5}(Q^2, \nu', t)}{\nu'^2 - \nu^2} + F_{1,5}^{as}(Q^2, \nu, t), \qquad (2.7)$$

with ν_{max} fixed in the model at 1.5 GeV and $F_{1,5}^{as}(Q^2, \nu, t)$ the asymptotic contribution. The asymptotic contributions are treated differently for F_5 and F_1.

The $F_5(Q^2, \nu, t)$ amplitude intervenes in the determination of the spin-flip GPs and its asymptotic contribution is fixed in the model. Therefore the DR model cannot be used to extract the spin-flip GPs from experimental data.

The $F_1(Q^2, \nu, t)$ amplitude is related to the magnetic GP $\beta_M(Q^2)$ and its asymptotic contribution is not fixed in the model. So the $F_1(Q^2, \nu = 0, t = -Q^2)$ asymptotic contribution depends on a free parameter Λ_β which appears in the expression of $\beta_M(Q^2)$:

$$\beta_M^{DR}(Q^2) = \beta_M^{\pi N}(Q^2) + \frac{[\beta_M(Q^2) - \beta_M^{\pi N}(Q^2)]_{Q^2=0}}{(1 + Q^2/\Lambda_\beta^2)^2}. \qquad (2.8)$$

Λ_β is a free parameter that has to be fitted on experimental data to extract $\beta_M(Q^2)$. The dipole form in equation 2.8 is arbitrary. It provides nevertheless an easy parametrization of the Q^2-dependence of $\beta_M^{DR}(Q^2)$ asymptotic part.

$F_2(Q^2, \nu, t)$ is the next amplitude discussed here, it is related to the sum $\beta_M(Q^2) + \alpha_E(Q^2)$. Even if this amplitude satisfies the dispersion relation 2.6 one has still to consider contributions beyond πN in the calculation of its imaginary part. Indeed the use of DR to the RCS case has shown that approximating the imaginary amplitude to πN contributions only, failed to predict $\beta_M(Q^2 = 0)$ precisely enough. One has to consider higher orders that are not calculated yet. To this aim, an asymptotic contribution is also considered for $F_2(Q^2, \nu, t)$. That finally leads to the following DR expression of $\alpha_E(Q^2)$:

$$\alpha_E^{DR}(Q^2) = \alpha_E^{\pi N}(Q^2) + \frac{[\alpha_E(Q^2) - \alpha_E^{\pi N}(Q^2)]_{Q^2=0}}{(1 + Q^2/\Lambda_\alpha^2)^2}, \tag{2.9}$$

where Λ_α is the second free parameter of the model.

2.1.2 Results of calculation in the DR model

One may wonder which contribution is more relevant in the DR model for the scalar GPs: the πN one or the asymptotic one. Figure 2.2 displays the asymptotic and πN contributions for the two scalar GPs (these results are obtained with an arbitrary choice : $\Lambda_\alpha = \Lambda_\beta = 0.7\ GeV$). As it appears the electric GP is dominated by its asymptotic contribution while the magnetic GP is a sensitive interplay between the two contributions.
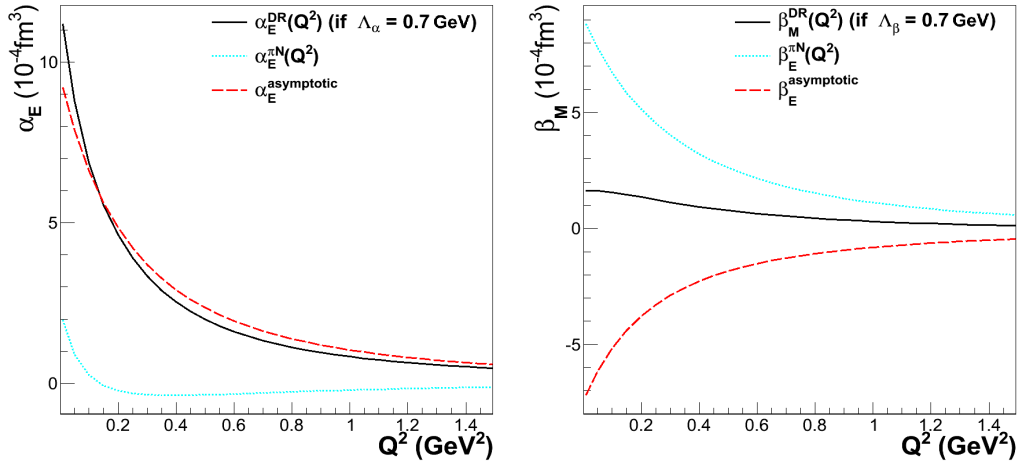
Figure 2.2: Scalar GPs from the DR model for fixed parameters $\Lambda_\alpha = \Lambda_\beta = 0.7\ GeV$. The red dashed line is the asymptotic contribution, the blue dotted line is the πN contribution and the black full line is the sum of the two.

One has to carefully consider the result of figure 2.2. Indeed the dipole shape that appears is only caused by our choice to keep the Λ parameters constant for all Q^2. In fact the DR model does not specify a Q^2 behavior, and the Λ's are only intermediate parameters than can vary with Q^2. As another illustration of that, figure 2.3 shows different values for different Λ from 0.3 to 1.1 GeV (here again the choice of keeping Λ constant along Q^2 determines the shape).
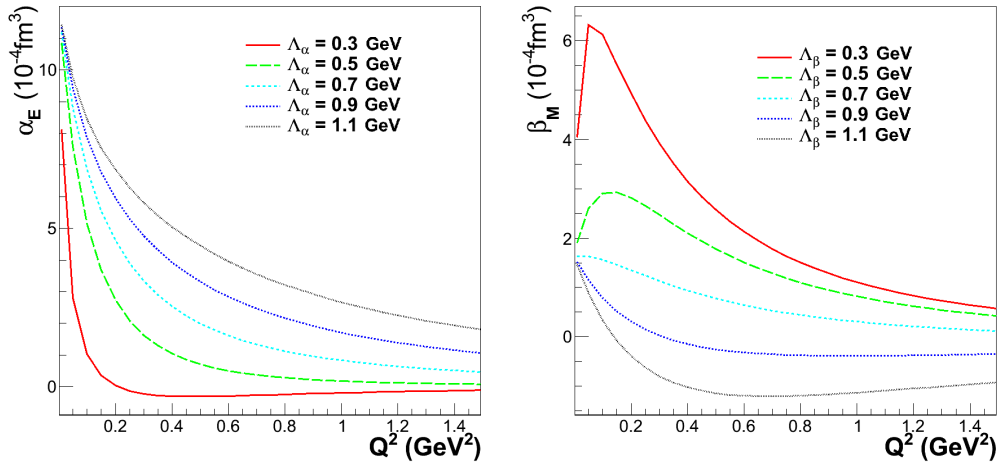
Figure 2.3: Scalar GPs from the DR model for different values of the Λ parameters. Red full line $\Lambda = 0.3 \; GeV$, green dashed line $\Lambda = 0.5 \; GeV$, light blue light dashed line $\Lambda = 0.7 \; GeV$, dark blue dotted line $\Lambda = 0.9 \; GeV$ and black line $\Lambda = 1.1 \; GeV$.

Physical interpretations of GP contributions are proposed in the model. For the magnetic GP, the paramagnetic contribution would correspond to $\beta_M^{\pi N}(Q^2)$ while $\beta_M^{asympt}(Q^2)$ would be the diagmagnetic contribution interpreted as the exchange of an effective σ-meson in the t-channel.

For the electric GP, $\alpha_E^{asympt}(Q^2)$, i.e. the contributions beyond (πN) (typically the $(\pi\pi N)$ intermediate states) dominate.

The DR model offers a solid description of VCS, it predicts the behavior of spin-flip GPs and approximates the behavior of scalar GPs as a function of two free parameters Λ_α and Λ_β. Thanks to these free parameters one can use the DR model to extract scalar GPs from experimental data. This model also has the advantage to be valid above the pion production threshold, up to $\sqrt{s} = 1.28 \; GeV$, and for a broad range of Q^2.

Although the model focuses on the VCS process, it has the merit to provide also the calculation of the full photon electroproduction process, i.e. including the Bethe-Heitler part, and making it directly comparable to experiment.

It is important to emphasize the role of the DR model in our GP extraction from the LEX analysis. Since the relation between structure functions and scalar GPs depends on spin-flip GPs, which remain experimentally unknown, the LEX approach based on equation 1.38 is powerless to obtain GPs directly. We will need a prediction of the spin-flip GPs in order to fix these quantities in equations 1.37 and for this task we chose the DR model prediction.

2.2 Other models

The other models are predictive, in the sense that they predict all the GPs with no free parameters. While they cannot be used for a GP extraction from experiment, it is still interesting to compare their calculations.

2.2.1 Chiral perturbation theories

The chiral perturbation theory (χPT) is an effective field theory that successfully calculates meson properties. In χPT the chiral symmetry and its breaking are implemented to a low-energy Lagrangian. Then the theory of perturbation is used to expand the calculation along a chosen quantity of the considered interaction; for instance the proton four-momentum and the order n at which the calculation stops are written as $O(p^n)$. That way, chiral perturbation theories predict fundamental quantities, among which the RCS polarizabilities, the scalar GPs and the spin GPs. The first description of χPT was done by Weinberg [41], more information about such theories applied to baryons can be found in the review paper from V. Bernard [42].

For VCS two different chiral perturbation theories give a prediction for the GPs: the heavy baryon chiral perturbation theory (HBχPT) [43] and the baryon chiral perturbation theory (BχPT) [44]. For both, all the low-energy constants that appear in the constructed Lagrangian are known. So these highly constrained models will predict GP values to compare with experimental data.

The BχPT just extends the theory to include a matter field. So a new effective meson-baryon Lagrangian is constructed. The theory only considers the three low-mass quarks (u,d,s), the SU(3) flavor symmetry and the eight pseudo-scalar mesons that result from its breaking (the pions, the kaons and the η). The results presented in table 2.2.1 were obtained by V. Bernard et al. [45] at order $O(p^3)$.

In the HBχPT framework the nucleon is considered as extremely heavy, and so non-relativistic. This idea was introduced by Jenkins and Manohar [46] and requires to use the SU(2) symmetry instead of SU(3). As a result only three pseudo-scalars are predicted by the breaking of the symmetry, they are the pions. Thus the model introduces the nucleon's pion cloud and its interaction with the VCS photon. Figure 2.4 shows the diagrams typically calculated and the HBχPT calculation of GPs from [47] is drawn in figure 2.6.
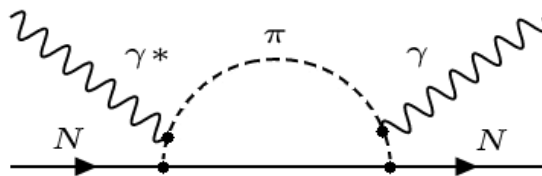
Figure 2.4: Typical pion loop diagram for Compton scattering.

The $\Delta(1232)$-resonance is ignored by theses theories, but it has been shown that including the $\Delta(1232)$-resonance as an explicit degree of freedom impacts significantly the predictions. Furthermore, in their paper [48] Lensky et al. performed a new Lorentz-covariant calculation of the RCS electric and magnetic polarizabilities. Considering both the $\Delta(1232)$-resonance and the new Lorentz-covariant calculation deeply impacts the predictions; results obtained by this approach are labeled as "NEW" in table 2.2.1.

Table 2.2.1 from [48] illustrates a variety of results provided by χPT theories. The predictions are presented for BχPT and HBχPT; the calculations are done up

to the order $O(p^3)$ and even $O(p^4)$ for "NEW" (but the $\Delta(1232)$-resonance is not considered at the $O(p^4)$ order) . The compilation of RCS measurements from [28] is shown as a comparison.

	BχPT	BχPT (NEW)	HBχPT	HBχPT (NEW)	PDG [28]
$\bar{\alpha}_E$ $(10^{-4}fm^3)$	6.8	10.8	12.2	20.8	11.5±0.4
$\bar{\beta}_M$ $(10^{-4}fm^3)$	-1.8	4.0	1.2	14.7	2.5±0.4

Table 2.2.1 : RCS electric and magnetic polarizability predictions from different BχPT and HBχPT calculations as presented in [48].

As it appears from table 2.2.1, there is a large sensitivity to the calculation choice in χPT predictions. Also, BχPT and HBχPT are in poor agreement.

2.2.2 Effective Lagrangian model

The effective Lagrangian model was elaborated by M.Vanderhaeghen [49], it consists in a phenomenological approach to calculate the polarizabilities. The idea is to evaluate the Non-Born contribution to photon electroproduction by summing the Feynman diagrams of dominant intermediate states.

This relativistic model calculates the contributions of the non-Born diagrams represented in figure 2.5, with N^* representing the following intermediates states : $\Delta(1232)$, $P_{11}(1440)$, $D_{13}(1520)$, $S_{11}(1535)$, $S_{31}(1620)$, $S_{11}(1650)$ and $D_{33}(1700)$. The electromagnetic couplings of these resonances are adjusted on photo-decay amplitude fits to experimental data. The X symbol of figure 2.5 stands for the π^0 or the σ $(\pi\pi)$ meson and the coupling constants are deduced from other models (more informations are given in [49]).

The main limitation to the model comes from the evaluation of the $\pi\gamma\gamma$ coupling constant. Indeed the experimental photo-decay amplitude only fixes the on-shell effects. This may explain the discrepancy between the experimental RCS polarizabilities and the ones predicted by the model.

A new determination of polarizabilities was performed in an effective Lagrangian model framework [50]. In this work a more general treatment of the $\Delta(1232)$ contribution was implemented by adding an off-shell degree of freedom. This calculation is drawn in figure 2.6. The prediction of $\alpha_E(Q^2 = 0)$ is still in bad agreement with the experimental values, as for the work of reference [49].

2.2.3 Linear sigma model

In the linear sigma model (LSM), originally developed in reference [51], the proton structure is described by a pointlike nucleon that interacts with pions and sigmas. The LSM was developed for VCS by A. Metz and D. Drechsel [52][32] and was the first model to give a prediction of neutron scalar GPs. It is built in order to respect all the relevant symmetries like Lorentz symmetry, gauge invariance and chiral invariance. It also satisfies the partially conserved axial current relation (PCAC [53][54]) which represents spontaneous breaking of the chiral symmetry and is an important relation to describe hadron physics at low energy. The PCAC
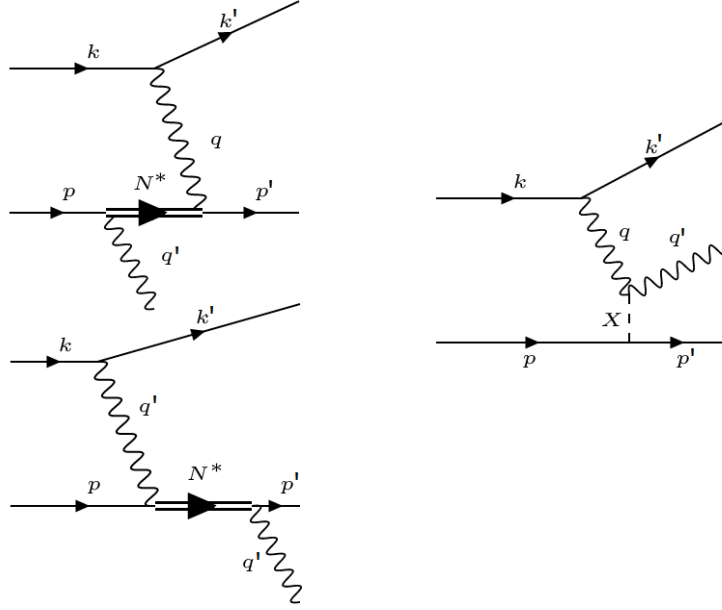
Figure 2.5: VCS Non-Born diagrams calculated in the effective Lagrangian model [49]. The N^* and X symbols are specified in the text.

relation gives rise to the Goldberger-Treiman relation [55] that is used to determine the pion-nucleon coupling constant $g_{\pi N}$:

$$g_{\pi N} = g_A \frac{m_N}{F_\pi} = 13.4, \tag{2.10}$$

with m_N the nucleon mass, g_A the axial coupling constant and F_π the pion decay constant. $g_{\pi N}$ is used to calculate all the one-loop diagrams (figure 2.4) contributing to the GPs.

The LSM considers an infinite sigma mass to avoid all the Feynman diagrams containing the sigma propagator. The calculation [52][32] predicts the following RCS polarizabilities:

$$\bar{\alpha}_E = 7.5 \cdot 10^{-4} \ fm^3 \ ,$$
$$\bar{\beta}_M = -2 \cdot 10^{-4} \ fm^3.$$

Since the LSM ignores the $\Delta(1232)$-resonance the magnetic polarizability is low. The Q^2-behavior of scalar and spin GPs according to LSM is represented in figure 2.6.

2.2.4 The non-relativistic quark model nRQM

The nRQM is a general model for nucleon structure which was introduced by O. W. Greenberg and Resnikoff [56]; it was later improved by Isgur and Karl [57]. The strength of the model comes from its simplicity; indeed, in the approximation of equal masses for quarks only three parameters define the model:
- The quark mass which is fixed thanks to the proton magnetic moment.

- The harmonic oscillator energy which is fixed to reproduce the mass difference between the baryon resonances.

- The chromatic fine structure constant α_s which explains the mass degeneracy between the proton and the $\Delta(1232)$.

The model was then adapted to Compton scattering and polarizabilities by G. Q. Liu et al. [58]. It considers that the electric polarizability is ruled by the electromagnetic transition E1 between the proton and its resonances. The magnetic polarizability is deduced from the M1 transition P$\rightarrow \Delta(1232)$.

The model was later reconsidered by B. Pasquini, S. Scherer and D. Drechsel [59] for a new prediction of GPs. The following resonances were used: $D_{13}(1520)$, $S_{11}(1535)$, $S_{31}(1620)$, $S_{11}(1650)$, $S_{13}(1700)$, $D_{33}(1700)$ and recoil effects were implemented in the model. The following values were predicted for the scalar RCS polarizabilities:

$$\bar{\alpha}_E = 5.5 \cdot 10^{-4} \ fm^3 \ ,$$
$$\bar{\beta}_M = 4.7 \cdot 10^{-4} \ fm^3.$$

The predicted behavior of GPs is represented in figure 2.6. As mentioned in [59] there is room to improve the model since it does not take into account important considerations such as relativity, gauge invariance and chiral symmetry. However the predictions provide an order-of-magnitude estimation for the nucleon resonance contributions.

As a conclusion, figure 2.6 from [59] shows the predictions of all the presented models. Models agree on a smooth fall-off shape for the electric GP, they also agree to predict a more complicated shape for the magnetic GP. The spin-flip GP predictions are rarely in agreement from a model to another.

As a more general conclusion, the polarizabilities in RCS and furthermore in VCS are good observables to test the validity of various models of nucleon structure. Experimental data on polarizabilities are therefore welcome, and the present thesis is part of this experimental effort.

2.3 Previous and current VCS Experiments

In this section we will remind the previous scalar GPs measurements by presenting the explored phase space, the results and the specificities of each analysis. Then we will briefly introduce a recent measurement at MAMI that uses the Δ resonance to extract the electric GP at $Q^2 = 0.2 \ GeV^2$.

2.3.1 The first MAMI experiment

The very first dedicated VCS experiment has been performed in 1996 at MAMI by the A1 collaboration [7]. This experiment is quite similar to the one presented in this thesis. The absolute photon electroproduction differential cross section has been measured at a virtuality $Q^2 = 0.33 \ GeV^2$ and $\epsilon = 0.62$.

The beam energy was about 855 MeV. The scattered electron and the recoiling proton were detected in coincidence with the same two high-resolution magnetic
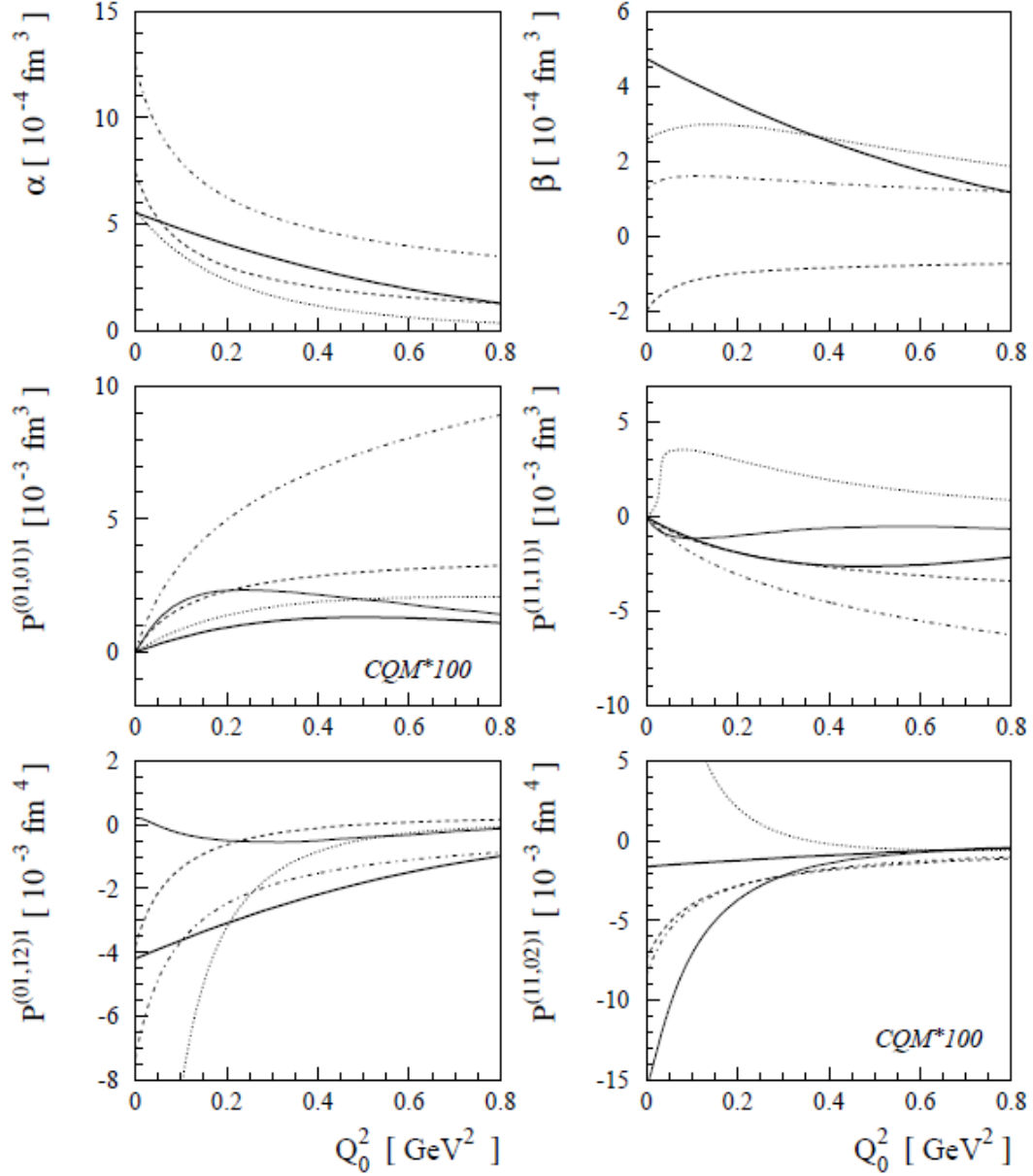
Figure 2.6: Results for the six GPs in different model calculations as a function of $\tilde{Q}^2$. Full line: nRQM ("CQM*100") [59], dashed line: linear sigma model [52], dotted line: effective Lagrangian model [50], dashed-dotted lines: HBχPT [47], full thin lines: dispersion-relation calculation [60]. Figure taken from [61].

spectrometers that we used: A and B. The same liquid hydrogen target of 49.5 mm long was also used.

The explored phase space was defined by:

- a range in q'_{cm} going from low q'_{cm} (33.6 MeV/c) for the renormalization, up to close to the pion production threshold ($q'_{cm}(max) = 111.5 \; MeV/c$).

- an in-plane measurement, mostly at $\varphi = 180°$(which is the hemisphere opposite to the BH peaks).

- basically all polar angles of the final photon, with θ_{cm} from -141°to 6°.

The LEX approach was used to extract the structure functions with the following results [7]:

$$P_{LL} - P_{TT}/\epsilon = (23.7 \pm 2.2 \pm 0.6 \pm 4.3) \ GeV^{-2} \ ,$$
$$P_{LT} = (-5.0 \pm 0.8 \pm 1.1 \pm 1.4) \ GeV^{-2}.$$

The first error is statistical only. The two others are systematic: the first one corresponds to the normalization of the angular distributions, the second one stems from the distortion of the distributions.

Later, a DR analysis was performed and confirmed the results [62] (table 4, method 4):

$$P_{LL} - P_{TT}/\epsilon(DR) = (23.2 \pm 3.0) \ GeV^{-2} \ ,$$
$$P_{LT}(DR) = (-3.2 \pm 2.0) \ GeV^{-2},$$

where the errors are purely statistical.

2.3.2   JLab VCS experiment (E93-050)

The JLab measurements were performed in 1998 [63] [64]. An electron beam of 4.030 GeV energy was directed onto a 15 cm liquid hydrogen target. The two high-resolution spectrometers of Hall A were used to detect the scattered electron and the outgoing proton in coincidence.

Extractions of GPs were done at two setups (I and II) corresponding to two values of Q^2 : 0.92 and 1.76 GeV^2 for an ϵ of respectively 0.95 and 0.88. The setup-I at $Q^2 = 0.92 \ GeV^2$ was split in two settings : I-a that contained events under pion production threshold and I-b that was exploring the $\Delta(1232)$ resonance. Measurements were done with in-plane and out-of-plane data.

The cross sections were calculated using the proton form-factor parametrization from Brash et al. [65]. Both LEX and DR analysis have been performed (since the I-b setting was above the pion production threshold no LEX approach was used for it). Table 2.3.2 presents the results for the structure functions.

analysis	Q^2 (GeV^2)	$P_{LL} - P_{TT}/\epsilon$ (GeV^{-2})	P_{LT} (GeV^{-2})
I-a LEX	0.92	$1.77 \pm 0.24 \pm 0.70$	$-0.56 \pm 0.12 \pm 0.17$
I-a DR	0.92	$1.70 \pm 0.21 \pm 0.89$	$-0.36 \pm 0.10 \pm 0.27$
I-b DR	0.92	$1.50 \pm 0.18 \pm 0.19$	$-0.71 \pm 0.07 \pm 0.05$
II LEX	1.76	$0.54 \pm 0.09 \pm 0.20$	$-0.04 \pm 0.05 \pm 0.06$
II DR	1.76	$0.40 \pm 0.05 \pm 0.16$	$-0.09 \pm 0.02 \pm 0.03$

Table 2.3.2 : JLab structure function measurement for all settings and both types of analysis. The first error is statistical, the second is systematic.

2.3.3 MIT-Bates experiment

The MIT-Bates experiment was performed in 2000-2001 [66][67]. In this experiment the GPs were extracted at a very low Q^2 of 0.057 GeV^2 and $\epsilon = 0.9$. The target was 1.6 cm of liquid hydrogen and the experiment used Out-of-Plane Spectrometers for proton detection.

The Bates VCS experiment was designed to make an azimuthal separation of $P_{LL} - P_{TT}/\epsilon$ and P_{LT} by taking data simultaneously at φ angles of 90°, 180°and 270°, at fixed $\theta_{cm} = 90°$. Data were taken at photon energies q'_{cm} ranging from 43 MeV up to 115 MeV.

Both DR and LEX analyses have been performed with very different results for P_{LT}:

$$P_{LL} - P_{TT}/\epsilon(DR) = (46.7 \pm 4.9_{stat} \pm 3.4_{syst}) \ GeV^{-2} \ ,$$
$$P_{LT}(DR) = (-8.9 \pm 4.2_{stat} \pm 1.4_{syst}) \ GeV^{-2}.$$
$$P_{LL} - P_{TT}/\epsilon(LEX) = (54.5 \pm 4.8_{stat} \pm 3.4_{syst}) \ GeV^{-2} \ ,$$
$$P_{LT}(LEX) = (-20.4 \pm 2.9_{stat} \pm 1.4_{syst}) \ GeV^{-2}.$$

The Bates experiment was the first one to explicitly show that one has to carefully use the LEX. Indeed the LEX extraction is only valid in kinematics where $\mathcal{O}(q'_{cm}{}^2)$ in equation 1.38 is small enough to be neglected. The Bates experiment proved that the higher orders had a strong impact on its in-plane kinematics (where $\varphi = 180°$) and were responsible of the large difference between the LEX and DR P_{LT} values.

From the RCS electric polarizability and this new measurement one was able to determine the polarization radius of the proton: $< r_\alpha >$. This radius, which is about twice larger than the proton charge radius, is an evidence of the mesonic effects in the electric polarizability.

2.3.4 The Doubly polarized VCS experiment at MAMI

In 2005-2006 a new experiment was done at MAMI [68][69]. This experiment has been performed at $\epsilon = 0.645$ and at the same Q^2 as the first one, 0.33 GeV^2, with the aim of gaining insight into the proton spin-flip GPs for the first time. This requires to measure doubly polarized VCS. The studied reaction was then $e\vec{p} \to e'\vec{p}'\gamma$, obtained thanks to the MAMI capacity to produce a polarized electron beam; the outgoing proton polarization was measured by a focal-plane polarimeter.

The $P_{LT}^{\perp}$ structure function was extracted for the first time. Since this experiment is kinematically close to the first MAMI experiment the scalar GPs were also extracted, by an unpolarized analysis, in order to confirm the previous result.

Only a LEX analysis was performed, with several different parametrizations for the proton form factors. The $P_{LL} - P_{TT}/\epsilon$ results are in agreement from a parametrization to an other but important variations were observed for P_{LT}. With the Friedrich-Walcher parametrization of form factors [17] the following structure functions were extracted:

$$P_{LL} - P_{TT}/\epsilon = (27.1 \pm 1.9_{stat} \pm 3.0_{syst}) \ GeV^{-2} \ ,$$
$$P_{LT} = (-8.0 \pm 0.7_{stat} \pm 2.2_{syst}) \ GeV^{-2}.$$

An iterative approach was used to determine the final values, i.e. the obtained structure functions were reintroduced in the LEX analysis at each step. The comparison with the first MAMI experiment tends to confirm the non-trivial Q^2 behavior observed in this region.

2.3.5   The "VCS Δ" experiment at MAMI

In parallel to our experiment, another VCS experiment was performed at MAMI in 2013 at $Q^2 = 0.2 \ GeV^2$ and is currently in the very end of the analysis process [70]. It also uses the standard A1 setup, with the two spectrometers A and B detecting the outgoing electron and proton and using the 49.5 mm long liquid hydrogen target. But the measured phase space is different since this experiment explores the $\Delta(1232)$ resonance region, i.e. above the pion production threshold.

So this experiment did not use a LEX approach but measured the in-plane azimuthal asymmetry of the photon electroproduction cross section:

$$A_{(\varphi=0)} = [\sigma_{\varphi=0} - \sigma_{\varphi=180}]/[\sigma_{\varphi=0} + \sigma_{\varphi=180}], \qquad (2.11)$$

which is sensitive to both the electric GP and the Coulomb quadrupole amplitude (C2)^2. The experiment aims to extract these two quantities. The sensitivity to each one varies in a different way versus θ_{cm}. A large range in θ_{cm} is then explored in order to extract those two quantities from the same reaction channel.

Above the pion production threshold the only way to access $\alpha_E(Q^2)$ is thanks to the DR model, so the experiment will provide a model-dependent extraction of the electric GP, that will be compared with our own results at the same value of $Q^2 = 0.2 \ GeV^2$.

2.4   Motivation for a new experiment: "vcsq2"

This section describes the motivations for our experiment [8] which is designed to extract the electric and magnetic GP at three new values of $Q^2 = 0.1; 0.2; 0.45$ GeV^2.

Since 1996 a series of VCS experiments performed at MAMI, JLab and Bates have provided experimental results for the electric and magnetic GPs at different Q^2 values from 0.06 GeV^2 to 1.76 GeV^2. Bates and JLab measurements were at respectively very low and very high Q^2 while MAMI was exploring the intermediate range. The results are gathered in table 2.4.

---

^{2}C2 gives us information about the sphericity of the proton.

Experiment	Q^2 (GeV^2)	ϵ	$P_{LL} - P_{TT}/\epsilon$ (GeV^{-2})	P_{LT} (GeV^{-2})
LEX analysis				
MIT-Bates [67]	0.057	0.90	$54.5 \pm 4.8 \pm 3.4$	$-20.4 \pm 2.9 \pm 1.4$
MAMI first [62]	0.33	0.62	$23.7 \pm 2.2 \pm 0.6 \pm 4.3$	$-5.0 \pm 0.8 \pm 1.1 \pm 1.4$
polar-MAMI [69]	0.33	0.645	$27.1 \pm 1.9 \pm 3.0$	$-8.0 \pm 0.7 \pm 2.2$
JLab (I-a) [63]	0.92	0.95	$1.77 \pm 0.24 \pm 0.70$	$-0.56 \pm 0.12 \pm 0.17$
JLab (II) [63]	1.76	0.88	$0.54 \pm 0.09 \pm 0.20$	$-0.04 \pm 0.05 \pm 0.06$
DR analysis				
MIT-Bates [67]	0.057	0.90	$46.7 \pm 4.9 \pm 3.4$	$-8.9 \pm 4.2 \pm 1.4$
MAMI first [62]	0.33	0.62	$23.2 \pm 3.0_{stat}$	$-3.2 \pm 2.0_{stat}$
JLab (I-a) [63]	0.92	0.95	$1.70 \pm 0.21 \pm 0.89$	$-0.36 \pm 0.10 \pm 0.27$
JLab (I-b) [63]	0.92	0.95	$1.50 \pm 0.18 \pm 0.19$	$-0.71 \pm 0.07 \pm 0.05$
JLab (II) [63]	1.76	0.88	$0.40 \pm 0.05 \pm 0.16$	$-0.09 \pm 0.02 \pm 0.03$

Table 2.4 : Structure functions world data. The first error is statistical, the second is systematic.

Table 2.4-bis contains the world data for $\alpha_E(Q^2)$ and $\beta_M(Q^2)$. The presented LEX analyses show values obtained by a DR-subtraction of the spin-flip GPs.

Experiment	Q^2 (GeV^2)	ϵ	$\alpha_E(Q^2)$ $(10^{-4}fm^3)$	$\beta_M(Q^2)$ $(10^{-4}fm^3)$
LEX analysis				
MIT-Bates*	0.057	0.9	$9.22 \pm 0.85 \pm 0.60$	$6.77 \pm 1.04 \pm 0.48$
MAMI first*	0.33	0.62	$6.90 \pm 0.72 \pm 1.41$	$2.52 \pm 0.50 \pm 1.11$
polar-MAMI*	0.33	0.645	$8.05 \pm 0.62 \pm 0.98$	X
JLab (I-a)*	0.92	0.95	$1.04 \pm 0.20 \pm 0.57$	$0.40 \pm 0.18 \pm 0.25$
JLab (II)*	1.76	0.88	$0.85 \pm 0.19 \pm 0.42$	$-0.10 \pm 0.17 \pm 0.21$
DR analysis				
MIT-Bates [67]	0.057	0.90	$7.85 \pm 0.87 \pm 0.60$	$2.69 \pm 1.48 \pm 0.49$
MAMI first*	0.33	0.62	$6.75 \pm 0.98_{stat}$	$1.39 \pm 1.26_{stat}$
JLab (I-a) [63]	0.92	0.95	$1.02 \pm 0.18 \pm 0.77$	$0.13 \pm 0.15 \pm 0.42$
JLab (I-b) [63]	0.92	0.95	$0.85 \pm 0.15 \pm 0.16$	$0.66 \pm 0.11 \pm 0.07$
JLab (II) [63]	1.76	0.88	$0.52 \pm 0.12 \pm 0.35$	$0.10 \pm 0.07 \pm 0.12$

Table 2.4-bis: Generalized polarizabilities world data. The first error is statistical, the second is systematic. The star stands for values that we calculated ourselves with the DR code (described section 5.1.2) from the published LEX structure functions of table 2.4, the X means that we were not able to compute a DR value from the structure function.

Although all models (except the DR model) predict a single-dipole behavior for $\alpha_E(Q^2)$ the two MAMI experiments at $Q^2 = 0.33\ GeV^2$ seem to contradict this prediction. The $\alpha_E(Q^2)$ single-dipole behavior is translated in a smooth fall-off for the $P_{LL} - P_{TT}/\epsilon$ structure function (the predictions of the DR model are presented in appendix B). Figure 2.7 represents the world measurements for the structure function $P_{LL} - P_{TT}/\epsilon$. In the figure the DR prediction, if one fixes $\Lambda_\alpha = 0.7\ GeV$

for all Q^2, is represented as the dashed curve. This clearly shows the tension between the three-times confirmed $Q^2 = 0.33 \, GeV^2$ measurement and the smooth fall-off described by the curve and the other data points.

Figure 2.7: World measurements of $P_{LL} - P_{TT}/\epsilon$ performed at JLab, Bates and MAMI by LEX analysis (empty red crosses) and DR analysis (full blue crosses) with statistical (inner) and total (quadratically summed, outer) error bars. The DR model prediction assuming a dipole behavior for the asymptotic part of $\alpha_E(Q^2)$ with $\Lambda_\alpha = 0.7$ GeV, and a fixed $\epsilon = 0.85$ is also plotted (light blue dashed line). The measurements are done at different ϵ, the exact values are specified in table 2.4. Some points are shifted in Q^2 for visibility.

This situation was the physical motivation to explore in more depth the intermediate Q^2 range with a new VCS MAMI-experiment, at Q^2 values that will surround the previous one: $Q^2 = 0.1 \, GeV^2$, $Q^2 = 0.2 \, GeV^2$ and $Q^2 = 0.45 \, GeV^2$. I was in charge of analysing the $Q^2 = 0.2 \, GeV^2$ data set and two PHD students were in charge of the other data sets [71][72].

The world results for the second structure function P_{LT} are represented with respect to Q^2 in figure 2.8. For P_{LT}, and so for the magnetic GP, some models predict a Q^2-shape that contains an extremum in the low-Q^2 region, due to the interplay between the paramagnetic and the diamagnetic proton responses. But, since the experimental uncertainties are large relative to the P_{LT} values, it is difficult to confirm the predictions. However the three new measurements, performed with a large statistics, may help to clear the picture. Investigating the GPs behavior will allow to gain a deeper understanding of the structure and the dynamics of the proton.

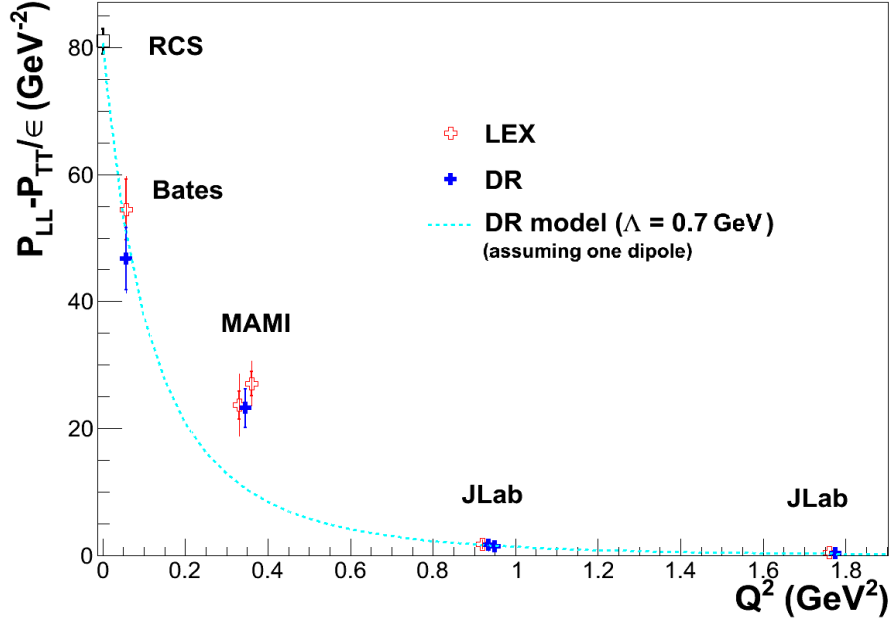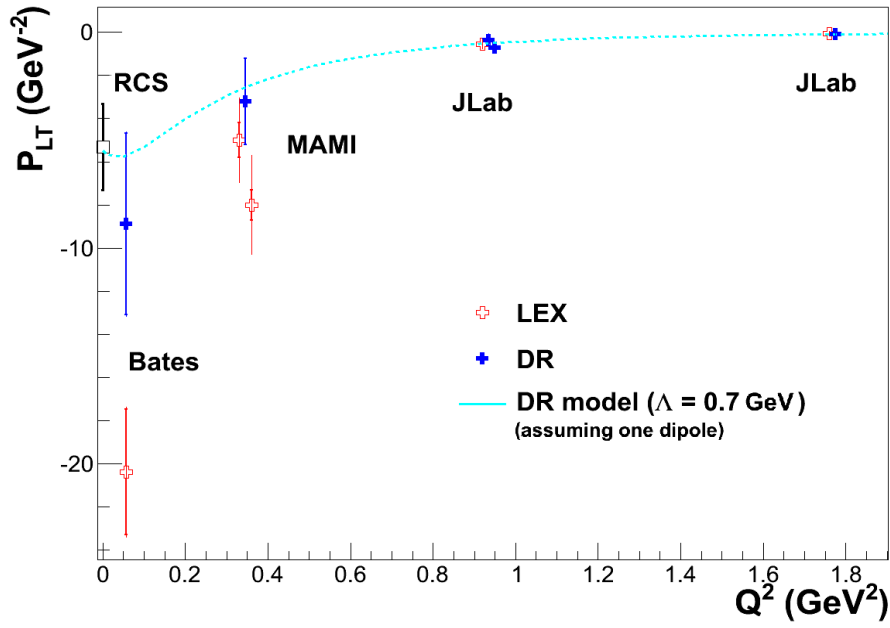Figure 2.8: World measurements of P_{LT} performed at JLab, Bates and MAMI by LEX analysis (empty red crosses) and DR analysis (full blue crosses) with statistical (inner) and total (outer) error bars. The DR model prediction assuming a dipole behavior for the asymptotic part of $\beta_M(Q^2)$ with $\Lambda_\alpha = 0.7$ GeV is also plotted (light blue dashed line). Some points are shifted in Q^2 for visibility.

Chapter 3

Experimental configuration

The following chapter is dedicated to the experimental configuration, from the presentation of the facility and the spectrometers to the presentation of our experimental choices.

Sections 3.1 and 3.2 are focused on the description of the Mainz Microton and the three-spectrometer facility of the A1 collaboration.

Section 3.3 explains which experimental configurations are more relevant to perform a GP extraction leading to our choice of kinematical settings.

3.1   MAMI

3.1.1   The Mainz facility

The Mainz Microtron (MAMI), located at the Institut für Kernphysik (KPH), is an accelerator for electron beams. The MAMI operation principles were developed by Prof. Dr. Helmut Herminghaus in cooperation with Dr. Karl-Heinz Kaiser [73]. The accelerator, operational since 1979, is regularly improved. The latest stage of development is MAMI-C, finalized in 2006, it provides an unpolarized (polarized) electron beam up to 100 μA (20 μA) and can reach an energy of 1.5 GeV.

The great advantage of MAMI is its capacity to provide a high intensity beam with a 100% duty cycle. Indeed the frequency of accelerating cavities is 2.45 GHz, this generates a beam with a neat temporal structure, i.e. each "bunch" of electrons is separated in time by only 0.4 ns. Thus the beam temporal structure is invisible for the detectors, for instance of A1, which have a time resolution of the same order of magnitude. The beam is then called a "continuous wave" beam. Typically in our experiment, with particles detected in coincidence by two spectrometers, the high duty cycle of MAMI is essential to increase the ratio of true coincidences over accidental ones.

Figure 3.1 is a layout of the facility. In each hall a collaboration is in charge of an experimental setup and follows a specific physics program. The A2 collaboration uses tagged real-photons to study processes such as: total photo-absorption, real Compton scattering and meson photo-production. The A4 collaboration was focused on parity violation in electron scattering. The physics motivation of the X1 collaboration is centered on the use of X-rays to determine material or biological properties.
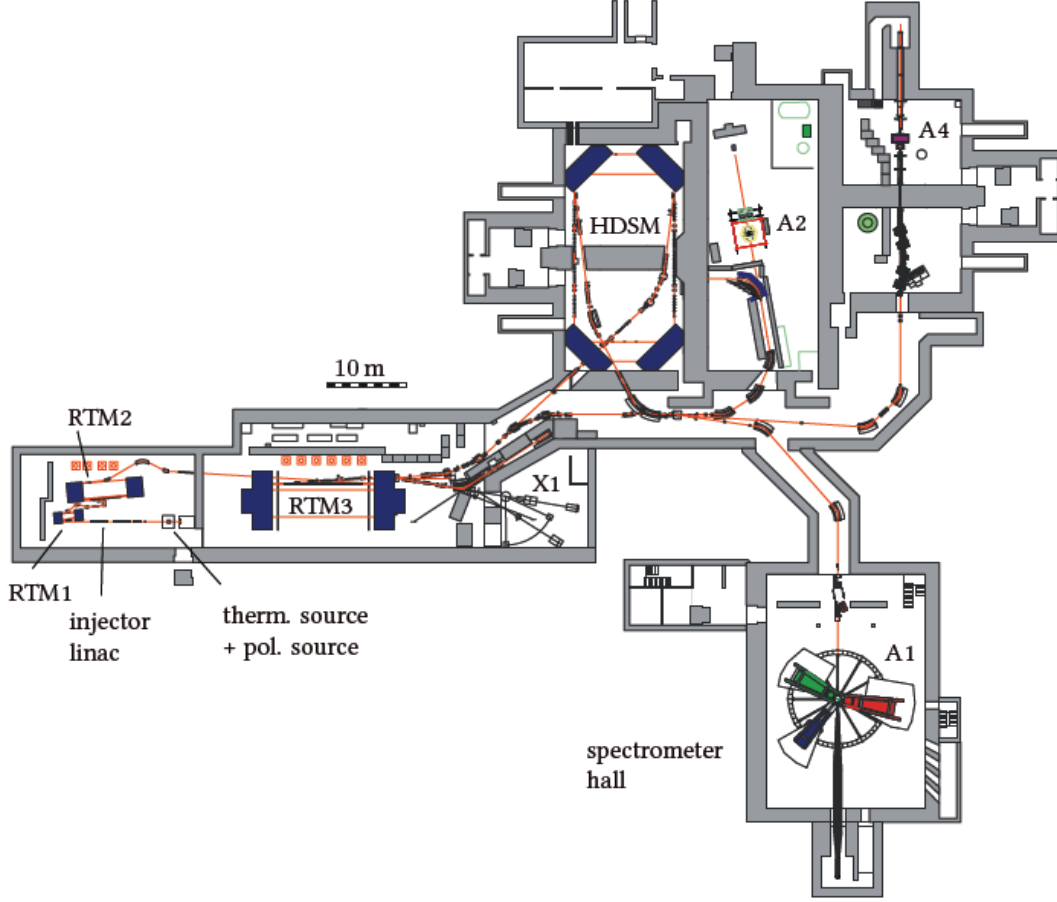
Figure 3.1: Schematic of MAMI.

3.1.2 Operating principles of MAMI

This section is a brief description of the MAMI design which is more detailed in [74]. Like in all microtrons the electron acceleration is done through linear sections. MAMI was designed to realize this acceleration while saving space. Figure 3.1 shows the electron path through the Mainz Microtron. After the choice of beam polarization (two different sources are available for polarized and unpolarized electrons) the electrons are sent through the injector. It is a linear accelerator (LINAC) that will increase the electron energy up to 3.5 MeV before entering the race-track microtrons (RTM).

A RTM, figure 3.2, is used to avoid the building of a too long accelerator. It contains a LINAC combined with two magnets that will bend the electron trajectory in order to drive it back to the linear section, where the electron will be accelerated again. So electrons will make several turns and at each turn their energy increases. The electron trajectory therefore increases in radius at each turn, giving to the RTM this particular design which inspired its name.

After 18 turns in RTM1 the electrons reach an energy of 14 MeV and are injected in the second and larger RTM. In RTM2 they again undergo the same acceleration process and after 51 turns their energy is about 180 MeV. At this
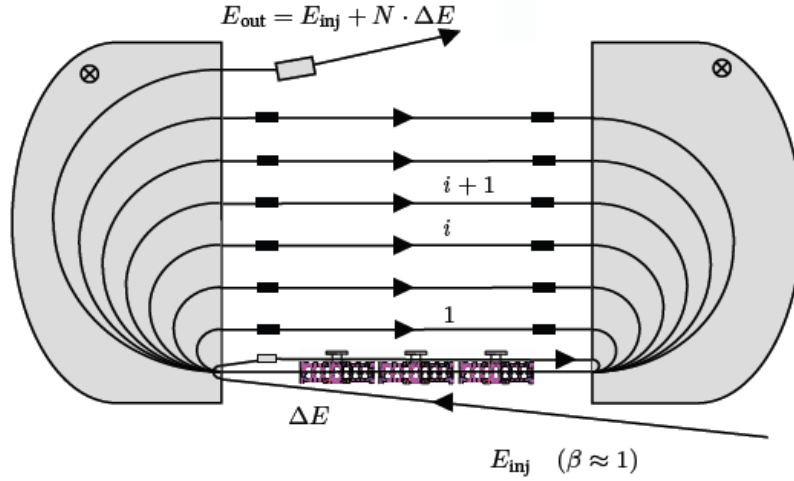
Figure 3.2: Schematic of a racetrack microtron (RTM) [74].

stage, called MAMI-A, the beam can be directed to experimental halls or sent to the third and even larger RTM. The electrons will do 90 turns in RTM3 to obtain an energy of 855.1 MeV. This step is called MAMI-B and here again one can drive the beam to experimental halls or choose to accelerate it again in the last stage.

At high electron energy like the one provided by MAMI-B the magnets must be large enough to completely deflect the electrons. But MAMI-B with its 5m wide magnets reached the mechanical limit of the RTM concept [73], and is the largest microtron in the world. Thus the last stage, MAMI-C, is made from another design: a harmonic double sided microtron (HDSM) accelerator presented in figure 3.3.
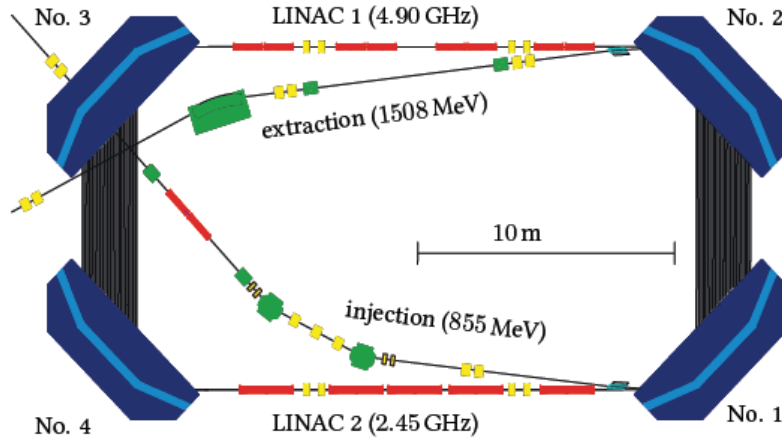
Figure 3.3: Schematic of a harmonic double-sided microtron (HDSM) [74].

A HDSM is composed of four 90°-bending magnets and two linear accelerators. The frequency of each LINAC is adjusted in order to prevent the beam from instabilities. After 43 turns in this last stage the electrons can reach an energy of 1508 MeV before getting directed to experimental halls.

3.2 A1 experimental hall

The physics program of the A1 collaboration is focused on electroproduction reactions on nuclear targets that probe hadron structure, such as: elastic scattering processes, electroproduction of mesons or photons, etc. The A1 experimental hall is easily identifiable in figure 3.1 by its three-spectrometer set-up [75]. These large and heavy spectrometers can be independently rotated around the central axis where the target is placed. Each spectrometer can be operated in a single, double or triple coincidence mode depending on the studied physical process. It is also possible to raise the spectrometerB in an out-of plane position and thus reach specific regions of the angular phase space.

3.2.1 The liquid hydrogen target

The vacuum scattering chamber, at the pivot point of the three spectrometers, holds several targets on a ladder. The ladder moves to select which target will be hit by the beam depending on the need of the experiment. For our experiment the carbon target was used for calibration, the aluminum oxide screen was needed for beam position monitoring and the liquid hydrogen target was the one necessary to realize the actual data taking.

In order to perform our GP extraction we need to control and measure the luminosity because we measure an absolute cross section. But, the luminosity of electron scattering experiments depends on target density (and indirectly its temperature). Furthermore the electrons will deposit energy in the target, warming it and changing its density. It is thus important to stabilize the target temperature by a cooling system. The liquid hydrogen target was built on the concept of closed-circuit loop. The circulation of liquid hydrogen is powered by a ventilator that ensures a constant flow in the target. Then the heat deposited by the electron beam dissipates during the passage of liquid hydrogen in the heat exchanger. The heat exchanger is cooled by a Philips cryo-generator. The whole scattering chamber and the Philips-Machine are represented in figure 3.4.

A second important point is to avoid the local density variation inside the cryo-target. A too localized and intense beam can even create local boiling. The "wobbler" mechanism, that displaces the beam transversely by a few millimeters along a determined pattern at a frequency of several kHz, will prevent the target from local boiling. The target dimensions are represented in figure 3.4, its length is 49.5 mm for a width of 11.5 mm. The cell walls are made of a HAVAR foil of $10 \mu m$ thickness.

The target average density and temperature are 0.069 $g.cm^{-3}$ and 22°K, its pressure is approximately 2 bar.

3.2.2 The high-resolution spectrometers

In our experiment the particles are detected in coincidence, the electron by spectrometer B and the proton by spectrometer A. The deflecting power of the spectrometers allows to reconstruct four particle properties at the target level in the considered spectrometer frame: θ_0 and ϕ_0 the particle vertical and horizontal angles, y_0 the coordinate of the particle track along the transverse horizontal axis,
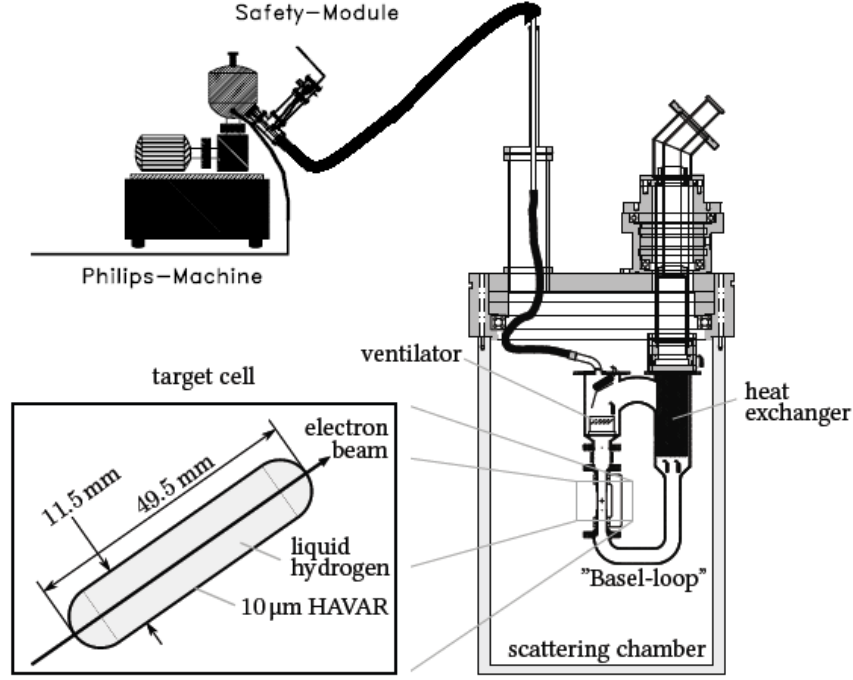
Figure 3.4: Schematic of the A1 vacuum scattering chamber and the liquid hydrogen target (bottom left).

and δ the particle relative momentum (relative to p_{ref} the reference momentum of the spectrometer). $(\delta, \theta_0, y_0, \phi_0)$ are the target coordinates in the spectrometer frame.

$(x, \theta, y, \phi)_{fp}$ are the equivalent of those coordinates in the spectrometer focal-plane frame. They are the coordinates that are actually measured by the detector package, and then the optical matrix is used to reconstruct the properties at the target level.

Thereafter the informations from the beam position and both spectrometers are gathered in order to reconstruct, in the lab frame, the vertex position and the missing mass.

The following sub-section summarizes the spectrometer reference frames and optics. In the next subsection the spectrometer A and B characteristics are detailed.

Spectrometer frames, Focal plane frame and optics

Two frames are important to define: the focal plane reference frame where the track reconstruction is performed; and the spectrometer frame which is at the target side. The spectrometer frame differs from the laboratory frame only by a rotation corresponding to the spectrometer position in the hall. The focal plane is a virtual plane located at the exit of the magnets, which is defined by an x axis perpendicular to the particle track and an upwards z-axis in the direction of the particle trajectory (the coordinates are represented in figure 3.6).

Figure 3.6 is a schematic representation of a particle track in spectrometer A. The dashed blue line is the reference track, i.e. the trajectory of a particle of
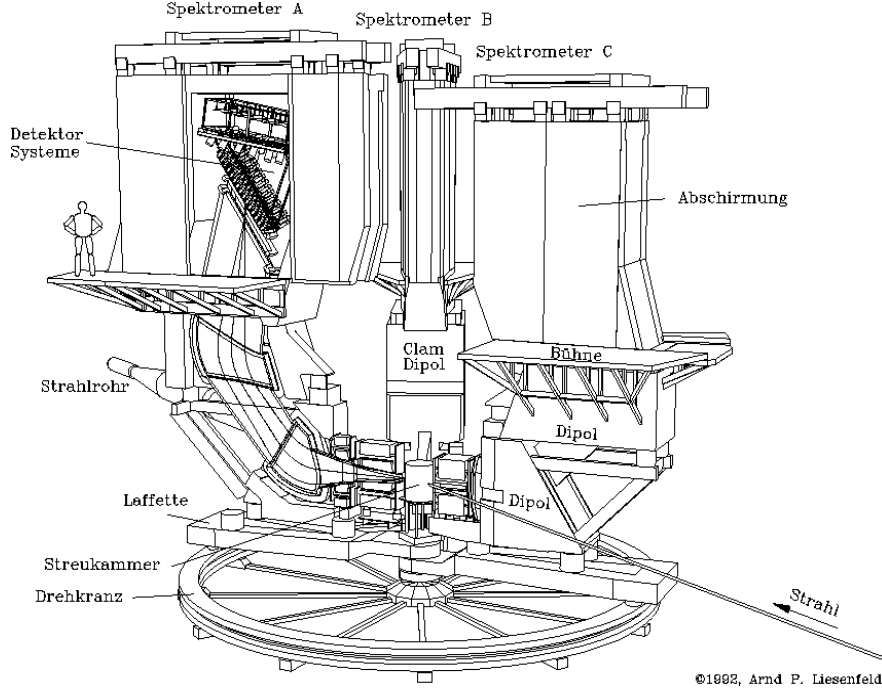
Figure 3.5: Schematic of the A1 three-spectrometers setup [75].

momentum p_{ref} that enters in the middle of the spectrometer acceptance ($\delta = 0, \theta_0 = 0°, y_0 = 0mm, \phi_0 = 0°$). The red line is the trajectory of an arbitrary particle. The four focal-plane coordinates $(x, \theta, y, \phi)_{fp}$ are linked to the target coordinates in the spectrometer frame $(\delta, \theta_0, y_0, \phi_0)$ by the spectrometer optics, with: x_{fp} and y_{fp} the coordinates of the intersection point between the focal plane and the particle; θ_{fp} and ϕ_{fp} its vertical and horizontal angles.

The spectrometer optics is a tensor of coefficients $(D_{ijkl}, T_{ijkl}, Y_{ijkl}, P_{ijkl})$ that correspond to a fifth-order polynomial expansion:

$$
\begin{aligned}
\delta &= \sum_{ijkl=0}^{5} D_{ijkl} \, (x_{fp} - x_{ref})^i \, (\theta_{fp} - \theta_{ref})^j \, (y_{fp} - y_{ref})^k \, (\phi_{fp} - \phi_{ref})^l, \\
\theta_0 &= \sum_{ijkl=0}^{5} T_{ijkl} \, (x_{fp} - x_{ref})^i \, (\theta_{fp} - \theta_{ref})^j \, (y_{fp} - y_{ref})^k \, (\phi_{fp} - \phi_{ref})^l, \\
y_0 &= \sum_{ijkl=0}^{5} Y_{ijkl} \, (x_{fp} - x_{ref})^i \, (\theta_{fp} - \theta_{ref})^j \, (y_{fp} - y_{ref})^k \, (\phi_{fp} - \phi_{ref})^l, \\
\phi_0 &= \sum_{ijkl=0}^{5} P_{ijkl} \, (x_{fp} - x_{ref})^i \, (\theta_{fp} - \theta_{ref})^j \, (y_{fp} - y_{ref})^k \, (\phi_{fp} - \phi_{ref})^l,
\end{aligned}
\tag{3.1}
$$

with $(x_{ref}, \theta_{ref}, y_{ref}, \phi_{ref})$ the focal-plane coordinates of the reference track. The coefficients have been determined by calibration measurements on specific targets with specific collimators [75].

Spectrometer A and B global characteristics

The spectrometers A and B share the same principle but differ by their size, capacity and conception. The spectrometer C, not detailed here, is a scaled-down

48
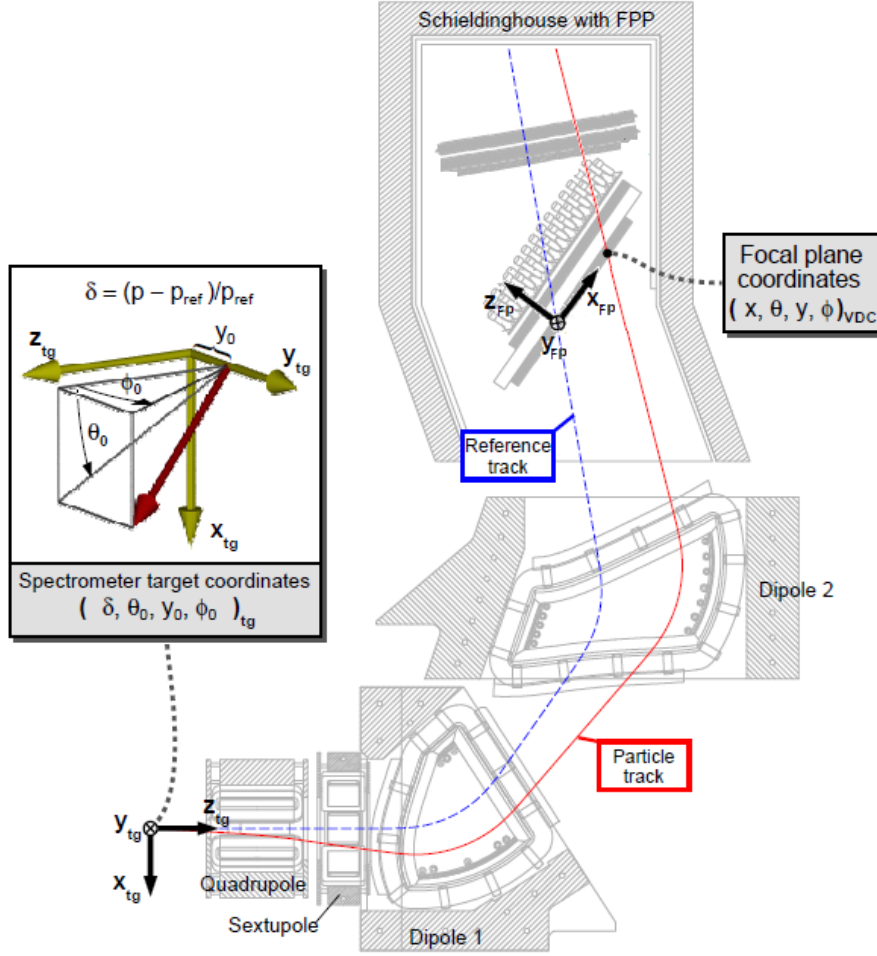
Figure 3.6: Schematic of a particle track in spectrometer A and representation of frame coordinates. $(\vec{x}, \vec{z})$ is the dispersive plane, $(\vec{y}, \vec{z})$ is the non-dispersive plane [76].

version of spectrometer A.

The spectrometer A holds four magnets, a quadrupole, a sextupole and two dipoles, in a so-called QSDD configuration. The two dipoles generate the particles dispersion while the quadrupole applies a focus to particles in the transverse direction. The sextupole performs corrections of aberrations in the dispersive plane. By consequence of this particular quadrupole-sextupole design, the spectrometer's angular acceptance is large but the reconstruction is parallel-to-point in the transverse direction, which means that a segment in target coordinates corresponds to a point in the focal-plane coordinates, and so the reconstruction of y_0^A suffers from a poor resolution. However this allows the precise first-order determination of ϕ_0^A through the measurement of y_{fp} [75].

In the dispersive direction the reconstruction is point-to-point, so the dispersive angle θ_0^A and the relative momentum δ^A are reconstructed with a good resolution.

The spectrometer B compensates the spectrometer A's poor resolution in transverse direction by a more simple design. Indeed it contains a single dipole with

a field gradient that adds quadrupole and sextupole contributions to ensure the focus. As a result, a point-to-point optics is obtained both in the dispersive and non-dispersive planes, and the momentum and position resolutions of spectrometer B are high. The counterpart is its small solid-angle and momentum acceptance. The other important characteristic of spectrometer B is its capacity to be tilted above the horizontal plane up to 10° in the so called out-of-plane position. This will allows us to measure particles from the photon electroproduction process when $\varphi_{cm} \neq 0$ and access specific and relevant regions of the phase space.

The main properties of the two spectrometers are summarized in table 3.2.2.

	units	A	B
Configuration		QSDD	D
dispersive plane		point-to-point	point-to-point
non dispersive plane		parallel-to-point	point-to-point
Maximum momentum	[MeV/c]	735	870
Reference momentum	[MeV/c]	630	810
Central momentum	[MeV/c]	665	810
Solid angle	[msr]	28	5.6
Scattering Angle			
minimum angle		18°	7°
maximum angle		160°	62°
Momentum acceptance		20%	15%
Angular acceptance			
dispersive	[mrad]	70	70
non-dispersive	[mrad]	100	20
Long target acceptance	[mm]	50	50
angle of focal plane		45°	47°
length of focal plane	[m]	1.80	1.80
length of central trajectory	[m]	10.75	12.03
Dispersion (central)	[cm/%]	5.77	8.22
Magnification (central)		0.53	0.85
Dispersion/Magnification	[cm/%]	10.83	9.64
momentum resolution		10^{-4}	10^{-4}
angular resolution at target	[mrad]	<3	<3
position resolution at target	[mm]	3-5	1

Table 3.2.2: Parameters of the spectrometers A and B. Values are taken from [77].

3.2.3 Focal-plane detectors

For each spectrometer the standard detector package is composed of two pairs of vertical drift chambers (VDC), two scintillator planes and a Cerenkov detector (the configuration can be changed to use specific detectors like a polarimeter). In this section, based on [75], the detectors are introduced in an order that follows the particle trajectory in the spectrometer.

Vertical drift chambers

The vertical drift chambers (VDC) are the first stage of detection. They aim to determine the focal-plane coordinates $(x, \theta, y, \phi)_{fp}$.

Their operating principle is represented in figure 3.7. A VDC has a planar structure with a plane of wires which is surrounded by two planes of high voltage cathodes. Two kinds of wires compose the wire plane: the wider wires which are called potential wires; and the thinner signal wires. The chamber is filled with a mixture of equal parts of argon and isobutane, plus 1.5% of ethanol.

When a charged particle passes through the VDC it ionizes the gases generating secondary electrons. The voltage difference between cathodes and wires will make the electrons drift. Then when they approach a signal wire, the secondary electrons at their turn start to ionize the gases and generate an electron avalanche. The potential wires serve to optimize the field lines repartition. The start of the avalanche is detected in the signal wires. The signal of wires close to the particle trajectory starts earlier than the signal from more distant wires. Figure 3.7 is a schematic representation of the drift time as measured by a time-to-digital converter (TDC), the common stop being given by the scintillators.
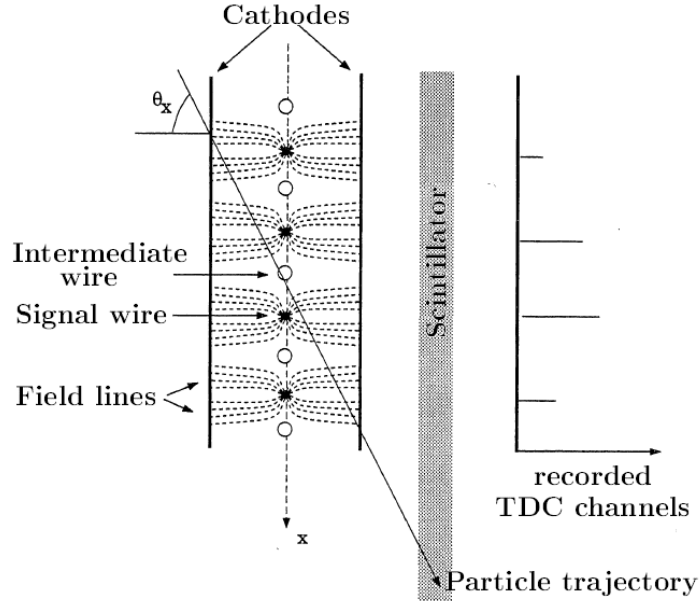
Figure 3.7: Schematic of the electric field lines in a VDC when a particle crosses the detectors and representation of the corresponding recorded signal in TDC channels, from [78]. The longer signals correspond to closer wires.

Each spectrometer contains two VDCs (1 and 2), as it appears in figure 3.6 the VDCs plane is tilted by 45° with respect to the reference trajectory. In this way the number of wires hit by a particle is increased.

To measure the four coordinates in the focal plane each VDC holds two planes of wires. The X_1 and X_2 planes, composed of wires parallel to $(\vec{y_{fp}})$, determine the particle momentum and vertical angle. The S_1 and S_2 planes, with wires rotated from 40° with respect to the X plane, measure the two other coordinates.

Thanks to this design the overall tracking efficiency is better than 99.9% (99% for a single plane) and the following resolutions are achieved [77] :

$$\delta x_{fp} = 100 \ \mu m$$
$$\delta y_{fp} = 200 \ \mu m$$
$$\delta \theta_{fp} = 0.3 \ mrad$$
$$\delta \phi_{fp} = 1 \ mrad.$$

Scintillators

The next detectors encountered by a particle are two scintillator planes; one which is 3 mm thick, called "dE" for energy loss, and the second which is 10 mm thick and called "ToF" (for Time of Flight). Each plane of spectrometer A (B) has 15 (14) paddles linked via a light-guide to two photomultipliers (PMT). The PMT signals are sent to time-to-digital converters (TDCs) and analog-to-digital converters (ADCs) providing informations that have a threefold use:

Firstly, since their response signals are fast they serve as trigger for the data acquisition.

Secondly, they are used for timing measurements. As mentioned before, scintillators give the stop signal for VDC channels but they also allow a reconstruction of the coincidence time. When a particle hits the scintillator in, for instance, spectrometer A, it opens a $\approx 80 \ ns$ window. Then the acquisition waits for a second signal from the other spectrometer scintillators. The measured time between these two TDC signals (after fine corrections) is presented in figure 3.8 (without any selection of events). We distinguish two kinds of coincidences: the accidental coincidences which are randomly distributed in time; and the true coincidences which are in a peak centered on 0. Figure 3.8 illustrates the very good time resolution ($\sigma \approx 0.40 \ ns$) and the advantage of a high duty cycle as MAMI (the ratio of true coincidences over random ones is ≈ 15).

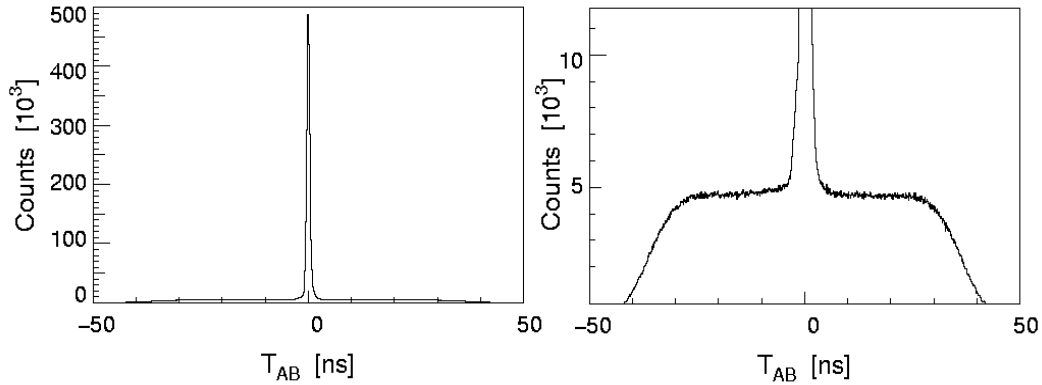Figure 3.8: Coincidence time measurements by scintillators (after software corrections), before (left) and after (right) zooming the y axis. The accidental coincidences appear as a flat distribution, the true coincidences are distributed in a narrow peak.

The third use of scintillators is for particle identification. Indeed the PMT signal is also integrated by an ADC and this information is proportional to the energy

lost by the particle in the scintillator paddle. A proton of a given momentum will deliver more energy than a pion of the same momentum in our low-energy regime.

Cherenkov detector

The last sub-detector is a threshold gas Cerenkov counter, which is used for particle identification between pions and electrons. Pions of a given momentum cross the detector at a lower speed than electrons of the same momentum, the Cerenkov detector is adjusted in a way that only the electrons generate Cerenkov light (i.e. 10 MeV electrons are faster than light in the medium which has a refraction index $n = 1.0014$). The Cerenkov process occurs in a decafluorobutane (C_4F_{10}) gas at atmospheric pressure [77]. The emitted light is reflected by mirrors to photomultipliers; there are twelve mirrors in spectrometer A and five in spectrometer B.

3.2.4   Trigger and data acquisition: the A1 software

Trigger and data acquisition

The trigger is independent in each spectrometer and the trigger conditions can be set differently in each spectrometer. The minimal trigger condition is a single signal in only one scintillator PMT but, to minimize the background, a coincidence between the left and right PMTs of the scintillator paddle is required. Then one can ask for the particle to be detected in one of the two planes (dE or ToF) or in both of them.

After being analyzed by the programmable logic unit (PLU) the signals are sent to a fast programmable gate array (FPGA) that gather signals from the three spectrometers. Then if the FPGA accepts an event a signal is sent to the front-end electronics of spectrometers to start the read-out process of digitized detector signals. Finally the data are sent to a workstation where the acquisition program "Aqua++" combines them in the event builder. The trigger process is further detailed in [75].

After the detection of a particle the recorded informations in the runfile are:
- the drift time of each activated wire
- the TDC and ADC information in each scintillator
- the PMT signal of Cerenkov detectors
- the target conditions
- the wobbler information
- the content of scalers for luminosity calculation.
Those informations are sufficient to reconstruct the particle momentum and trajectory, and also the vertex position in the target.

The A1 software stack

The A1 collaboration uses an in-house built software package [79] that allows to read out the detector electronics, do the data acquisition and perform both online and offline analysis. The four softwares involved are: Mezzo for the slow control,

Aqua++ for the data acquisition, Lumi++ for luminosity calculation, and Cola++ for the analyses.

Mezzo is the slow control software, i.e. it records numerous parameters describing the status of the apparatus: spectrometers, beam and target. Its readout is sent directly to the central process via fast Ethernet at a typical frequency of 1 Hz, and thus can be seen by the user to check the experiment conditions online.

Aqua++ merges all data from spectrometers into events and saves them on a disk. The duration of data collection is limited, a single data-taking is a so-called run, and the choice of run's length is left to the user.

Coincidence events are recorded, but the single-arm events are also kept for the use of calibration. For this purpose a counter module is a part of the experimental trigger, it allows the prescale of single-arm events from each spectrometer separately.
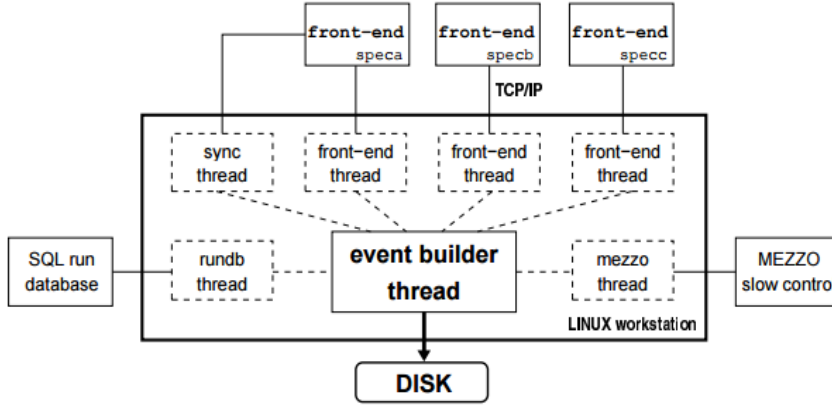
Figure 3.9: Schematic view of the Aqua++ event builder threads, from [79].

Figure 3.9 is a schematic view of the Aqua++ event builder threads [79], it illustrates how the event builder merges informations from each spectrometer's front-end, from a user interface (SQL run database) and from the Mezzo slow control. In this way, the slow control data are also available for offline analysis.

Lumi++ is the software used for online and offline luminosity calculations. The integrated luminosity of a run is the product of incident electrons number during the run, by the number of target nuclei per unit area:

$$\mathcal{L} = \frac{Q_{tot}}{e} \cdot \frac{\rho \bar{x}_{tg} \mathcal{N}_A}{A}, \tag{3.2}$$

with $e = 1.6 \cdot 10^{-19} \ C$ the elementary charge, $\mathcal{N}_A = 6.022 \cdot 10^{23} \ mol^{-1}$ the Avogadro constant, $A = 1.008 \ g \cdot mol^{-1}$ the hydrogen molar mass and ρ the target density. $\bar{x}_{tg}$ is the averaged target length[1]. The total charge Q_{tot} is obtained by the

---

[1]The particular shape of the target with its round endcaps is not considered by Lumi++.

54

integration of the beam current (measured by a Foerster probe) in time intervals (measured by scalers). All these informations are gathered over time and used by Lumi++. Furthermore the software also uses informations from other scalers which measure the dead time.

Cola++ is the data analysis software that is used both in online and offline analyses. It reads run files to build histograms readable by the user and also provides tools for: the manipulation of four-vectors, the customization of data cuts, and the design of events weighting. To function properly Cola++ needs three input files:
- The run.db file (for run database file) contains parameters, ordered in time, that describe the experimental conditions and have to be calibrated, see chapter 4.
- The .col file contains the list of histograms to be produced by Cola++ and the analysis conditions: the events selections, the definition of variables elaborated from raw variables (from run files), the events weight, etc.
- The .tma files (for transfer matrix files) detail the optics parameters defined in section 3.2.2.

3.3 Choice of kinematical settings

The VCS phase space is defined by the five variables $(q_{cm}, q'_{cm}, \epsilon, \theta_{cm}, \varphi_{cm})$. In the lab frame particles from the $ep \rightarrow ep\gamma$ process are emitted in a large range of directions, but with our spectrometers acceptance we only have access to a limited part of the VCS phase space. Moreover all the phase-space regions are not of equal interest. For instance in the Bethe-Heitler peaks the electron bremsstrahlung is too dominant to perform a GP extraction. So we need to carefully decide where the extraction will be done and so where the A1 spectrometers are positioned.

3.3.1 The leptonic-side variables

Among the five important variables, three are fixed by the leptonic part of VCS $(q_{cm}, q'_{cm}, \epsilon)$. These variables are fixed by the electron lab-frame variables: (k, k', θ_e), and so they are fixed by the electron spectrometer and the beam. Their value is deduced from three constraints.

First we want to perform our measurement around $Q^2 = 0.2\ GeV^2$, this fixes q_{cm}.

Secondly, since in the LEX equation 1.38 the GP effect depends on q'_{cm}, we need to increase q'_{cm} to magnify the effect. But in order to perform our LEX analysis q'_{cm} has to remain under the pion production threshold.

The third and last constraint is that we want to have ϵ as high as possible, i.e. close to 1. Indeed in equation 1.38 ϵ is in factor of the structure functions through the v_{LL} and v_{LT} coefficients.

Another criterion could be considered: it is essential to have a large range in q'_{cm} to increase the lever arm in our LEX analysis. Fortunately this is ensured by the large momentum acceptance of the spectrometers.

3.3.2   The center-of-mass angles of the Compton Scattering process

We have more freedom in our choice of center-of-mass angles θ_{cm} and φ_{cm} (cf. figure 1.8) and it seems a priori that any value out of the Bethe-Heitler peaks would be relevant for a GP extraction. However it appears that it is not that simple.

The explored region in θ_{cm} and φ_{cm} depends on the spectrometers acceptance. It also depends on Q^2, the higher Q^2 is the narrower will be the cone drawn by the outgoing proton and the larger will be the phase space probed in our experiment. But at $Q^2 = 0.2\ GeV^2$ it is impossible to explore the whole $(\theta_{cm},\varphi_{cm})$ space with the acceptance of our spectrometers with only one setting. So we have to decide which settings are relevant and three criteria motivated our choice.

The first criterion is the importance of the GP term compared to the cross section σ_{BH+B}. At $q'_{cm} = 112.5\ MeV/c$, figure 3.10 shows the relative theoretical GP effect according to the LET:

$$relative\ GP\ effect = \frac{\Phi q'_{cm}[v_{LL}(P_{LL}(q_{cm}) - \frac{P_{TT}(q_{cm})}{\epsilon}) + v_{LT}P_{LT}(q_{cm})]}{\sigma^{BH+B}}. \quad (3.3)$$

Two relevant regions of the $(\theta_{cm},\varphi_{cm})$-plane appear to have an important GP effect:

- The first region for $\varphi_{cm} \approx 0$ and $cos(\theta_{cm}) \approx -1$ with a GP effect of approximately $+20\%$.

- The second region when $\varphi_{cm} \approx \pm100°$and $cos(\theta_{cm}) \approx 0$ with a GP effect of approximately -10%.

We will now consider these two regions and we will check if they also satisfy the two remaining criteria. If so, our spectrometers will be fixed in order that their acceptance roughly corresponds to the considered region.

The second criterion is the weight of each structure function independently in the GP effect of equation 3.3. We wanted to realize two settings, one which will be more sensitive to the electric GP and another that will be more sensitive to the magnetic GP. This selective sensitivity is determined by the values of the coefficients v_{LL} and v_{LT}, according to equation 1.38. Figures 3.11 and 3.12 show the theoretical behavior of the coefficients v_{LL} and v_{LT} in the $(cos(\theta_{cm}),\varphi_{cm})$-plane at fixed $q_{cm} = 458\ MeV/c$ and $\epsilon = 0.85$. The previously selected region for $\varphi_{cm} \approx 0$ and $cos(\theta_{cm}) \approx -1$ is still interesting since it corresponds to a domain where $v_{LL} \approx 0$. The second selected region where $\varphi_{cm} \approx \pm100°$and $cos(\theta_{cm}) \approx 0$ contains points where $v_{LT} = 0$ and therefore should be highly sensitive to the $P_{LL} - P_{TT}/\epsilon$ structure function. So the selected regions also satisfy this second criterion.

The third and last criterion is to have a large range in v_{LL} and v_{LT} coefficients. Indeed to realize the final structure function fit one has to dispose of a large lever arm in the coefficients in order to increase the global sensitivity of our fit. Since the two selected regions stand for respectively opposite value of the coefficients, as it appears on figures 3.11 and 3.12, they will offer the necessary lever arm.
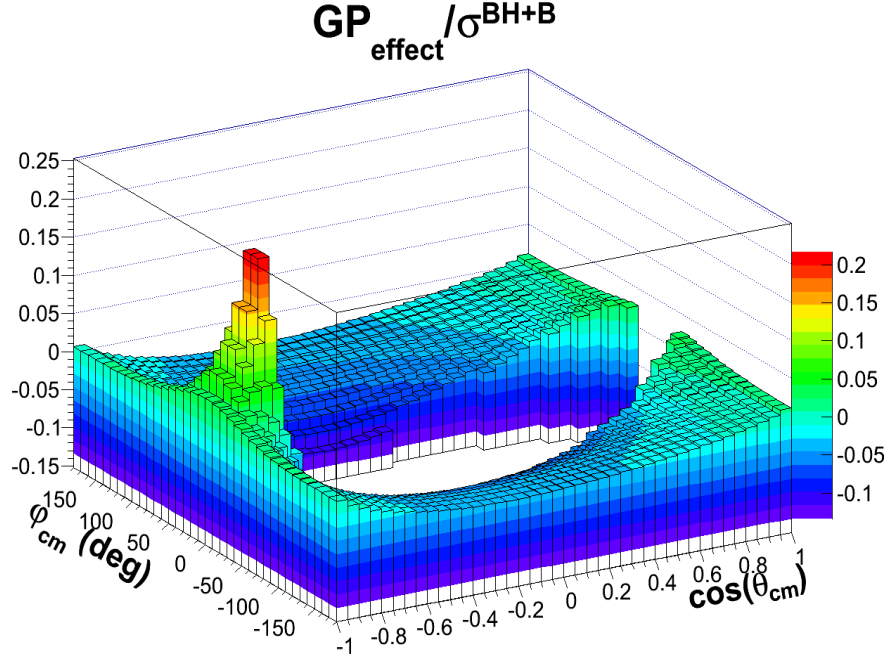
Figure 3.10: Theoretical relative GP effect according to the LET and equation 3.3 for $P_{LL} - P_{TT}/\epsilon = 20 \ GeV^{-2}$ and $P_{LT} = -4 \ GeV^{-2}$ at $q'_{cm} = 112.5 \ MeV/c$. The blank region at the center of the plot is removed for clarity reasons and corresponds to the Bethe-Heitler peaks.
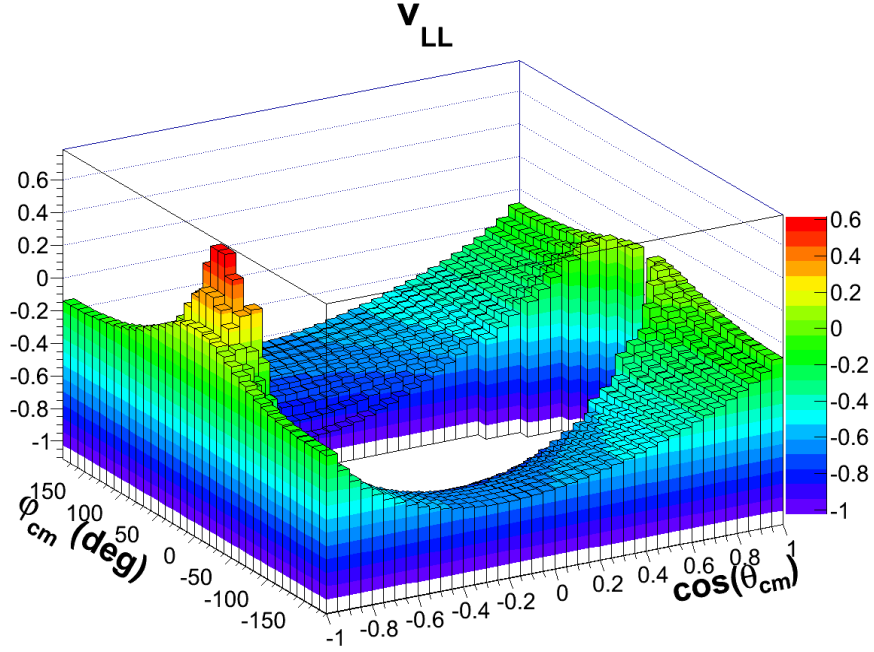

Figure 3.11: Theoretical behavior of v_{LL} in the $(\cos(\theta_{cm}),\varphi_{cm})$-plane at fixed $q_{cm} = 458 \ MeV/c$ and $\epsilon = 0.85$.
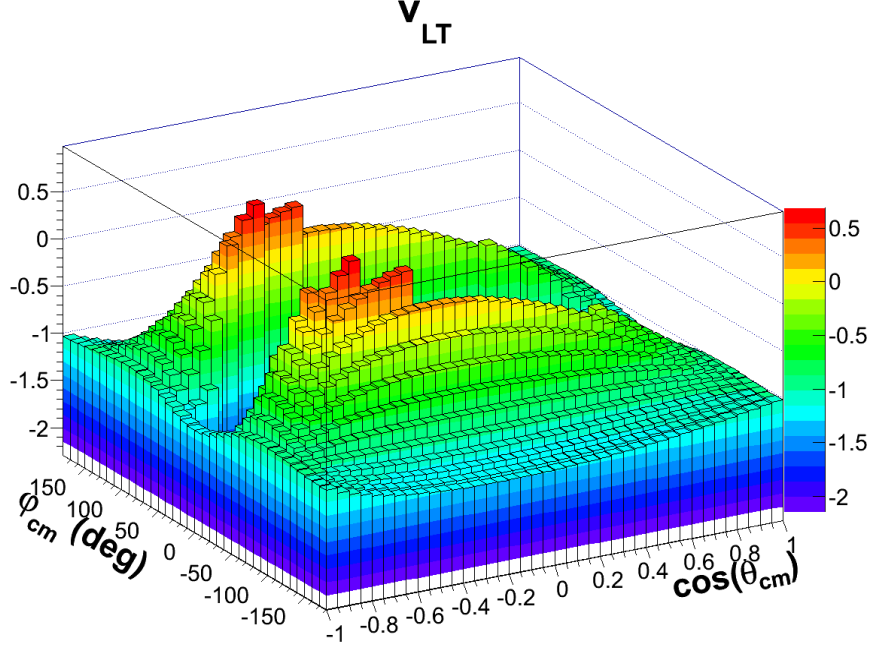
Figure 3.12: Theoretical behavior of v_{LT} in the $(cos(\theta_{cm}),\varphi_{cm})$-plane at fixed $q_{cm} = 458\ MeV/c$ and $\epsilon = 0.85$.

3.3.3 A last criterion: the LEX validity

From the BATES experiment [66][67] we know that ignoring the higher-order terms in the LEX analysis is not always safe. Indeed the higher-order terms ($O(q'^2_{cm})$ in equation 1.38) depend on the $(\theta_{cm},\varphi_{cm})$ angles and become in some cases too strong to be neglected. So we wanted to identify the regions where higher-order effects are small enough in order to realize a LEX extraction as meaningful as possible.

To do that we build a theoretically-based criterion which provides an evaluation of the higher-order effect. For a coherent and fixed choice of structure functions we calculate the theoretical photon electroproduction cross-section from LEX (σ^{LEX}), i.e. truncated at first order. We also calculate the theoretical cross section predicted by the DR model (σ^{DR}) where we keep the exact same choice of structure functions.

Even if the higher-order terms are not specifically expressed in the DR cross section they are included as a whole in the calculation. Then the comparison of the DR cross section to the LEX one will provide an estimation of the higher-order terms. So $\mathcal{O}^{DR}(q'^2_{cm})$ is the criterion representing the relative importance of higher-order terms in the LEX cross section, according to the DR model. It is written as:

$$\mathcal{O}^{DR}(q'^2_{cm}) = \frac{|\sigma^{LEX} - \sigma^{DR}| * 100}{\sigma^{BH+B}}. \qquad (3.4)$$

Figure 3.13 shows the value of this theoretical criterion in the $(cos(\theta_{cm}),\varphi_{cm})$-

plane and also a two-dimensional representation where only the bins where $\mathcal{O}^{DR}(q'_{cm}{}^2) < 2\%$ remain (in blue). This second representation helps to identify the considered acceptance areas which are represented by red perimeters, the dashed black area stands for the BH peaks. Later in section 5.5.2 we will see how applying a cut on $\mathcal{O}^{DR}(q'_{cm}{}^2)$ impacts our analysis.

The first selected region (for $\varphi_{cm} \approx 0$ and $cos(\theta_{cm}) \approx -1$) appears to be of interest since it contains kinematical points where the higher-order effect is negligible according to the DR model. But the region also contains kinematical points where the higher orders seem to be important and where a LEX analysis may be adventurous. Later in section 5.5.2 we will show how we can get rid of these kinematical points. The higher orders appear to be smoother in the second selected region ($\varphi_{cm} \approx \pm100°$ and $cos(\theta_{cm}) \approx 0$).
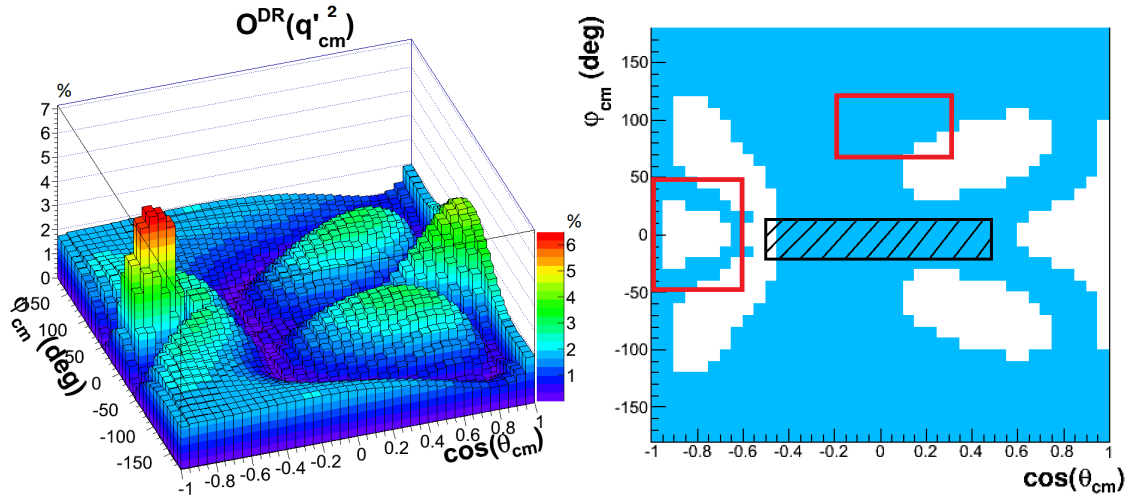
Figure 3.13: (Left) behavior of $\mathcal{O}^{DR}(q'_{cm}{}^2)$ in the $(cos(\theta_{cm}), \varphi_{cm})$-plane at $q'_{cm} = 87.5\ MeV/c$ and (right) two-dimensional representation of the angular region where $\mathcal{O}^{DR}(q'_{cm}{}^2) < 2\%$ (blue), the red squares correspond to the two areas of interest to perform the GP extraction.

To conclude, all the presented criteria are fulfilled by the regions indicated in red, which were at the basis of the definition of our spectrometer settings. The contour drawn by the spectrometers acceptance is actually larger and varies with respect to q'_{cm}.

3.3.4 The $Q^2 = 0.2\ GeV^2$ settings

Two main settings (corresponding to different spectrometers position) were designed in order to probe the regions of interest. A so-called in-plane setting containing the ($\varphi_{cm} \approx 0$ and $cos(\theta_{cm}) \approx -1$) region which will be more sensitive to P_{LT} and $\beta_M(Q^2)$, and a so-called out-of-plane setting which used the out-of-plane capability of spectrometer B to probe the second region more sensitive to $P_{LL} - P_{TT}/\epsilon$ and $\alpha_E(Q^2)$. These two settings are centered on values of q'_{cm} as high as possible but still below the pion threshold.

An important step of the analysis is the renormalization procedure which will be presented in section 5.4. To perform it we also need data where the GP effect is very small. This is realized with supplementary settings centered at low values of q'_{cm} ($\approx 25 - 50$ MeV/c). They are called the low-q'_{cm} settings.

The data taking at $Q^2 = 0.2 \ GeV^2$ took place in 2011 but a problem was encountered that required us to redo the out-of-plane setting in 2015. We then decided to add another setting in a third region of interest, the "forward out-of-plane setting". Table 3.3.4 gathers the spectrometers settings analyzed at $Q^2 = 0.2 GeV^2$.

setting name	E_{beam} (MeV)	$\boldsymbol{P_B}$ MeV/c	$\boldsymbol{\theta_B}$ (^{o})	$\boldsymbol{OOP_B}$ (^{o})	$\boldsymbol{P_A}$ MeV/c	$\boldsymbol{\theta_A}$ (^{o})
$Q^2 = 0.2$ GeV^2						
LOW	904.9	723	32.5	0.0	462	52.2
LOW-bis	904.9	715	32.5	0.0	442	52.2
INP	1002.4	766	30.4	0.0	580	51.5
OOP	1002.4	766	29.2	8.5	486	51.0
OOP-forward	1002.4	770	29.2	8.5	411	42.5

Table 3.3.4: The analyzed kinematical settings for spectrometer A and B. (P_B, P_A) are the central momenta and (θ_B, θ_A) are the spectrometer angles w.r.t. the beam. The scattered electron and proton are respectively detected in spectrometer B and A.

Chapter 4

Experimental Analysis

In this chapter we present the first-level analysis work. The detectors need to be calibrated, the experimental data have to be checked and the VCS events must be selected.

Sections 4.1 and 4.2 contain the description of detectors calibration. The first section is a brief introduction of standard A1 calibrations while the second section describes with more detail the unusual issues we encountered. Section 4.3 presents the data selections and binning. Sections 4.4 and 4.6 gather the control figures used to ensure our analysis correctness, while section 4.5 is devoted to the simulation of the experiment.

4.1 Standard raw data calibration

The calibration of focal-plane detectors is essential for using clean data-selection and for extracting the GPs with minimized systematic errors. The procedures we followed are summarized here and described with more details in [71].

The calibrations presented in this section are made thanks to the raw informations from detectors but also some specific variables defined in Cola++ (missing mass, errors estimated on track reconstruction, etc...). The settings are calibrated independently by following the same procedure. For some calibrations a data selection is required.

4.1.1 The photon missing-mass squared

The missing-mass squared, M_X^2 is a relativistic invariant, defined as the squared mass of the undetected particles (the real photon in our experiment) by:

$$M_X^2 = E_X^2 - \vec{p_x}^2,$$ (4.1)

with $E_X = (E_p + E_e) - (E_{p'} + E_{e'})$ the missing energy and $\vec{p_x} = (\vec{k} + \vec{p}) - (\vec{k'} + \vec{p'})$ the missing momentum, both being defined thanks to conservation laws.

Beside the reaction identification, the missing-mass squared is a powerful tool to calibrate our detectors. Indeed M_X^2 is deduced from the four-momentum vectors

reconstructed by both spectrometers A and B. A wrong calibration will then impact directly its resolution, so by minimizing the resolution of M_X^2 one can identify the optimal offset values.

For the $ep \rightarrow ep\gamma$ reaction, the missing-mass squared of the real photon is centered on 0 MeV^2 with a radiative tail at positive M_X^2. The next channel is the pion production $ep \rightarrow ep\pi^0$ which corresponds to a missing-mass squared $M_X^2 = 18225\ MeV^2$. This reaction constitutes a second source of true coincidences that is unwanted in our VCS analysis. Therefore, the missing-mass squared is used as a selection tool. Figure 4.1 shows an example of the missing-mass squared as reconstructed by Cola++.
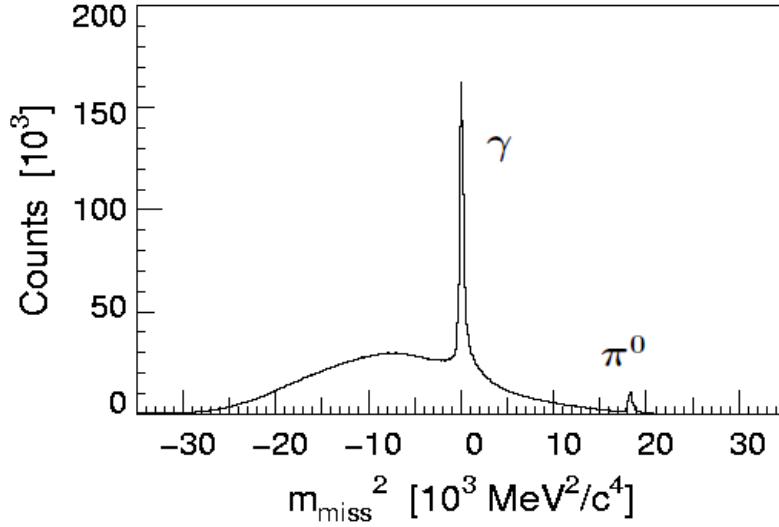
Figure 4.1: The missing-mass squared as reconstructed by Cola++ for all coincidences of the setting INP. The left peak corresponds to $ep \rightarrow ep\gamma$ events, the small peak at the right to the $ep \rightarrow ep\pi^0$ reaction.

The total distribution of figure 4.1 is a convolution of several ones: the peaks from γ and π^0 events, but also broader distributions that we want to remove from our analysis. One is from random coincidences (left of figure 4.2) and the other is generated by the target walls (right of figure 4.2).

The random coincidences distribution also presents a tiny peak of $ep \rightarrow ep\gamma$ events which is a consequence of the spectrometers time resolution. The target walls distribution is comprised of random coincidences but also of true coincidences from $ep \rightarrow ep\gamma$ and $ep \rightarrow ep\pi^0$ reactions on a proton in a nucleus. These events occur on protons which are not at rest, and so, they are not to analyse. This spectrum shows also a small peak on hydrogen, due to an imperfect cut on the vertex position.

The goal of the calibration presented in the following is to have a good control of the data selections that keep the events from the $ep \rightarrow ep\gamma$ reaction.

Figure 4.2: Setting INP: reconstructed M_X^2 for random coincidences (left) and events from the target walls (right).

4.1.2 Calibration of VDCs

Disabling wires

It happens that VDC wires are dead or inefficient. Such wires are easy to identify since their counting rate will be unexpectedly smaller than the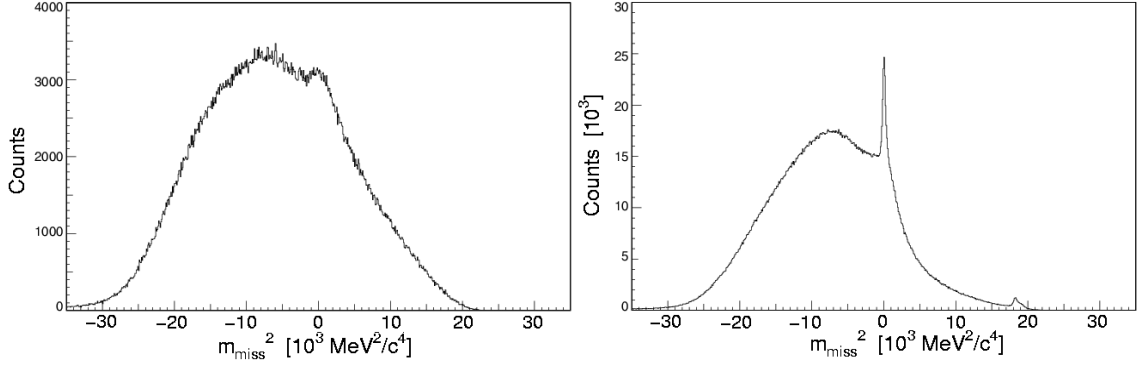 one of neighbouring wires. In the same way the so-called "hot wires" with a too high counting rate have to be disabled since they trigger even when their is no particle passing them. The procedure is described in [71].

TDC offsets of drift time

The drift time in VDCs is used for track reconstruction. For each of the four VDC planes the measured drift time will depend on an offset that has to be calibrated. In order to realize the calibration of the four VDCs we use the track-reconstruction errors of the four focal-plane coordinates provided by Cola++.

So for each VDC we test a range of offset values, then we calculate, for a run, the mean value of the error on reconstructed tracks. Figure 4.3 shows how the mean value of the error on the spectrometer B $s2$-plane varies with the offset (in units of TDC channel). In this way the offset that minimizes the reconstruction errors is identified.

Drift velocity

The drift velocity is also a parameter to calibrate; it may vary with time, for instance when an isobutane bottle change occurs. The calibration is done thanks to the error on track reconstruction in the same way as for TDC offsets.

Once the calibration is done one has to ensure that the optimal value is stable over time, i.e. for each data run of a setting. If it is not, a new calibration is done and applied to the problematic runs.

Drift time criterion

The timing differences between signals in neighbouring wires can be used to differentiate between "good events" from the ionization of the measured particle and the
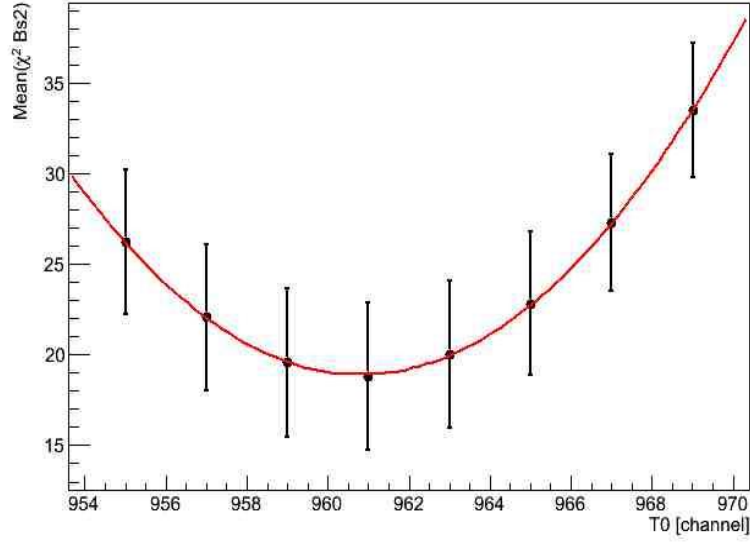
Figure 4.3: Mean value of the error on reconstruction per track with respect to a range of TDC offsets, for the spectrometer B $S2$ layer; the variable is labeled as "B.s2.chi_sqr" in Cola++. The error bars come from the determination of the mean by ROOT.

so-called δ-electrons from secondary ionizations. It also prevents from hot-wires signal. Figure 4.4 is a schematic representation of those events in a VDC plane.

One has to set three parameters in order to filter out wrong events by this criterion. The procedure is described in [71].
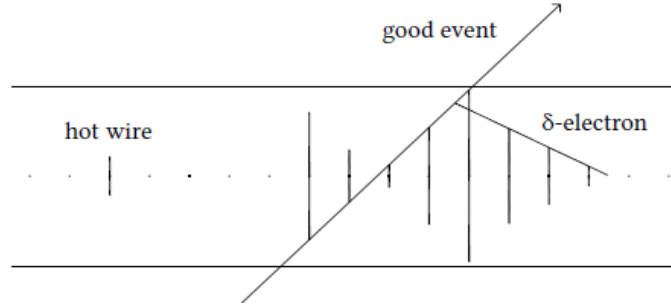
Figure 4.4: A hot wire, a good event and a δ-electron event in a schematic representation of a VDC plane from [71]. The vertical lines represent the time it took for the signal to arise after the passage of a particle through the VDC.

Tracking quality and efficiency

The quality of the VDC tracking can be checked over time by plotting the evolution of the resolution on the four focal plane coordinates in a complete setting (variables labeled as "$\Delta x, \Delta y, \Delta \theta, \Delta \phi$" in Cola++). This should remain stable and is a good indication if the calibration is incomplete. This was checked for our five settings and all the instabilities were corrected.

64

The efficiency per wire is at least superior to 90%. Such an efficiency is enough to get close to a 100% efficiency for the tracking. Therefore we do not apply any correction for tracking inefficiency.

4.1.3 Calibration of Cerenkov detectors

In our experiment we use the information from the Cerenkov detector in spectrometer B which is dedicated to the separation of electrons from pions. Nevertheless we did not make use of it since the other analysis cuts were sufficient to supress the pions (this is presented in section 4.3). So the only calibration we did consists in shifting the PMT pedestal values to zero in order to align them.

4.1.4 Scintillators

Timing calibrations

The standard calibration of scintillators timing is made in three steps that are not independent. So one has to do several times the three calibrations in an iterative process.

The first step consists in plotting the coincidence time T_{AB} between the two spectrometers for the complete setting. Then the global timing offset is modified in order to center the T_{AB} distribution on zero, as presented in figure 4.5.

Secondly, the same type of correction has to be applied per scintillator paddle. Indeed the signals from some paddles could start sooner and be compensated by signals from other paddles which start later; this gives a global timing spectrum which is well centered on zero but wider than it should be. So the per-paddle signal is homogenized.

The last step is the correction of the "time walk" phenomenon. It occurs when the detection of a signal triggers thanks to a threshold discriminator. Two pulses (having more or less a Gaussian shape) that start at the same time will trigger at different times if their maximum height is different. In Cola++ the true signal start t_0 is approximated by:

$$t_0 = t - b \cdot \frac{1}{\sqrt{Q_T}}, \tag{4.2}$$

with t the measured start of the signal, Q_T the total charge collected (in units of ADC) and b a free parameter to calibrate. To do so, one has to check the distribution of scintillator timing versus the signal integral measured by the ADC. If a correlation is observed is has to be removed by changing the free parameter value. This will modify the global timing calibration.

ADC

Scintillators provide timing information but also measure the energy loss of passing particles (in units of ADC channel). In our experiment this information can be used for particle identification between π^+ and protons in spectrometer A.

In each paddle the ADC spectrum is composed of two peaks, one corresponding to pions and the other (at higher energy) to protons. The calibration of the ADC
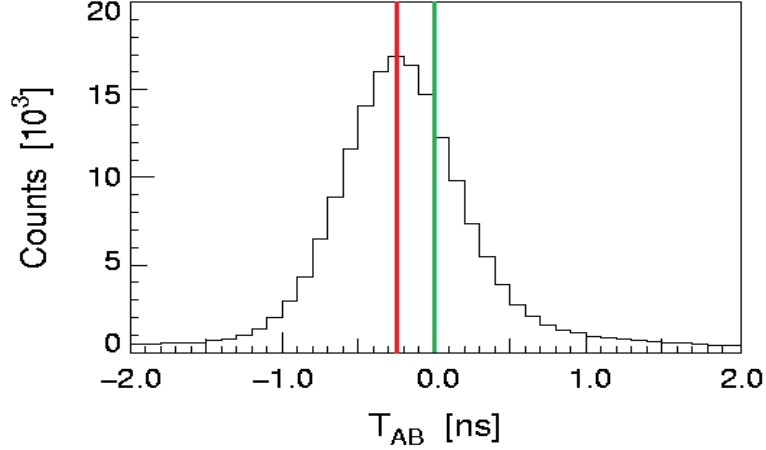
Figure 4.5: Setting INP: coincidence time spectrum between spectrometers A and B before offset correction. The FWHM of the peak is equal to 0.9 ns.

consists in rescaling the spectrum in such a way that pions and protons peaks are aligned for each paddle. Thus, if one wants to perform a particle identification selection the same cut can be applied to every paddle. It has to be done for both scintillator planes (dE and ToF) of the spectrometer A. The calibration description is detailed in [71]. In section 4.3.4 we show that the PID selection based on scintillator is actually unnecessary.

Efficiency

Since the trigger is done by the scintillators, some events may be lost if the scintillators efficiency is not 100%. Indeed there are small inefficiencies which change from a paddle to another. So one has to correct the event loss in order to precisely measure the $ep \rightarrow ep\gamma$ cross section.

For this purpose we use "efficiency runs" taken with a specific target, the carbon target. Since one cannot measure the efficiency of the triggering plane, two runs are required, one with the dE plane as a trigger and the other with the ToF plane as a trigger.

The efficiency of a scintillator plane is determined as the ratio:

$$\epsilon^{eff} = \frac{N_{track \cap TDC}}{N_{track}}, \tag{4.3}$$

where N_{track} is the number of (single-arm) events having a good VDC track, and $N_{track \cap TDC}$ is the number of events having in addition a TDC information in the plane under study [80]. The efficiency is determined in small two-dimensional bins in the scintillator coordinates (X_{scint}, Y_{scint}).

The correction is applied to our data as a weight function:

$$f(X_{scint}, Y_{scint}) = \frac{1}{\epsilon^{eff}(X_{scint}, Y_{scint})}, \tag{4.4}$$

for each triggering plane [81]. Usually the efficiency is superior to 98%, it never gets lower than 90% for the worst paddles.

4.1.5 Optics calibration

The spectrometer optics is an essential part of the particle reconstruction. We used as a starting point the transfer matrix files of the A1 distribution; then, adjustments were necessary for our data analysis, due mainly to the high values of central momenta for spectrometer B, and also partially for spectrometer A (see table 3.3.4).

The calibration of spectrometers optics is a broad topic, and sometimes in our case it gives several solutions due to the fact that some adjustments are based only on the M_X^2 variable. Indeed it happens that two different offset choices lead to comparable results in terms of resolution on missing-mass and vertex reconstruction. We then have to stick with a reasonable choice and see how using other optics parameters would affect the extraction of physics observables. This will be considered in the systematic errors presented in section 5.7.

Matrix elements

The first step of optics calibration is the adjustment of polynomial coefficients presented section 3.2.2 and gathered in a tma file.

This was done in [82] for spectrometer B thanks to carbon target runs and sieve-slit collimators which select only particles emitted at well-known angles (θ_0, ϕ_0). The coefficients P_{ijkl} and T_{ijkl} are adjusted until the reconstructed track reproduces the sieve-slit holes configuration.

A second tool is the vertex reconstruction for cryo-target runs. Figure 4.6 shows the typical shape of the target along the beam axis as seen by spectrometer B; the peaks at the edges are caused by the walls of the target which generate more particle at our kinematics. The calibration of spectrometer B optics coefficients Y_{ijkl} is optimal when the peaks are sharper.
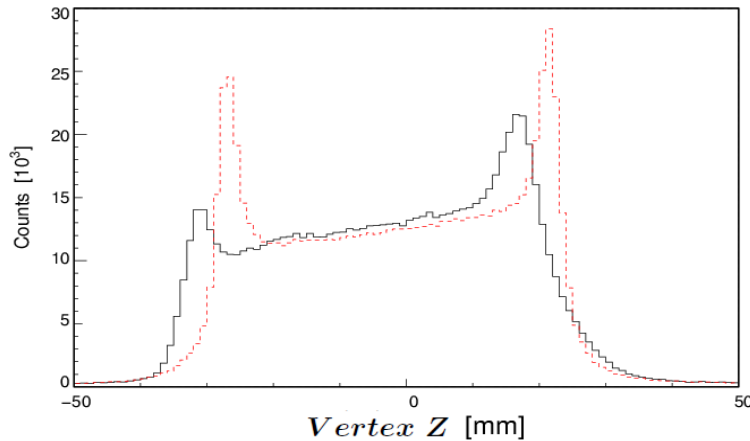

Figure 4.6: Vertex reconstruction for the setting INP. *Vertex Z* is reconstructed with the standard optics from A1 (black) and with our optimized optics (red), for which the reconstruction has improved.

General offsets

Beside the calibration of polynomial coefficients we had to adjust supplementary coefficients that correspond to global offsets of the four target coordinates $(\delta, \theta_0, y_0, \phi_0)$. For instance a 2 mm shift of the target position along the beam axis is taken into account by a supplementary coefficient, called $\Delta Y_0(B)$.

The angular offsets $(\Delta\theta_0(A), \Delta\phi_0(A), \Delta\theta_0(B), \Delta\phi_0(B))$ were adjusted thanks to symmetry properties of our cross section. For instance the geometry of our experiment constrains the (θ_0)-spectrum to have symmetrical edges for the in-plane settings. If it is not the case, global offsets $\Delta\theta_0(A)$ or $\Delta\theta_0(B)$ are applied to correct the distribution.

The $\Delta Y_0(B)$ coefficient was corrected thanks to carbon runs. We assumed that the carbon target is well-centered in the A1 hall and used this information to modify $\Delta Y_0(B)$ until we obtained a reconstructed vertex centered on $\bar{z}_{carbonfoil} = 0$.

This simple procedure is complicated by transverse beam position effects, as presented later in section 4.2.1. The consequence is that one has to carefully select a carbon run with a beam well-centered transversally ($x_{lab} = 0$) in order to calibrate $\Delta Y_0(B)$. The difficulty to select such runs is explained 4.2.1 for the cryo-target and is the same for the carbon target.

Our calibration of $\Delta Y_0(B)$ lead to consider an off-centered cryo-target:

$$Z^{lab}_{cryo-target} = -2.2 \pm 0.5 \ (mm) \ .$$

The same order of magnitude of off-centered values (-2 to $-3 \ mm$) was found for other data sets of our experiment and also confirmed independently by other experiments [83].

Magnets saturation in spectrometer A

The spectrometer-A optics we used is valid in a wide momentum range. However, magnet saturation effects occur above a certain field value. Typically this will affect the track reconstruction of particles having a momentum larger than ≈ 580 MeV/c. This is the case for the in-plane setting.

A specific calibration led to make small changes in the coefficients P_{0010}, P_{1010} and T_{0100} of spectrometer A [84] for this setting.

Beside the coefficients correction one also has to change the reference momentum in spectrometer A, indeed the saturation of the magnetic field changes its value. To consider this, an analytic parametrization was determined by J. Roche and is described in her thesis [78]. For our in-plane setting, we applied the following correction to the spectrometer A central momentum ($P^{central}_A = 1.0476203 * P^{ref}_A$):

$$P^{central}_A = 579.954 - 0.278(MeV/c),$$

579.954 being the value measured by the NMR probe.

4.2 Specific raw data calibration

After our first-pass analysis we observed important inconsistencies in our cross-section measurements. They were caused by unexpected features. In this section we present how we successfully solved these issues in our final analysis.

4.2.1 Beam position

During the analysis of our settings an issue concerning the beam position was found. The beam position is not as stable as we thought. The beam conditions are checked continuously, but its exact position on the cryo-target (or carbon-target) cannot be observed by MAMI operators.

At the beginning of data taking the beam position is fixed by eye thanks to an aluminum screen. Figure 4.7 shows a snapshot of the aluminum screen hit by the beam. Then the beam is turned off, the aluminum screen is replaced by the cryo-target, and the beam is turned on again. At this point there is no possibility to check its exact position versus time.
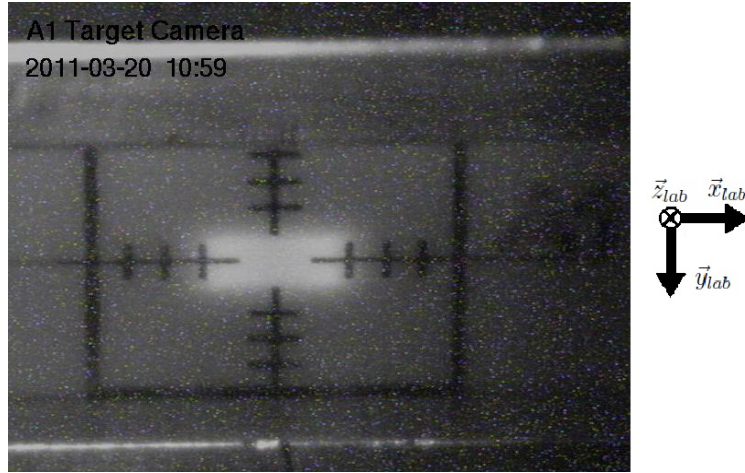
Figure 4.7: Snapshot of the aluminum screen hit by the beam. The composition of the screen makes it glow where the electrons strike it. The bright rectangle shows the wobbler size in horizontal (x) and vertical (y); here ($\pm 2\ mm$)($\pm 1\ mm$).

However, there is a way to establish its position over time in the $\vec{x}_{lab}$ direction. This position, which is averaged over the wobbler, is noted $X_{beam,lab}$. Indeed the vertex reconstruction by spectrometer B depends directly on $X_{beam,lab}$.
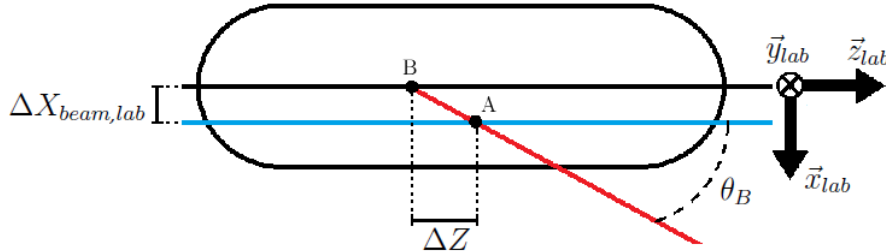
Figure 4.8: (Top view) Schematic representation of the error ΔZ on the reconstructed vertex position induced by an error on the beam position $\Delta X_{beam,lab}$.

Figure 4.8 is a schematic representation of how the beam position acts on the vertex reconstruction. A change of beam position along $\vec{x}_{lab}$, from the black line

to the blue line, induces a change in the reconstructed vertex point, from B to A in the figure. The change ΔZ in the longitudinal vertex coordinate is given by:

$$\Delta X_{beam,lab} = \Delta Z * tan(\theta_B). \tag{4.5}$$

The target centering along $\vec{z}_{lab}$ can be measured run per run, using the $Vertex\ Z$ spectrum as shown in figure 4.6. We make the simple and reasonable assumption that, in reality, the cryo-target does not move along $\vec{z}_{lab}$ throughout our data taking.

If we observe some instabilities in the reconstructed Z-position of the target with time, as shown by the upper plot of figure 4.9, very likely it was the beam position which was unstable instead. Then we can adjust the value of $X_{beam,lab}(t)$ in software, in order to stabilize $Vertex\ Z$. In practice this is done by adjusting the parameter $Beam.offset.x$ in the run.db file, for groups of runs. The result is shown in the lower plot of figure 4.9. The spread of the reconstruction has changed from $\pm 0.5\ mm$ to $\pm 0.2\ mm$.
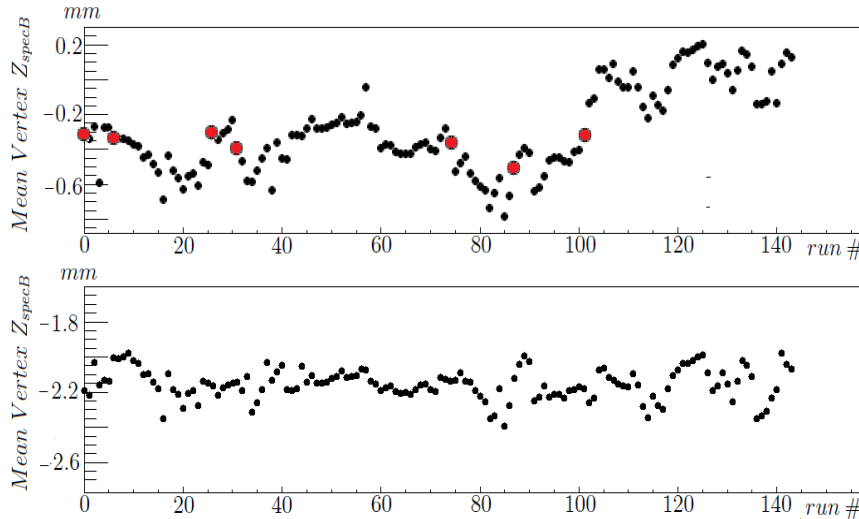
Figure 4.9: Mean position of the reconstructed $Vertex\ Z$ by spectrometer B for all the runs of the setting INP chronologically ordered. The top figure is for $Beam.offset.x = 0$ and $Y_{specB} = 0$, the bottom figure is after corrections: $Beam.offset.x$ adjusted per groups of runs, plus a global offset $\Delta Y_0(B)$. The red dots stand for runs taken just after a beam positioning using the aluminum screen.

4.2.2   Snow thickness and spectrometer B momentum

The spectrometer B reference-momentum P_B^{ref} is measured by a Hall probe with a precision not better than a few percent[1]. If the value considered by Cola++ is different than the real one this will make the missing mass resolution wider.

---

[1] P_A^{ref} is measured with a much better precision by an NMR probe.

The cryo-target cell is cooled to around 22 °K, which is cold enough to adsorb any residual gas molecule in the vacuum chamber that comes into contact with its outer surface. This creates a layer of so-called target snow. The snow quantity mainly depends on vacuum conditions.

The scattered particles will lose energy in this supplementary snow layer, proportionally to the product of snow density by its thickness. This is a parameter, considered by Cola++ and the simulation, which affects the missing mass reconstruction, so it has to be correctly estimated. We chose to work at constant density and adjust only the snow thickness.

The snow thickness and P_B^{ref} are two independent parameters that need to be calibrated using the missing-mass squared resolution.

The calibration, described in [71] and [85], uses two constraints on the reconstructed M_X^2: the peak width has to be minimized while its position has to be centered on the simulated one. The calibration consists then to test a range of values for one of the two parameters and select the optimal offset that minimizes the missing-mass squared width while keeping it well-centered. This will affect the second parameter optimal position and will require it to be calibrated in the same way. Several iterations are needed.

The P_B^{ref} parameter is stable in time but the snow thickness is run-dependent. Indeed the vacuum conditions are not always stable for a complete setting. So, once the two parameters are fixed for the first runs of a setting, the calibration of the snow thickness has to be continued for the following runs. Figure 4.10 illustrates for the setting INP how the increasing snow thickness affects the M_X^2 peak position over time and how we corrected for it.
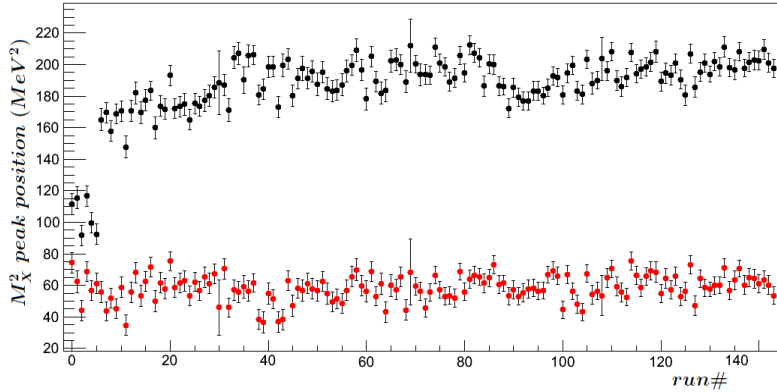
Figure 4.10: Position of the M_X^2 peak with respect to the run label, before (black) and after (red) snow and P_B^{ref} corrections for the setting INP. The error bars are given by the fit of the mean position. The large gap at run #6 corresponds to a large snow deposit after a long beam interruption. During this data taking the snow thickness slowly grows and the peak position slowly increases which result in a small slope on the present figure (black points).

Table 4.2.2 contains the estimated snow quantities (averaged over the runs) for the $Q^2 = 0.2 \ GeV^2$ settings. The vacuum conditions in 2011 for the OOP-setting were so bad that the snow quantity hampers the VCS analysis, the OOP data were collected again in 2015 with perfect vacuum conditions.

Setting	INP	LOW	LOW-bis	2011 OOP	2015 OOP	OOP-forward
Snow thickness (mm)	0.781	0.808	1.28	>4	0	0

Table 4.2.2: Average snow thickness found for each setting with a snow density fixed at $1.g.cm^{-3}$.

4.2.3 Vertical misalignment

Another complication arose from our three in-plane settings, i.e. INP, LOW and LOW-bis. Because of the φ_{cm}-symmetry of the $ep \rightarrow ep\gamma$ cross-section (see figure 4.13) the in-plane data should result in a symmetrical φ_{cm}-distribution of events. Figure 4.11 shows that for the in-plane setting the negative φ_{cm} region contains more events.
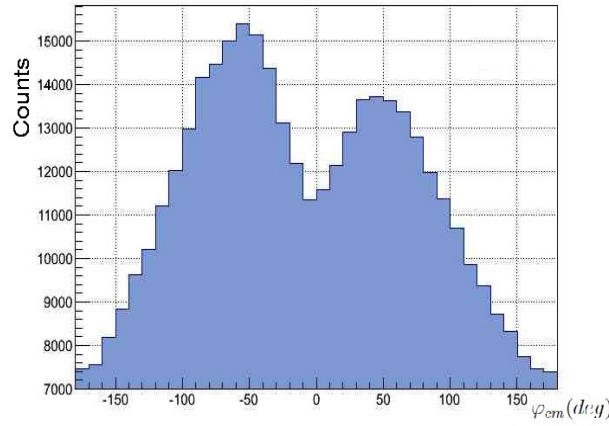
Figure 4.11: Experimental φ_{cm}-distribution for VCS events, setting INP.

We found no combination of spectrometer optics that could give at the same time a symmetrical φ_{cm}-distribution and a minimized missing-mass resolution. Therefore we concluded that our experiment effectively suffers from a vertical misalignment. The calculation of the φ_{cm} variable involves both spectrometers A and B, therefore the origin of this vertical misalignment cannot be identified unambiguously. We identified four possible causes:

- A vertical beam position offset

This solution is actually unrealistic. To obtain this kind of φ_{cm}-asymmetry the offset should be too big (>2mm) and would have been seen during the data taking.

- A non-zero out-of-plane angle for spec B

It is possible to imagine that the spectrometer B was not exactly in the in-plane position during the 2011 data taking. The study has shown that a 2.7 mrad offset in spectrometer B vertical angle is needed to correct the φ_{cm}-asymmetry. This appears unlikely since it implies a very large spatial displacement at the entrance of the spectrometer (i.e. $2.7mr * 3.368m \approx 9mm$).

72

- A vertical offset of spectrometer collimators

Although this seems unrealistic for spectrometer B (it would also imply a collimator offset of 9 mm), it can be considered for spectrometer A. In this spectrometer, a large offset in vertical angle translates into a small spatial displacement, due to the small target-to-collimator distance (0.565m).

- A small floor sagging in A1

The A1 floor sagging was proven by survey measurements [83] and is probably the most realistic cause of our vertical misalignment. For our three in-plane settings as our spectrometers are approximately in the same angular position (w.r.t. the beam, see table 3.3.4) the floor sagging should lead to the same kind of offsets.

Our assumption

A combined effect of those causes is also possible. It is then hard to identify the real offsets, especially because the floor sagging may affect offsets in a complicated way. However we assume that for such a small misalignment any vertical offset among the four listed is equivalent, and we can use any of them as a representation of the reality.

This non-trivial assumption is supported by our tests of different vertical offsets, of various nature. They all lead to the same optimized M_X^2, the same φ_{cm}-distribution and similar cross-section measurement.

We then decided to use the spec-A-collimator offset to correct the vertical misalignment, i.e. to be the representation of our vertical misalignment. We did a missing mass minimization for each of the three settings and obtained three offset values, presented in figure 4.12. This figure 4.12 shows that the three independent results are close (as would be the case for the floor sagging hypothesis). The average obtained offset, of -3.35 mrad, corresponds to a reasonably small vertical displacement of $0.565m * 3.35mr = 1.89\ mm$ at the level of the collimator entrance.

The simulation (see section 4.5) is therefore run with the same spec-A collimator offset : -3.35 mrad. So the simulated φ_{cm}-distribution will also be non-symmetrical but should match the experimental one.

This correction had a strong an positive impact on our measured cross section as illustrated in figure 4.13. This cross section is now symmetric w.r.t. $\varphi_{cm} = 0$, as it should be in theory.

4.2.4 Luminosity corrections

Another unexpected issue arose from the experimental luminosity calculation. The luminosity is given for each run by Lumi++ as presented in section 3.2.4. This luminosity-per-run needs to be corrected from the dead time DT_{run}, i.e. the time after each event during which the detectors are not able to record another event. It is calculated by Lumi++ in % and is used to correct the luminosity for run i as:

$$\mathcal{L}_i^{corrected} = \mathcal{L}_i^{raw} * (1 - DT_i/100), \qquad (4.6)$$

with the dead time which depends on the kinematics, for instance it is equal to 6% for the settings LOW and OOP, for the settings INP it varies from 5 to 8%.
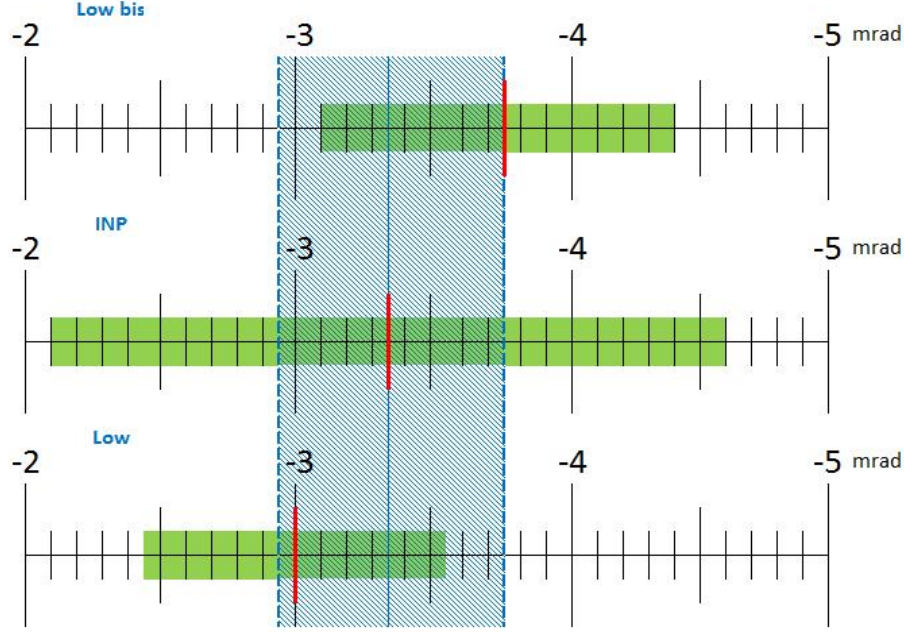
Figure 4.12: Spec-A collimator vertical offset (red line) obtained by missing-mass resolution minimization for three in-plane settings. The error bars (green area) correspond to the fit error on the determination of the minimum. The combined error (dashed blue area) is obtained by the quadratic sum of errors.

The problem was that Lumi++ miscalculated the dead time for some runs. We then built a correction procedure that uses reliable information to recalculate the dead time [86].

First we assume that the dead time calculation is stable from a run to another when the beam conditions are stable. This is the case for a given setting. We observed that, independently of beam current variations, the dead time can be expressed as:

$$DT_i = K \cdot \frac{N_i}{t_i}, \qquad (4.7)$$

with N_i the number of events recorded, t_i the run duration and K a constant linked to the setting that we have to determine.

The second step was then the determination of K. K was adjusted by averaging it on the runs having an initially reliable dead time value. The third and last step used equation 4.7 to recalculate the dead time for non-reliable runs.

The errors generated by this method were estimated from the reliable runs. The error is only up to 1% of the dead time, i.e. negligible.

Later, a modified version of Lumi++ provided by H. Merkel [87] confirmed our result, the corrected luminosities-per-run found by the two methods differ by only 0.09%.
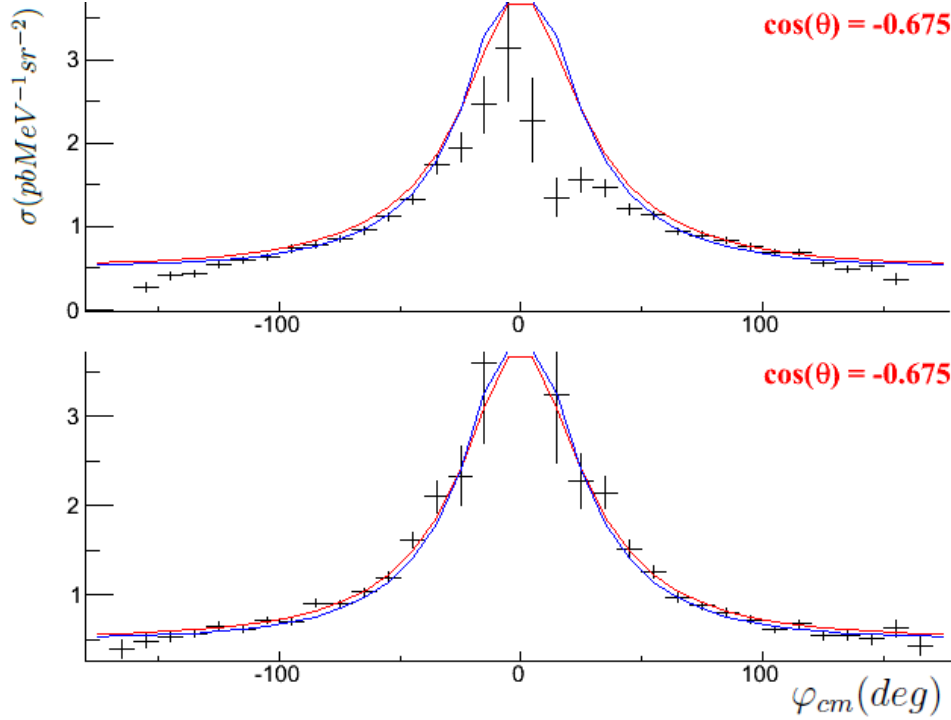
Figure 4.13: Measured cross section (black crosses) at $q'_{cm} = 87.5 MeV/c$ and $cos(\theta_{cm}) = -0.675$ for the setting INP before (top) and after (bottom) vertical misalignment correction. The curves are the theoretical cross section without (red) and with (blue) a GP effect.

4.3 Choice of 3D Binning and Analysis cuts

Now that our detectors are calibrated and that the distributions are corrected we can apply selections in order to only consider $ep \rightarrow ep\gamma$ events for the cross-section measurement. In this section the three mandatory selections are detailed first and the necessity of optional selections is then discussed. Afterwards the binning of the three-dimensional phase-space is presented. Spectrometer-momentum acceptance selections are always used in addition to the discussed selections. One requires $|\delta_B| < 7.5\%$ and $-6\% < \delta_A < 15\%$.

4.3.1 Cut on coincidence time

The time selection is the first mandatory cut. The coincidence time, detailed in section 3.2.3 and provided by scintillators, contains accidental coincidences under the peak of true coincidences that have to be removed.

So we estimate this amount by counting the number of events in the flat part of the distribution at each side of the peak, as presented in figure 4.14. Then we apply a weighted function that subtracts in the selected region the estimated number of accidental coincidences.

The random coincidences represent 6% of the events in the peak region in figure 4.14.
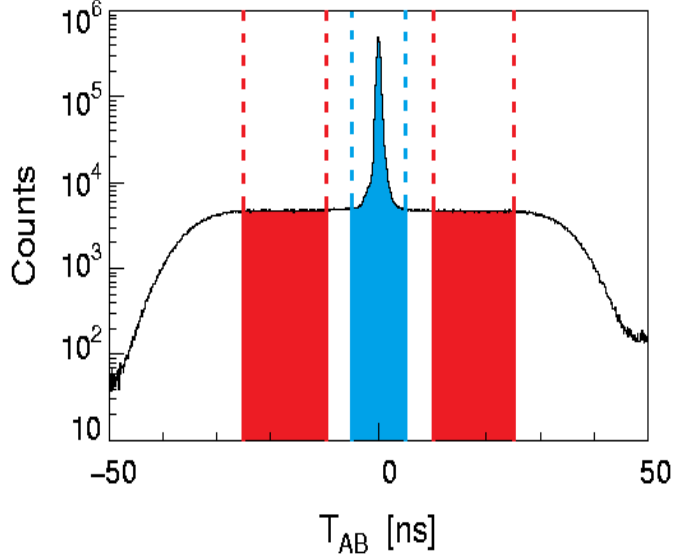
Figure 4.14: Setting INP coincidence time measurement. The red areas are used to estimate the number of accidental coincidences under the peak (blue area). The coincidence-time cut requires $|T_{AB}| < 4\ ns$.

4.3.2 Vertex selection

The vertex selection is the second mandatory cut. As stated before we need protons at rest in order to precisely measure the photon electroproduction cross-section. So we want to remove the population of figure 4.2 (right plot) from figure 4.1.

The target walls are identified in figure 4.6 as peaks, the selection simply consist in requiring $MIN < Vertex\ Z < MAX$ with MIN and MAX chosen sufficiently far from the peaks to include the resolution effects.

4.3.3 Missing-mass squared selection

The M_X^2 selection is the third mandatory cut. As explained in section 4.1.1 the missing-mass squared is a signature of the produced real-photon, it is therefore essential to put a cut on M_X^2 around 0.

The peak has a very long radiative tail for positive M_X^2 which corresponds to events which are reconstructed with a poor resolution due to energy loss of a second radiated photon. The selection will remove them. The cut we applied depends on the width of the M_X^2 peak, and so it varies from a setting to another.

Setting	INP	LOW	LOW-bis	2015 OOP	OOP-forward
M_X^2 lower cut (MeV^2/c^4)	-1000	-1000	-1000	-2000	-2000
M_X^2 upper cut (MeV^2/c^4)	2500	2000	3000	6000	4000
$Vertex\ Z$ lower cut (mm)	-17.7	-15.7	-15.7	-16.7	-16.7
$Vertex\ Z$ upper cut (mm)	12.3	10.3	10.3	11.3	11.3

Table 4.3.3: M_X^2 and $Vertex\ Z$ cuts for every analyzed setting.

4.3.4 PID selection based on energy deposited

At this point it is still possible a priori for unwanted events to pass the previously presented cuts, so we tested if a supplementary selection is required, namely the particle identification (PID) selection based on scintillator ADC signal in spectrometer A.

Figure 4.15 shows the energy deposited by protons and pions in spectrometer A scintillators after their ADC calibration and without the three mandatory selections. The protons deposit more energy and appear as a clear population at the top right of the figure.
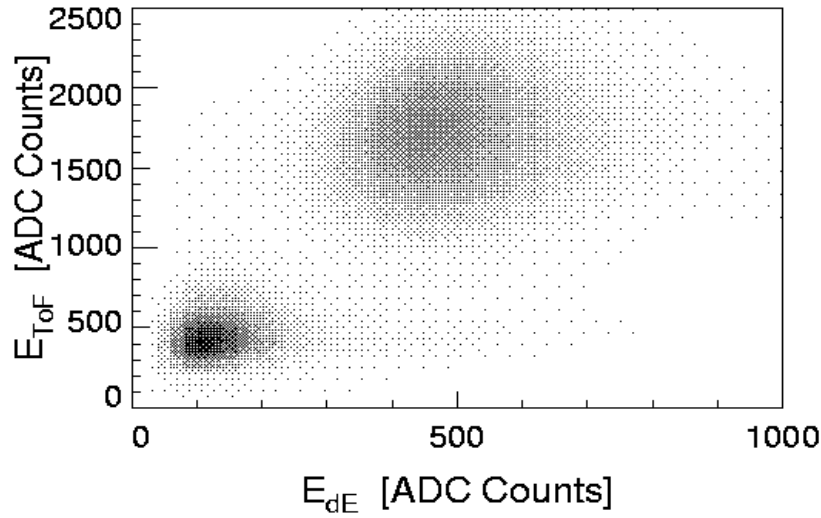
Figure 4.15: Energy deposited by protons and pions in spectrometer A scintillators (in units of ADC channels) after ADC calibration, without any analysis cut, setting INP.

The PID selection would consist in applying a two-dimensional cut on figure 4.15, but it is worthless. Indeed after applying the three mandatory selections the events identified as pions on this figure are strongly suppressed. As an example, for the setting LOW, these events represent only 0.1% of the total.

This result was similar for all our settings and we decided to not apply this selection.

4.3.5 PID selection based on Cerenkov detector

The Cerenkov detector of spectrometer B is used to differentiate π^- froms electrons. Figure 4.16 shows the measured signal for pions, which appears as a narrow peak on the left (it is the electronic pedestal), and for electrons, corresponding to the broad bump. The selection would consist in applying a cut on this figure.

However after applying the three mandatory selections the events identified as pions on this figure represent only 0.3% of the total, therefore we did not apply any Cerenkov cut.

Figure 4.16: Setting INP signal (in units of ADC channels) measured by the spectrometer B Cerenkov detector without analysis selection.

Actually, the three mandatory selections are efficient and sufficient for all our settings. Table 4.3.3-b shows the number of events per setting.
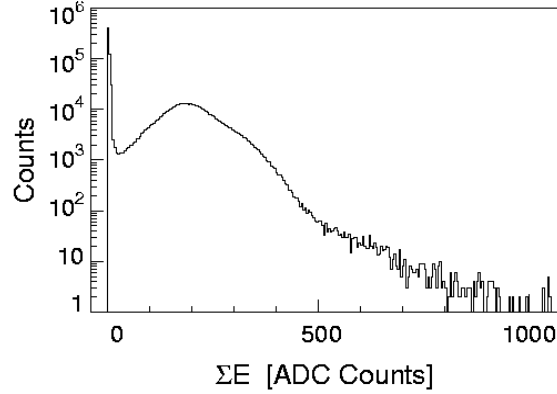
Setting	INP	LOW	LOW-bis	2015 OOP	OOP-forward
Counts	474925	247685	230970	328116	26815

Table 4.3.3-b: Number of events that pass our three selections in each setting.

4.3.6 Three-dimensional binning of the phase space

The phase-space point depends on the five variables of the VCS kinematics (q_{cm}, q'_{cm}, ϵ, θ_{cm}, φ_{cm}). In our settings, two of these variables cover a narrow range, $q_{cm} \approx 458$ MeV/c and $\epsilon \approx 0.85$, therefore they are not binned. The three others are used to build a three-dimensional phase space as presented in table 4.3.6.

	q'_{cm} (MeV/c)	φ_{cm} (°)	$cos(\theta_{cm})$
Bin Width	25	10	0.05
Range	[0;175]	[-180;180]	[-1;1]
Number of bins	7	36	40

Table 4.3.6: Data binning of the three-dimensional phase space.

The analysis contains then $7 * 36 * 40 = 10080$ bins, but a large number of bins are actually empty, i.e. out of the acceptance. The bins width is compatible with the resolution on (q'_{cm}, θ_{cm}, φ_{cm}) which we estimated thanks to the simulation.

4.4 Calibration checks

In this section control plots are gathered in order to conclude on the experimental calibration.

78

4.4.1 Control of the optics quality

The missing-mass squared peak position and the target position in Z are two quantities which should not depend on the reconstructed target coordinates $(x_0, \theta_0, y_0, \phi_0)$ or the focal-plane coordinates $(x, \theta, y, \phi)_{fp}$. By plotting the reconstructed coordinate with respect to the missing-mass squared or to the $Vertex\ Z$ we should then see no correlation. Correlations would be the sign of a residual default in the optics (matrix elements or offsets).
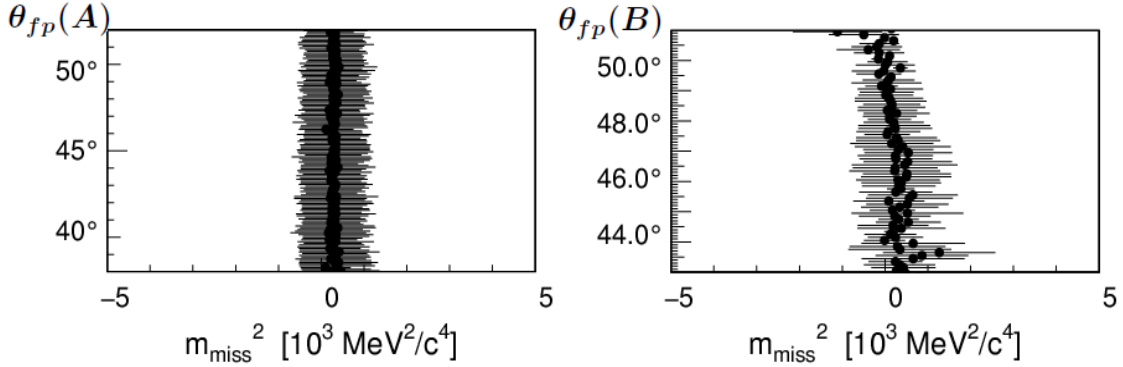
Figure 4.17: Example of optics control plots. (Left) reconstructed θ_{fp} angle by the spectrometer A of the setting LOW-bis versus M_X^2. (Right) reconstructed θ_{fp} angle by the spectrometer B of the setting OOP 2015 versus M_X^2.

For each spectrometer variable and each setting we checked the absence of such correlations. Figure 4.17 shows two examples of missing-mass squared control plots. The left one is obtained for the spectrometer A of the setting LOW-bis, no correlation appears between $\theta_{fp}(A)$ and the missing-mass. The right plot shows a small correlation for the spectrometer B of the 2015 OOP setting. This is nevertheless the best we could obtain and we consider that such a small correlation has no consequence on our measurement.

Figure 4.18 illustrates a well-reconstructed $Vertex\ Z$. The target shape clearly appears and does not depend on the reconstructed variable $\theta_{fp}(B)$.

The optics we used satisfies our correlation criteria, since only small correlations remain. It is impossible to obtain perfect optics. We chose one optics as a reference for the nominal analysis, and other solutions for optics have been considered for the purpose of systematic studies.

4.4.2 Event rate stability

Another control allows to check in the same time the consistency of our data selection and the quality of our luminosity calculation. It consists in calculating for each run the number of $ep \rightarrow ep\gamma$ events divided by the dead-time corrected luminosity of the run.

For each run i, the number $\mathcal{N}_{ep \rightarrow ep\gamma}$ of $ep \rightarrow ep\gamma$ events can be expressed as:

$$\mathcal{N}_i^{ep \rightarrow ep\gamma} = \mathcal{L}_i^{corrected} \cdot \int \frac{d^5\sigma}{d\Omega^5} d\Omega^5, \tag{4.8}$$
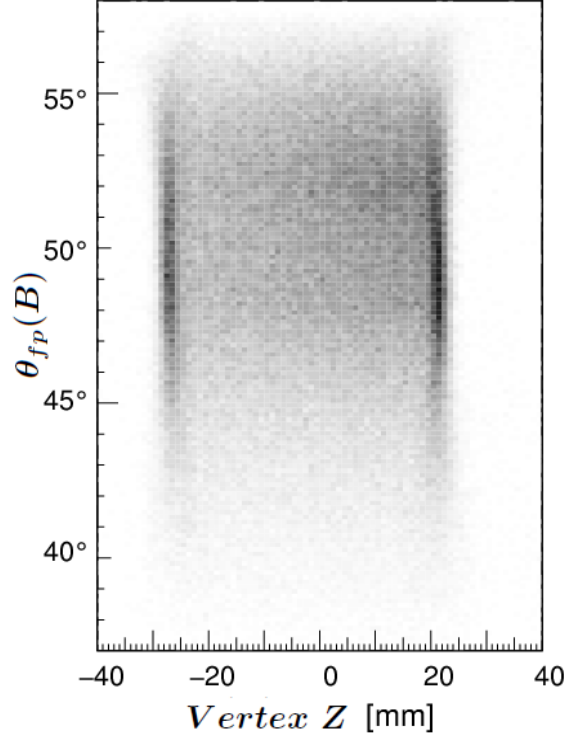
Figure 4.18: Reconstructed angle θ_{fp} by the spectrometer B of the setting LOW-bis with respect to the reconstructed vertex position. The darker areas correspond to the target walls. As expected, the shape of the target does not depend on the $\theta_{fp}(B)$ angle.

where the integral (presented in more detail in section 5.3) is essentially run-independent. So the ratio $\mathcal{N}_i^{ep \to ep\gamma}/\mathcal{L}_i^{corrected}$ must be run-independent (for a given setting).

Figure 4.19 shows this ratio with respect to the run label for the 2015 OOP setting. Each run has its own length but the ratio is constant over time. This is not true for one run which will be removed of the analysis (this run was interrupted during data taking because of detector issues).

The ratio for the INP setting shows a particular shape, figure 4.20. Indeed after the run 70 the beam current was increased from 10 μA to 15 μA. This seems correlated with a $\approx 2\%$ decrease of the plotted ratio. We believe that the current was too high for the second part of the data taking and that it was responsible of a slight local target boiling. This phenomenon changes the target density in a way that is not always detected by the sensors.

From those data we calculated that the luminosity for the second part of the setting is overestimated by 2% and this corresponds to a 1% overestimation of the total INP setting luminosity. So we apply this 1% in our nominal analysis and consider its effect in our calculation of the systematic error (presented in section 5.7).

The settings LOW and LOW-bis presented a constant ratio. Thanks to this control plot we know that we can trust the luminosity calculation and the data

Figure 4.19: Ratio of $ep \rightarrow ep\gamma$ events divided by the corrected luminosity for each run of the setting OOP-2015 with its statistical error. The ratio is expected to be constant.
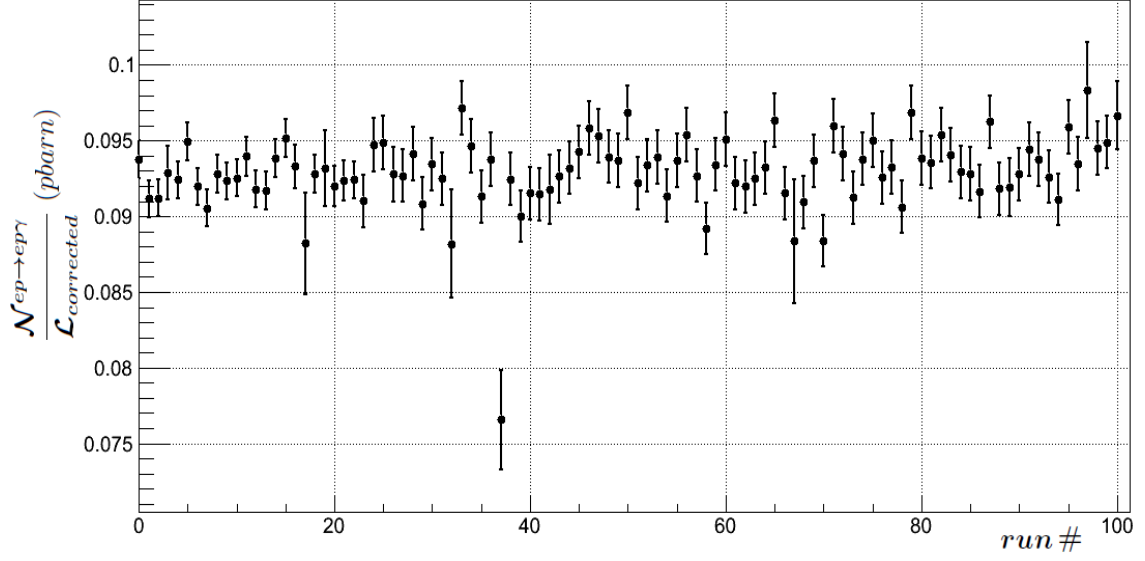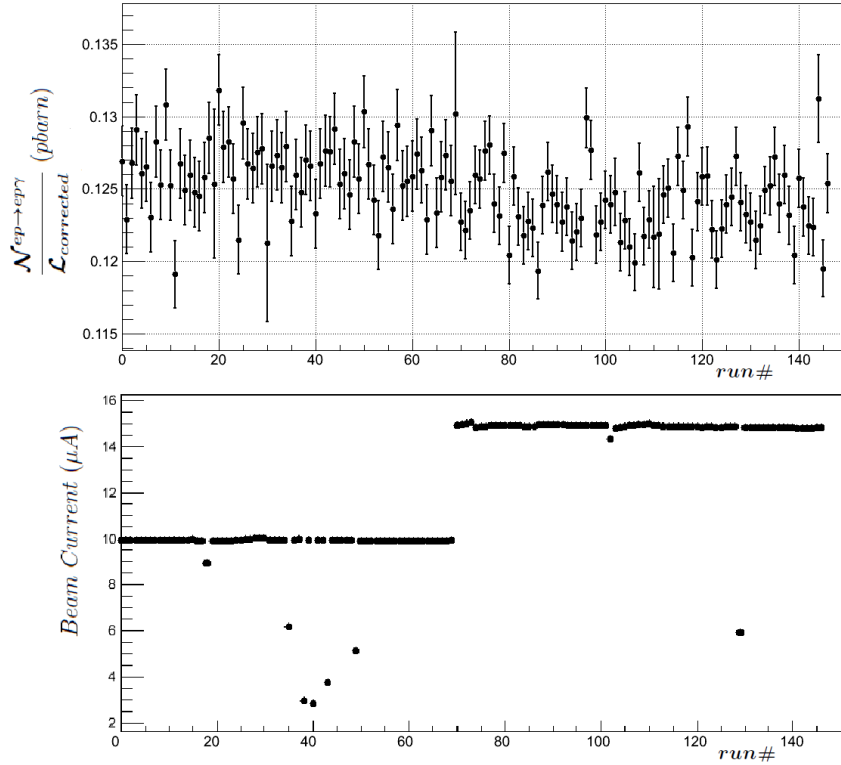

Figure 4.20: (Top) ratio of $ep \rightarrow ep\gamma$ events divided by the corrected luminosity for each run of the setting INP: The ratio is slightly decreased after the run # 70. (Bottom) beam current for each run of the setting INP.

81

selection.

4.5 The Monte Carlo Simulation: VCSSIM

The simulation is a mandatory tool for VCS analysis. It is necessary for the determination of the absolute cross section and also provides essential informations to understand possible experimental problems.

The Monte Carlo simulation VCSSIM was first developed at Gent University by L. Van Hoorebeke for the needs of the first VCS experiment at MAMI. It was then adapted to the JLab hall A spectrometers, and later, Peter Janssens implemented supplementary useful features [76]. This last version is the one we used for our GP extraction, up to small modifications.

VCSSIM is composed of three separate Fortran codes corresponding to three steps:

- The first step generates photon-electroproduction events at the target level according to a given cross section. Then energy loss from ionization and multiple scattering are considered along the path from the target to the spectrometers entrance in order to reject events out of the experimental acceptance.

- The second step applies spectrometer resolution to the generated events. The deterioration of target variables in the simulation allows to reproduce the experimental behavior caused by the VDC resolution.

- The third and last step is the reconstruction of events from the previous step ouput. The variables thus obtained can be analysed with event selection cuts and be compared to the experimental spectra. If the whole procedure is correctly applied the distributions from Cola++ and VCSSIM should match.

In addition to the event generation, VCSSIM also calculates a simulated luminosity $\mathcal{L}_{sim}$ which has to be used for the cross-section measurement (see section 5.3.1).

The VCSSIM program is fully detailed in [88]. In this section its main features are summarized.

Event generation

Before the event generation a simulation phase-space is determined, i.e. a range of values for each of the five variables $(k, k', \theta_e, \theta_{cm}, \varphi_{cm})$ is fixed. Two constraints determine the size of the simulated phase-space. Firstly, it has to be large enough to generate every particle that could reach the spectrometers acceptance. Since energy loss and multiple scattering affect the direction and momenta of particles, the simulated phase space has to be larger than the angular and momentum acceptances of the spectrometers. Secondly, it has to be not too large in order to save calculation time.

Then the event generation starts and an interaction point is sampled. The generation takes into account the beam position (including the wobbler information) and the beam energy loss in the target. The full photon-electroproduction kinematics is generated, by sampling uniformly in $(k', \theta_e, \varphi'_e, \varphi_{cm}, cos(\theta_{cm}))$, with φ'_e the angle between the scattering plane and the horizontal plane containing the

axis of the spectrometers. Instead of the acceptance-rejection method used in [88], here we use all samples that go through the acceptance, and the σ^{BH+B} cross section is used as a weight to the event. This procedure increases the efficiency of the Monte Carlo. The price to pay is a special treatment of the statistical fluctuations induced by the simulation (see section 5.3.1). The part of the radiative corrections that is acceptance-dependent (i.e. internal Bremsstralhung) is also included at this level.

Finally energy losses and multiple scattering are applied to the outgoing particles which are tracked up to the entrance of the spectrometers. Here, the simulation rejects events that do not pass through the collimators, or are not in the momentum bandwidth of the magnets.

Resolution effects and event reconstruction

To properly reproduce the experimental spectra resolution effects have to be added to the simulation. This is done by the second step of VCSSIM. It reads the first step output, which are the particles coordinates at the target level, and computes their focal-plane coordinates using a transfer matrix.

Then, in the focal plane, two types of errors are sampled: the multiple scattering in the detector materials and the resolution of the wire chambers. Those errors are propagated back to the target [76], where an additional error is also considered in order to reproduce effects such as: magnetic fields imperfections, beam position and energy instabilities, etc.

Finally the simulation's second step provides a file that contains the target variables of the two detected particles, degraded by resolution effects.

The last step of VCSSIM uses the second step output to reconstruct the kinematics of each event in the same way that it is done in the experimental analysis, i.e. by taking into account the energy loss of the particles in the target. By coupling informations from the two spectrometers, one reconstructs all important variables, such as M_X^2, or the variables for the three-dimensional binning: q'_{cm}, φ_{cm} and $cos(\theta_{cm})$. Vertex Z is obtained by coupling informations from spectrometer B and the beam.

Luminosity calculation

The simulated luminosity $\mathcal{L}_{sim}$ is mandatory to measure the photon electroproduction cross-section as it is presented in section 5.3. $\mathcal{L}_{sim}$ is calculated at the end of a simulated run. First a luminosity phase-space (L.P.S) is defined, it is smaller than the acceptance phase-space in the three dimensions $(k'_e, \theta_e, \varphi'_e)$. In the L.P.S the cross section is integrated and the number of samples N is counted. Then the simulated luminosity is given by:

$$\mathcal{L}_{sim} = \frac{N}{\int_{L.P.S} \frac{d^5\sigma}{dk'd\Omega_{e'}d\Omega_{\gamma\gamma,cm}} dk'd\Omega_{e'}d\Omega_{\gamma\gamma,cm}} \tag{4.9}$$

times a correction factor related to the full distribution of incoming momentum k_e [88].

Conclusion

To conclude, VCSSIM is required for two reasons. Firstly, it calculates an 'effective solid angle', i.e. that contains the detector geometry plus the various resolution effects. This quantity is necessary in order to determine a cross section accurately. Secondly VCSSIM gives insights in order to check the experimental data.

The parallel analysis at $Q^2 = 0.1\ GeV^2$, described in [71], was performed thanks to another simulation: Simul++. We benefited from having two simulations to perform agreement tests and the results were in accord at the two percent level.

4.6 Simulated and experimental data comparison

To ensure that both our experimental and simulated data are correctly analyzed we can compare their distribution of observables. In the following figures the normalization of the simulation is fixed in order to correspond to the same luminosity as in experiment, the simulated distributions are obtained by using $\sigma^{BH+B} + GP(LEX)$ as a weight function. We dispose of a large number of observables, reconstructed coordinates, vertex, missing-mass squared, particles momentum, etc...

We found a satisfying matching for each setting. Figure 4.21 is the reconstructed target angle ϕ_0 by the spectrometer A of the setting LOW-bis from VCSSIM (blue) and from experiment (red); the figure shows a perfect matching. Such agreements are obtained for almost all variables.
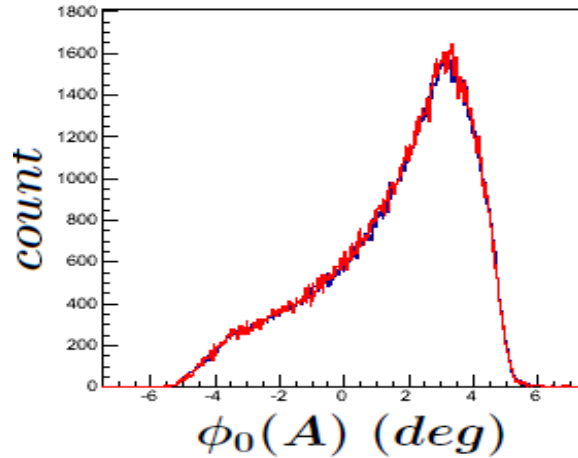
Figure 4.21: Reconstructed target angle by the spectrometer A of the setting LOW-bis from VCSSIM (blue) and from experiment (red). The integral of simulated events is multiplied by the ratio $\mathcal{L}^{exp}/\mathcal{L}^{sim}$.

Only a small disagreement remains. The ϕ_0 angle reconstructed by spectrometer A presents a difference for one specific q'_{cm} bin as presented in figure 4.22. Other choices of optics and offsets can fix this issue but deteriorate other distributions matching. The choice to keep this small disagreement has been considered in systematic error studies.

Finally, figure 4.23 presents the simulated and experimental distributions of the missing-mass squared for the four settings. The only perfect matching appears

Figure 4.22: ϕ_0 angle reconstructed by spectrometer A at $q'_{cm} = 87.5 \ MeV/c$ for the INP setting. A small disagreement is found on the left edge of the distributions.

for the setting INP (bottom left). This is because we optimized the simulated resolution on this one, after this optimization the distributions for 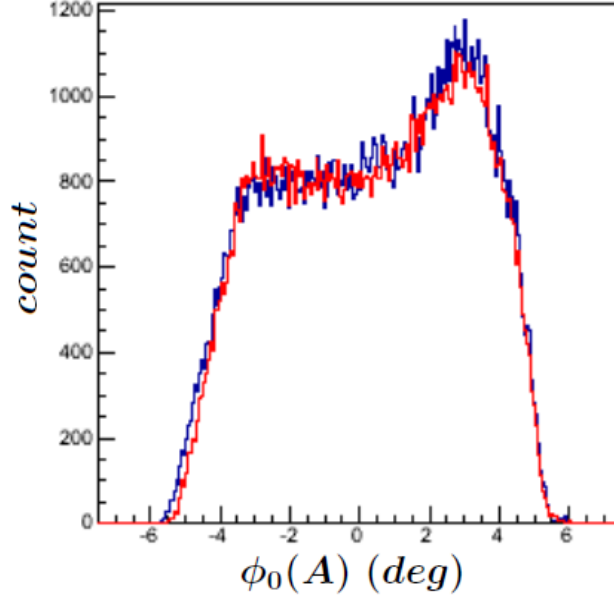the 2015-OOP setting (bottom right) are in less good agreement. This is not an issue since the missing mass cuts are very far from the main peak. For the low energy settings (top right and left), the experimental resolution is slightly better than the simulated one. Globally, the agreement of simulated and experimental distributions for M_X^2 is quite satisfactory.

4.7 Conclusion

The calibrations for VCS analysis have been done extensively. The principal unexpected issues: large snow thickness, vertical misalignment, local target boiling, magnet saturation effects, have been fixed. As an example, the left plot of figure 4.24 shows that the distributions of φ_{cm} from the experiment and from VCSSIM both present an asymmetry w.r.t zero, which is due to the vertical offsets we implemented in the experiment and the simulation. The matching is satisfactory.

The right plot of figure 4.24 is obtained when implementing a GP effect in the weighted function used by VCSSIM, i.e. the weight is calculated as $\sigma BH + B + GP(LEX)$. The rather poor agreement observed between experiment and simulation is due to the omission of the higher-order terms in q'_{cm} in the weighted function. It illustrates the limits of the LEX extraction which is discussed in the following chapter.
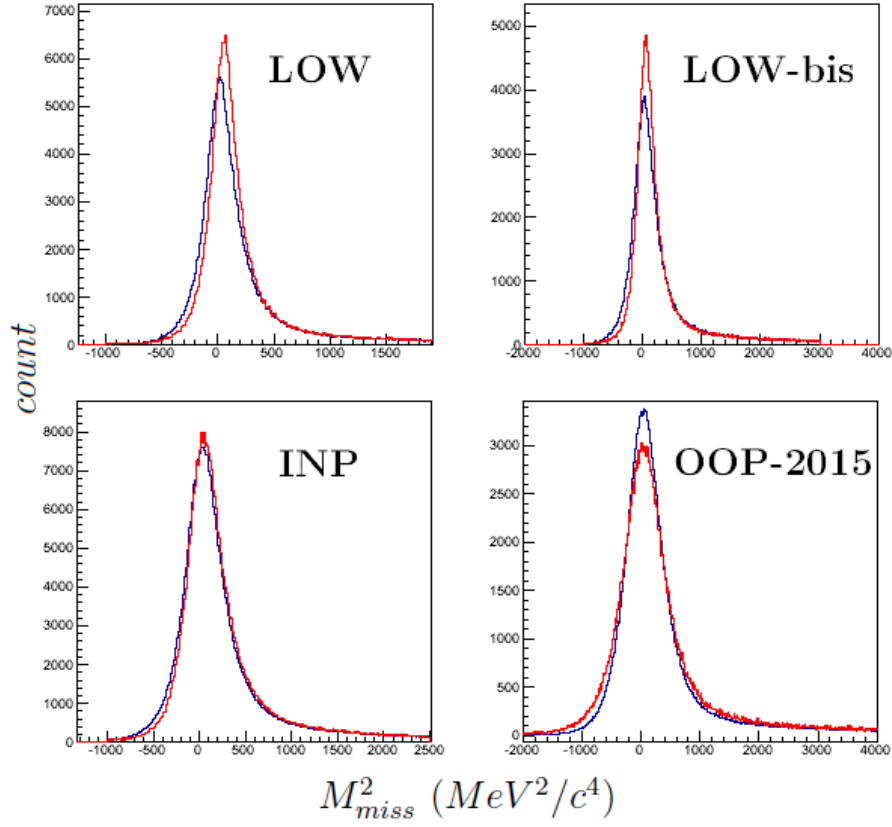
Figure 4.23: Missing-mass squared distributions from VCSSIM (blue) and from the experiment (red) with the fixed normalizations for the four analyzed settings.
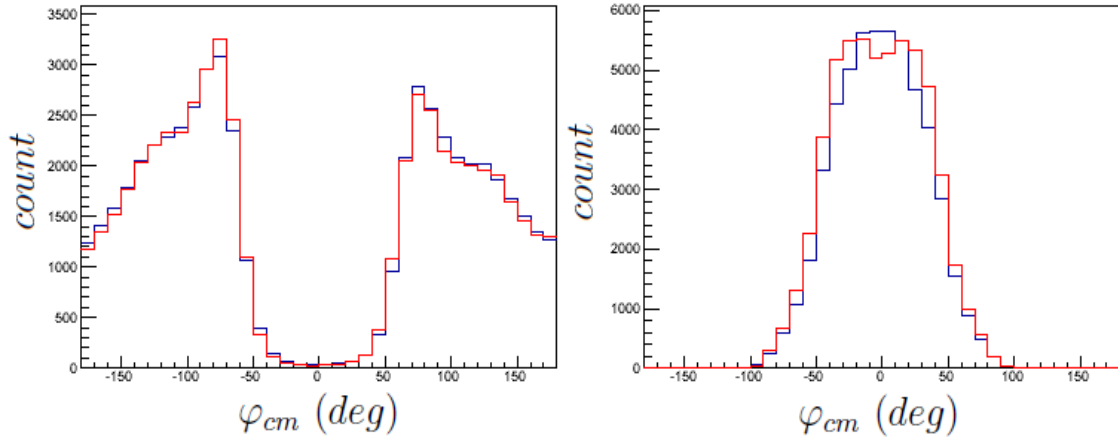

Figure 4.24: (Left) setting LOW φ_{cm} distributions from VCSSIM (blue) and from the experiment (red) with fixed normalizations at $q'_{cm} = 37.5\ (MeV/c)$. (Right) setting INP φ_{cm} distributions, at $q'_{cm} = 112.5\ (MeV/c)$, when one considers a GP effect in VCSSIM (blue).

Chapter 5

Photon electroproduction cross-section and extraction of VCS observables

This chapter describes the second-level analysis: the cross-section determination and the LEX and DR fits yielding the VCS observables: structure functions and GPs.

Section 5.1 presents the theoretical tools we used in the analysis. In section 5.2 we explain the calculation of radiative corrections at $Q^2 = 0.2\ GeV^2$. Section 5.3 is dedicated to cross-section measurement: method and results.

Section 5.4 introduces an important step of the analysis which is the renormalization procedure.

Finally sections 5.5 to 5.8 present the LEX and DR fits and the results in terms of structure functions and GPs.

5.1 Theoretical tools

In this section are presented the two analysis tools essential to the LEX and DR extraction of GPs: the two computer codes which provide respectively the theoretical LEX and DR cross-sections.

In addition to the presented tools we also make use of the A1 software previously presented, especially Cola++[1] .

5.1.1 The BHB code

The BHB code is a C++ program developed by M. Vanderhaeghen [90] which calculates the photon electroproduction cross-section in a chosen point of the phase space $d^5\sigma^{th}(P)$.

The parameters required by the code are the parametrizations of the proton form factors (G_E,G_M) and the five variables ($k, k', \theta_e, \theta_{cm}, \varphi_{cm}$) to define the phase-space point. Then, the user chooses which cross section is calculated by the code among: BH, Born or BH+B. The user can also enter values of structure functions

---

[1]Some graphics contents from Cola++ are drawn thank to ROOT from CERN [89].

$(P_{LL} - P_{TT}/\epsilon, \ P_{LT})$ to calculate the full photon electroproduction cross-section according to the LEX equation 1.38.

5.1.2 The DR code

The second theoretical code, used in our analysis, provides the photon electroproduction cross-section according to the DR model developed by B.Pasquini [91]. Here again the code calculates the theoretical cross section in a point of the phase space $d^5\sigma^{DR}(P)$.

In addition to the kinematical parameters from the $(q_{cm}, q'_{cm}, \epsilon, \theta_{cm}, \varphi_{cm})$-set the code requires values for the DR parameters Λ_α and Λ_β (presented in section 2.1). Just like for the BHB code the user also has to specify a choice of proton form-factor parametrization among the available ones.

To calculate the full DR cross-section the code also needs values of polarizabilities from RCS; they are fixed at the following values from [23]:

$$\bar{\alpha}_E = 12.1 \cdot 10^{-4} \ fm^3 \ ,$$
$$\bar{\beta}_M = 1.6 \cdot 10^{-4} \ fm^3 .$$

5.2 Radiative corrections

Radiative corrections are known to be an important correction to electron scattering processes in general, due to the fact that the electron is a light particle that radiates photons easily.

To study the photon electroproduction reaction $ep \rightarrow ep\gamma$ we only detect the scattered electron and proton, the real photon is identified by the missing-mass method. So we do not control all the processes that occur and which impact the cross-section measurement. For instance an event including a supplementary real or virtual photon could be counted as a first-order photon electroproduction event, while it is not. Such processes, called radiative processes, must be estimated and corrected in order to remove their contribution to the cross section, i.e. the cross section corresponding to the first-order graphs only (see figure 1.6).

This is done by applying a correction factor, F^{rad}, to the measured raw cross-section:

$$\sigma^{exp} = \sigma^{raw} * F^{rad}. \tag{5.1}$$

Radiative corrections to the $ep \rightarrow ep\gamma$ reaction have been studied extensively in [92] which served as a basis for the analysis of all VCS experiments. We will here summarize how we put these calculations into practice, more details can be found in [93]. Generally F^{rad} is written as a sum of contributions which are noted as δ-terms, each one corresponding to a specific process. We consider the following sum:

$$\frac{1}{F^{rad}} \ = \ 1 + \delta_{vac} + \delta_{vertex} + \delta_r + \delta_1 + \delta_2^{(0)}, \tag{5.2}$$

where the δ-terms are explained in section 5.2.1 which also details the specific choices that have been done for our F^{rad} estimation. Section 5.2.2 summarizes the results from [93]: value of the correction and uncertainty.

5.2.1 Physical processes and calculation choices

As can be seen from fig 1.6, the amplitude of the bare diagrams is of order (e^3), leading to a cross-section of order (e^6). Radiative corrections have been calculated [92] to the next order, i.e. including the following contributions:

- the emission of one supplementary real photon (amplitude of order (e^4) and cross-section of order (e^8))

- one supplementary virtual photon (amplitude of order (e^5) interfering with the bare amplitude, (e^3), which leads to a cross-section of order (e^8)).

The supplementary photons can be emitted from the proton side or from the electron side. The calculation of all the δ-terms requires theoretical approximations (like neglecting the higher-order corrections) and the use of model (for the proton-side correction). As a consequence we have to consider a 1% incompressible-theoretical error [92] in our F^{rad} determination.

Some of the diagrams of physical processes are available in appendix C and so are the mathematical equations used to estimate the correction terms. Only the specificities of our determination are presented here.

δ_r: Electron-side supplementary real photon

A large part of the radiative corrections is due to supplementary electron bremsstrahlung of a so-called soft photon. This second real photon may be emitted before or after the hadronic part of the interaction. Figure 5.1 is an example of one of the considered diagrams, where the Bethe-Heitler process comes with one supplementary real photon in red.
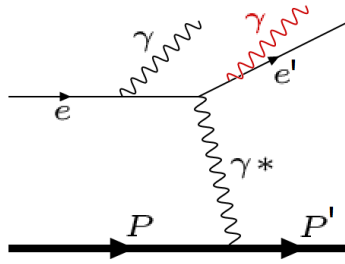
Figure 5.1: One possibility of Bethe-Heitler diagram with one supplementary real photon (red).

Such processes are taken into account through the δ_r term expressed as a sum of two terms: $\delta_r = \delta_{r1} + \delta_{r2}$. δ_{r1} gathers correction terms which depend on ΔE_s and δ_{r2} contains correction terms which do not. ΔE_s is the maximum energy that the soft photon can reach, it depends on the upper cut on the missing-mass squared used in the event analysis:

$$\Delta E_s^2 = \frac{cut}{4}, \tag{5.3}$$

where *cut* is defined in section 4.3 and depends on the settings as presented in table 4.3.3. Typically, an upper cut value of $M_X^2 = 2000 \ MeV^2$ corresponds to $\Delta E_s^2 = 22 \ MeV$.

δ_{r1} and δ_{r2} are an important part of the radiative corrections since they can both reach separately 20% in some analysis bins.

δ_{r1} is already implemented in VCSSIM: applying a missing-mass squared cut to the simulation impacts the final measured cross section in the same way it would be done by adding δ_{r1} to F^{rad}. It is then important to separate δ_r in those two terms in order to not consider δ_{r1} twice in our analysis.

So, the corrections due to supplementary real photon considered in our F^{rad} are only due to the δ_{r2} contribution which is detailed in appendix C.

δ_{vac} and δ_{ver}: supplementary virtual photon

A supplementary virtual photon is produced by three kinds of processes, the vacuum polarization process (figure 5.2): the electron self-energy process (figure C.2) and processes with an additional loop between lines (figure 5.3).
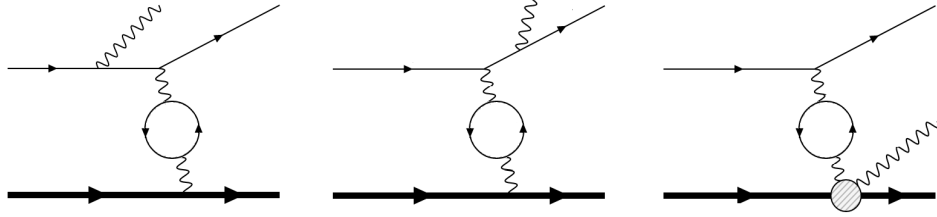

Figure 5.2: Vacuum polarization diagrams. The particles are represented by the line symbols used before.

The virtual-photon contribution that we used has the same expression as the virtual-photon radiative correction to the elastic reaction $ep \to e'p'$. Using the elastic case correction allowed us to avoid the complicated integral calculation involved in the photon-electroproduction case and due to the grahs 1 to 6 of figure 5.3. This choice, supported by the work of D. Marchand [94], leads to a $\approx 0.8\%$ systematic error on the total virtual-photon correction.

The electron self-energy processes, figure C.2, are not considered in our calculation but are a part of the 0.8% error already considered.

δ_1 and $\delta_2^{(0)}$: proton-side corrections

A supplementary photon can also be produced from the proton side, by rare proton bremsstrahlung and vertex corrections. Unlike corrections from the electron side, which can be calculated model-independently from QED, the proton-side corrections will depend on a model for the proton structure. This model dependence will become important if one wants a experimental precision at the 1% level [92].
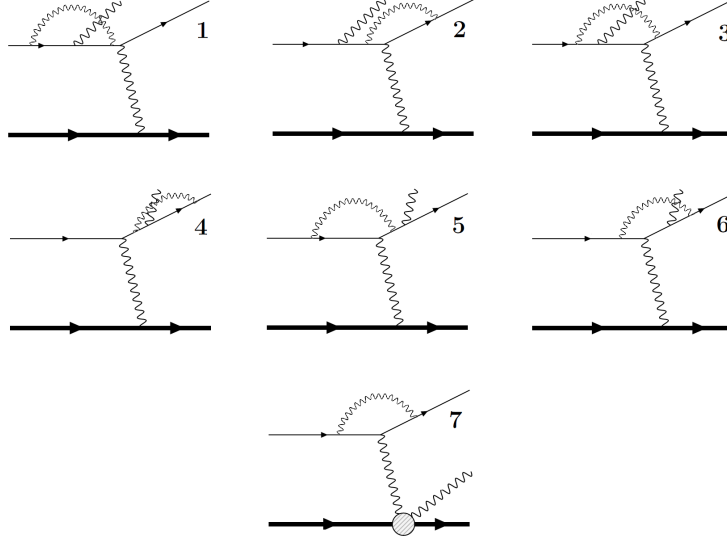
Figure 5.3: Vertex process diagrams.

This correction is described through three terms: $\delta_1, \delta_2^{(0)}$ and $\delta_2^{(1)}$, which also take into account the two-photon exchange process (direct and crossed). The terms considered are from the elastic case but can be applied for photon electroproduction with a negligible error [95].

To determine the proton-side corrections we decided to not consider the $\delta_2^{(1)}$ term; this results in a systematic error on our final F^{rad} which is estimated to be ± 0.002 (this is detailed in appendix C).

Higher-order correction terms

Now, one may consider more supplementary virtual or real photons, the so-called higher-order correction terms. The work presented in [96] proposes to estimate the effect of higher orders by considering a exponentiated form for the correction factor:

$$\frac{1}{F^{rad}} = \frac{e^{\delta_{ver} + \delta_r}}{\left(1 - \frac{\delta_{vac} + \delta_1 + \delta_2^{(0)}}{2}\right)^2} \tag{5.4}$$

By comparing the exponentiated form to equation 5.2, we checked that the higher-order contribution is effectively smaller than the 1% theoretical error which already accounts for it. We finally decided to calculate the radiative corrections by the expression of equation 5.2.

5.2.2 Value of the global radiative correction factor

An important question was to determine if one can apply F^{rad} as a global correction to the measured cross section or if it varies bin-per-bin in $(q'_{cm}, cos(\theta_{cm}), \varphi_{cm})$. This was answered in [93], where the calculation of every correction term in the whole

analysis phase-space showed only very small variations and leads to the conclusion that we can apply a global correction:

$$\frac{1}{F^{rad}} = 1.057 \ .$$

5.2.3 Systematic error on F^{rad}

The first error is generated by the phase-space averaging. Figure 5.4 shows the F^{rad} behavior at $q'_{cm} = 112.5 \ MeV/c$. For those bins one gets $1/F^{rad} = 1.058 \pm 0.002_{RMS}$ (the maximum difference between the averaged F^{rad} and one bin value is ± 0.006).
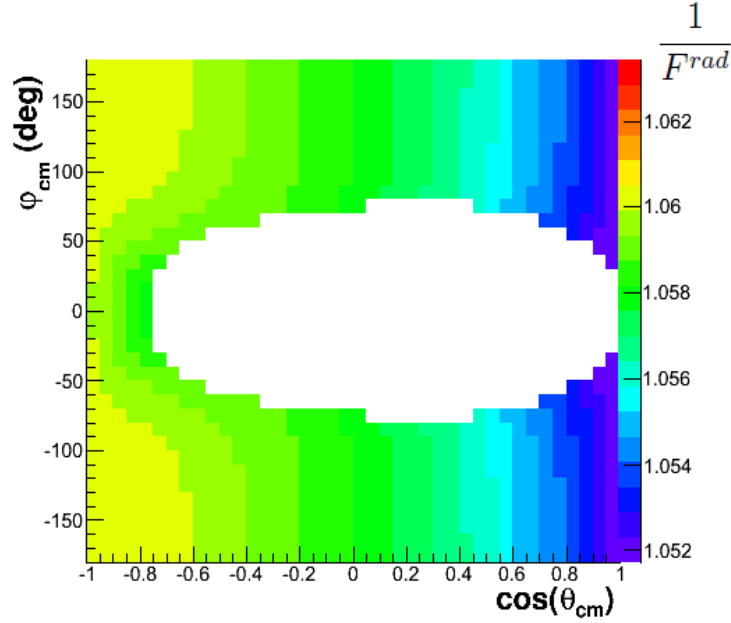
Figure 5.4: $1/F^{rad}$ behavior in the $(cos(\theta_{cm}), \varphi_{cm})$-plane at $q'_{cm} = 112.5 \ MeV/c$. The central part (white) is removed by the gradient-selection (cf. section 5.5.1).

One also has to check the F^{rad} behavior for the bins at $q'_{cm} = 37.5 \ MeV/c$ at which the renormalization is computed (see section 5.4). Figure 5.5 shows that $1/F^{rad} = 1.056 \pm_{RMS} 0.001$ (the maximum difference calculated is ± 0.003) which means that we can consider the radiative correction as a constant in our whole phase space.

A second error is induced by the ΔE_s quantity. Indeed this one varies from a setting to another whereas we used it as a constant in the F^{rad} determination. However we observed that changing it to its maximal variation only induces a ± 0.001 change on $1/F^{rad}$.

The quadratic sum of these two errors leads us to consider a total error induced by our phase-space averaging[2] of ± 0.003 and the maximum variation of F^{rad} is ± 0.007.

The complete error budget on F^{rad} is:

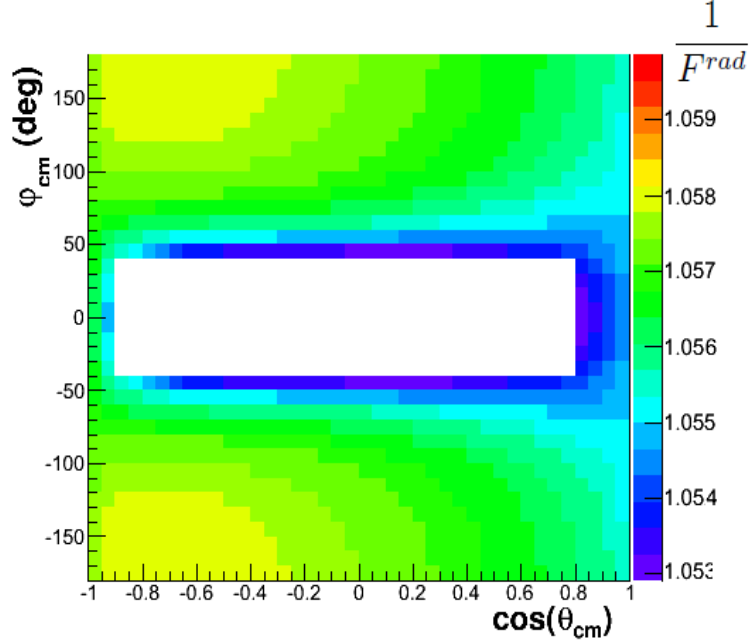[2]The averaging is done with an acceptance cut (the gradient selection), without it the error would have been larger.

Figure 5.5: $1/F^{rad}$ behavior in the $(cos(\theta_{cm}), \varphi_{cm})$-plane at $q'_{cm} = 37.5\ MeV/c$. The central part (white) is removed by an acceptance selection.

$$\Delta\left(\tfrac{1}{F^{rad}}\right) \quad = \pm 0.003_{PSA} \pm 0.01_{theo} \pm 0.008_{EC} \pm 0.002_{PSO}$$
$$= \pm 0.014\ (quadratic\ sum)$$

with:

PSA, the maximum uncertainty brought by our phase-space averaging.

$theo$, the incompressible theoretical error.

EC, the uncertainty brought by our choice to use the elastic-case determination of δ_{vertex} and δ_{vac}.

PSO, the uncertainty brought by the proton-side omission of $\delta_2^{(1)}$.

As a final result, we get:

$$\tfrac{1}{F^{rad}} = 1.057 \pm 0.014,$$

which is used to correct all our cross-section data, using equation 5.1. This factor is also considered in the normalization of experimental distributions when the reconstructed quantities are compared to the simulated ones (section 4.6). The ± 0.014 systematic uncertainty will largely disappear in the renormalization procedure described in section 5.4, and a small remaining part will contribute to our systematic errors.

5.3 Measurement of cross sections

Measuring the cross section of equation 1.38 is the first step of the second-level analysis. We want to extract a GP effect which is a few percent of the cross section,

so the measurement requires enough statistics, and systematic errors reduced to the 1-2% level. To achieve that we used a method based on a simulation (VCSSIM) which is described in [88]. We summarize it in the next sections.

5.3.1 The simulation-based method

First, the classical formula that expresses the photon electroproduction cross-section in one bin is:

$$\frac{d^5\sigma^{exp}}{dk'd\Omega_{k'}d\Omega_{p'_{cm}}} = \left(\frac{d^5\sigma}{d\Omega^5}\right)^{exp} = \frac{N^{exp}}{\mathcal{L}^{exp} \cdot \Delta\Omega^5}, \tag{5.5}$$

with N^{exp} the number of events in the bin, $\mathcal{L}^{exp}$ the experimental luminosity and $\Delta\Omega^5$ the solid angle of the five-dimensional bin. $\Delta\Omega^5$ is difficult to determine in a simple way because the acceptance is not constant in a single bin. So $\Delta\Omega^5$ is reproduced thanks to VCSSIM in order to obtain the cross section by the following method.

From equation 5.5 we have in one experimental bin (i):

$$N_i^{exp} = \mathcal{L}_i^{exp} \iiiint \sigma^{exp}(\Omega)A(\Omega)d\Omega^5, \tag{5.6}$$

where $A(\Omega)$ is the complicated acceptance function which varies between 0 and 1 in the bin and $\sigma^{exp}(\Omega)$ stands for $d^5\sigma/d\Omega^5$. We introduce a point P_0 of the differential phase-space $d\Omega^5$ which is, in our case, the center of the bin. The differential cross section in any point P of the considered bin can be expressed as:

$$\sigma^{exp}(P) = \sigma^{exp}(P_0)\left[1 + \frac{\sigma^{exp}(P) - \sigma^{exp}(P_0)}{\sigma^{exp}(P_0)}\right]. \tag{5.7}$$

Applying this to equation 5.6 leads to:

$$\frac{N_i^{exp}}{\mathcal{L}^{exp}} = \sigma^{exp}(P_0) \iiiint \left[1 + \frac{\sigma^{exp}(\Omega) - \sigma^{exp}(P_0)}{\sigma^{exp}(P_0)}\right]A(\Omega)d\Omega^5. \tag{5.8}$$

Now, if one makes use of a simulation faithful to the experiment, equation 5.8 can be written for the simulated events as well:

$$\frac{W_i^{sim}}{\mathcal{L}^{sim}} = \sigma^{th}(P_0) \iiiint \left[1 + \frac{\sigma^{th}(\Omega) - \sigma^{th}(P_0)}{\sigma^{th}(P_0)}\right]A(\Omega)d\Omega^5, \tag{5.9}$$

with W_i^{sim} the number of events in the simulated bin (in our case it is a weighted sum, the weight being the theoretical BH+B cross section). $\mathcal{L}^{sim}$ is the luminosity calculated by VCSSIM and $\sigma^{th}(P_0)$ can be either the BH+B cross section or the BH+B cross section increased by a theoretical GP effect. In our case we did not implement a GP effect in $\sigma^{th}(P_0)$ but we considered this possibility in the systematic studies of section 5.7.2.

The integrals of equations 5.8 and 5.9 can be considered as very close, since σ^{th} reproduces well the relative variations of the true cross section in the bins.

Finally, using equations 5.8 and 5.9 leads to the important cross-section determination formula:

$$\sigma^{exp}(P_0) = \frac{N_i^{exp}}{W_i^{sim}} \cdot \frac{\mathcal{L}^{sim}}{\mathcal{L}^{exp}} \cdot \sigma^{BH+B}(P_0). \qquad (5.10)$$

To calculate $\sigma^{BH+B}(P_0)$ we can choose different form-factor parametrizations as discussed in section 1.1.2. Here, one just needs to use the same parametrization for the theoretical cross section ($\sigma^{BH+B}(P_0)$) and for the BH+B cross section used as a weight event per event, in W_i^{sim}. Indeed, a change of form-factor parametrization roughly acts as a rescaling of the cross section (see section 5.4.3), which is canceled in the ratio $\sigma^{BH+B}(P_0)/W_i^{sim}$. In this way the measured cross section will not depend on the form-factor parametrization choice, in first approximation.

5.3.2 Statistical error

Once the experimental cross section from equation 5.10 is measured we have to determine its statistical error. We considered statistical fluctuations coming from the experimental and simulated number of counts:

$$\frac{\Delta \sigma^{exp}}{\sigma^{exp}} = \sqrt{\left(\frac{\Delta N_i^{exp}}{N_i^{exp}}\right)^2 + \left(\frac{\Delta W_i^{sim}}{W_i^{sim}}\right)^2}. \qquad (5.11)$$

The statistical error on $\mathcal{L}_{sim}$ is negligible, by construction of VCSSIM. The error on $\mathcal{L}_{exp}$ is of systematic nature and will be addressed in section 5.7.

N_i^{exp} depends on the coincidence selection described in section 4.3. Its statistical error is then calculated by considering the fluctuations from event counts both in the coincidence peak and in the accidental plateau.

As explained in section 4.5 we implemented a weight-procedure in VCSSIM: W_i^{sim} in bin i is equal to the sum $\sum_j^{N_i^{sim}} w_j$, with $w_j = \sigma^{BH+B}(j)$. For such quantities the statistical fluctuations give [97]:

$$(\Delta W_i^{sim})^2 = \frac{N_i^{sim}}{N_i^{sim}-1} \left[\left(\sum_j^{N_i^{sim}} w_j^2\right) - (< W_i^{sim} >)^2 \right], \qquad (5.12)$$

with $< W_i^{sim} >$ the mean of the weight distribution. In our case it can be simplified to the following expression [97]:

$$(\Delta W_i^{sim})^2 = \sum_j^{N_i^{sim}} w_j^2. \qquad (5.13)$$

The simulation is run on a larger statistics than the experiment, so that the term $\Delta W_i^{sim}/W_i^{sim}$ is not dominant in equation 5.11.

5.3.3 Cross-section results

We measured 7784 cross-section points distributed in the five settings, some of them are presented in the next figures. They are obtained without renormalization factor, but they are corrected from the radiative processes by means of the factor F^{rad} (i.e $\sigma^{exp} = \sigma^{raw} * F^{rad}$).

In the analysis some bins have a low number of events, typically bins at the acceptance edges. These bins are removed at the cross-section level by a cut on N_i^{exp}:

$$N_i^{exp} > 20.$$

No cut was applied on the number of simulated events which are more numerous per bin in our case.

Figure 5.6: Setting LOW: measured $ep \rightarrow ep\gamma$ cross section at fixed $q'_{cm} = 37.5 \ MeV/c$ with respect to φ_{cm} for the first-half of $cos(\theta_{cm})$-bins. The error bars are statistical. The blue full line is the theoretical cross section σ^{BH+B}, the red dotted line is σ^{BH+B} plus a polarizability effect calculated by the LEX with $P_{LL} - P_{TT}/\epsilon = 18.1 \ GeV^{-2}$ and $P_{LT} = -3.6 \ GeV^{-2}$.

Figures 5.6 and 5.7 present the measured cross section from the setting LOW at fixed $q'_{cm} = 37.5 \ MeV/c$; this setting covers a wide range in $(cos(\theta_{cm}), \varphi_{cm})$. The points follow the theoretical curves (BH+B) and (BH+B + GPs), which cannot
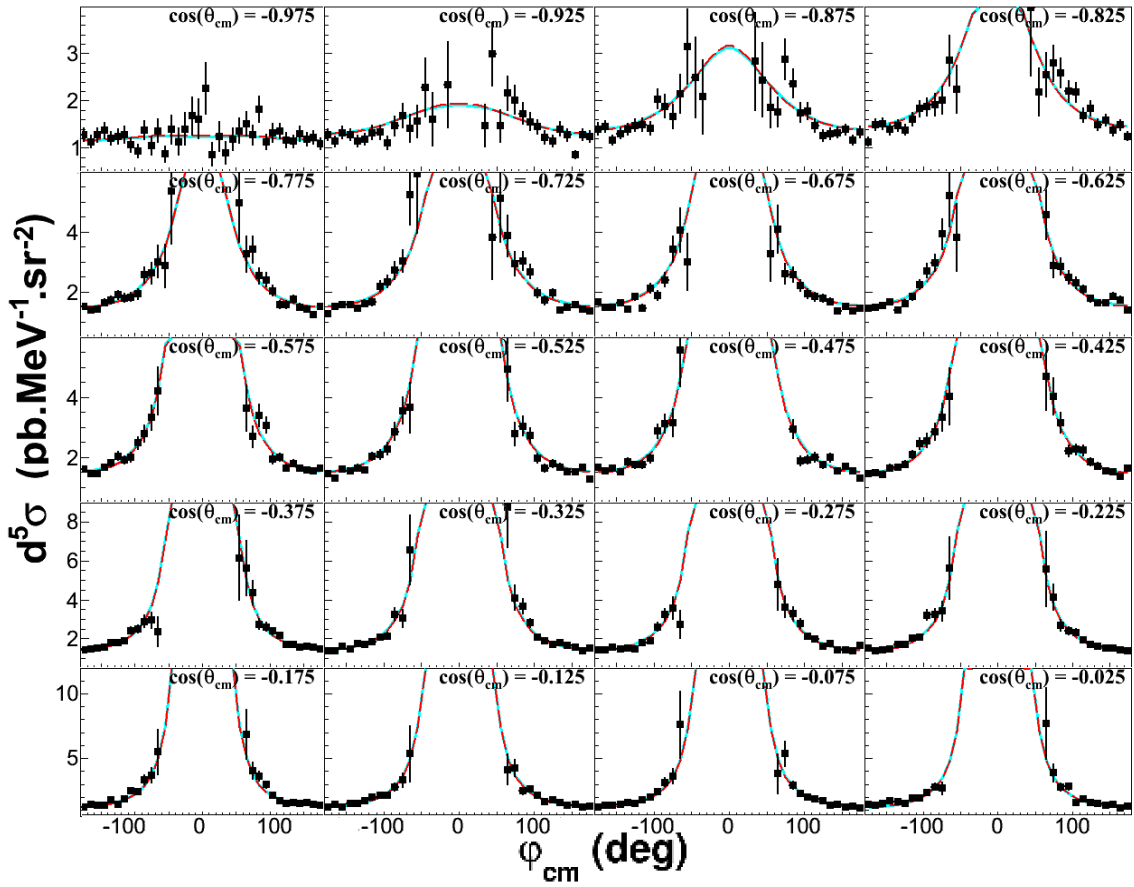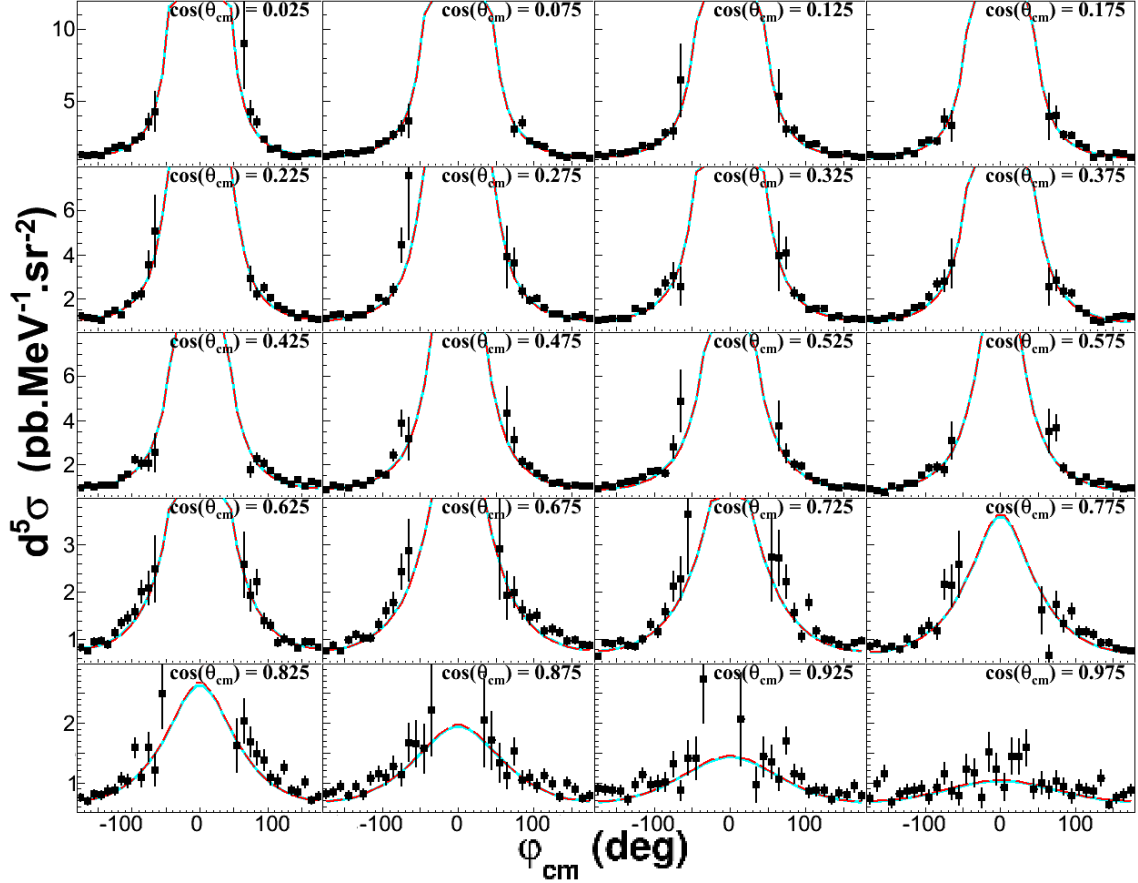
Figure 5.7: Setting LOW: measured $ep \rightarrow ep\gamma$ cross section at fixed $q'_{cm} = 37.5\ MeV/c$ with respect to φ_{cm} for the second-half of $cos(\theta_{cm})$-bins. The curves follow the convention of figure 5.6.

be differentiated at such a small q'_{cm}. The symmetry of the cross section in φ_{cm} is reproduced, which proves that the vertical misalignment is successfully corrected.

The cross sections for the three other q'_{cm} bins ($q'_{cm} = 12.5\ /\ 62.5\ /\ 87.5\ MeV/c$) are not presented but are also in agreement with the theory, and so are the cross-section points from the setting LOW-bis.

Figure 5.8 presents the measured cross section from the setting INP at fixed $q'_{cm} = 112.5\ MeV/c$. When $|\varphi_{cm}| \rightarrow 0$ the measured points tend to lie between the theoretical curves with and without a GP effect. This may already indicate the importance of higher orders in the theoretical curve (BH+B+GPs) which is built thanks to the LEX formalism (a similar observation was done in figure 4.24). This kind of observations motivated us to carefully handle the higher orders in our LEX extraction (see section 5.5.2).

When $|\varphi_{cm}|$ is far from 0 it is hard to distinguish which curve among (BH+B) and (BH+B + GPs) is more faithful to the data. The GPs, especially $\beta_M(Q^2)$ for this setting, have to be extracted from the small differences observed, this illustrates the difficulty of the analysis.

Finally figures 5.9 and 5.10 gather the cross section data from the OOP setting. These points are more sensitive to $\alpha_E(Q^2)$ but again the GP effect is hard to

Figure 5.8: Setting INP: measured $ep \rightarrow ep\gamma$ cross section at fixed $q'_{cm} = 112.5 \ MeV/c$ with respect to φ_{cm} for all the $cos(\theta_{cm})$-bins. The curves follow the convention of figure 5.6.

observe directly.

5.4 Renormalization procedure

The cross sections presented in the previous section may suffer from a global normalization factor. It could be caused by different sources, for example:

- a global loss of events due to detectors inefficiencies not fully corrected.

- a miscalculation of the experimental luminosity. Errors may come from approximation on the target length (due to its shape), target density or residual biases in the deadtime correction.

- a bad estimation of radiative corrections; as stated in section 5.2, they suffer from a lack of theoretical knowledge and the calculation has an uncertainty of 1-2%.

So we need to apply a correction factor, F^{norm}, in order to compensate for all possible biases that act as a global factor:
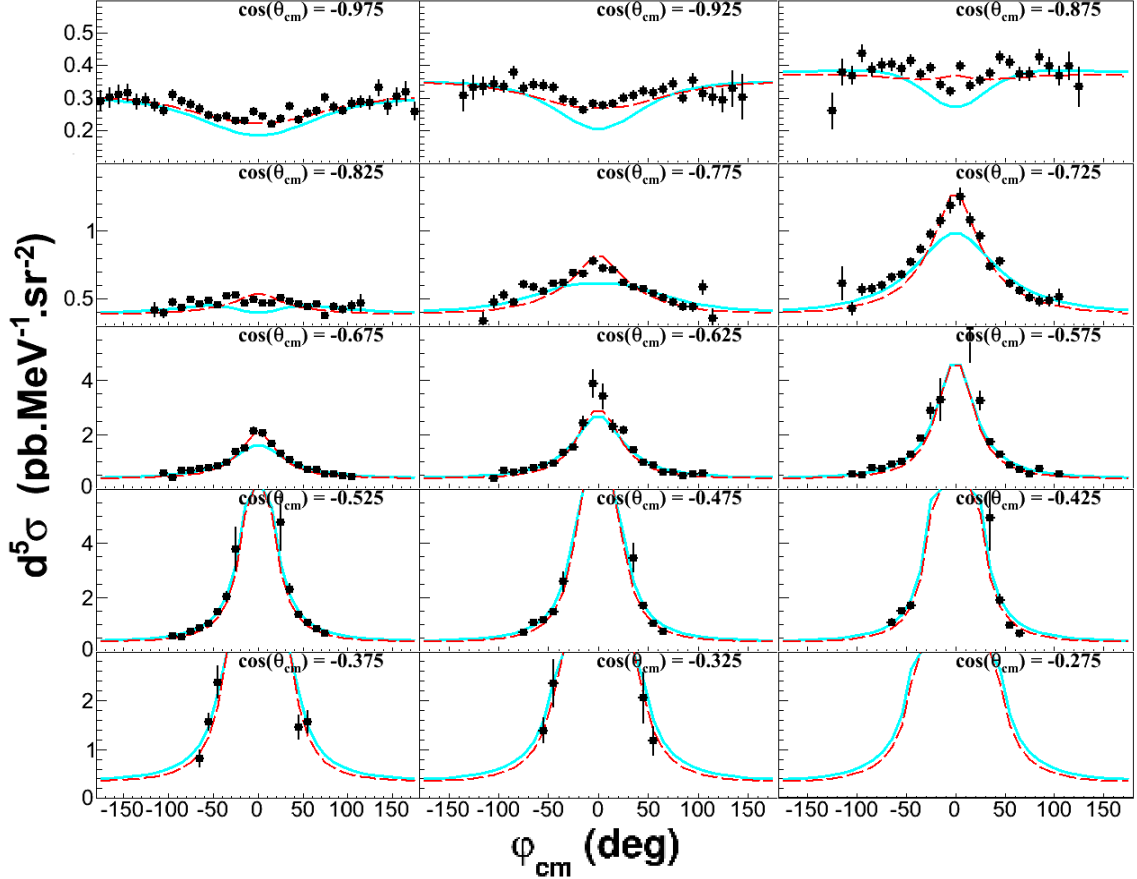
$$\sigma_i^{exp} = \sigma_i^{measured} * F^{norm}, \tag{5.14}$$

Figure 5.9: Setting OOP: measured $ep \rightarrow ep\gamma$ cross section at fixed $q'_{cm} = 112.5 \ MeV/c$ with respect to φ_{cm} for the first-half of $cos(\theta_{cm})$-bins. The curves follow the convention of figure 5.6.

where $\sigma^{measured} = \sigma^{raw} * F^{rad}$.

The F^{norm} factor can be estimated thanks to the low-energy settings (LOW and LOW-bis). Indeed at low q'_{cm}, i.e. $q'_{cm} < 50 MeV/c$ the measured cross section depends only weakly on the GP effect, and so, we can normalize it to the theoretical cross section without including a too important unknown parameter.

An important point is that the renormalization procedure is possible only at low q'_{cm} (<50 MeV/c). At higher q'_{cm} the effects of normalization and polarizabilities are mixed together and cannot be disentangled.

Another important point is that, when we allow σ^{exp} to be renormalized, the LEX and DR fits are sensitive only to the shape of the cross section versus $(q'_{cm}, cos(\theta_{cm}), \varphi_{cm})$ without being disturbed by the absolute normalization.

Using the low-energy settings we identify F^{norm} thanks to a χ^2-minimization:

$$\chi^2_{norm} = \sum_{i=1}^{n} \left(\frac{\sigma_i^{measured} * F^{norm} - \sigma_i^{th}}{\Delta\sigma_i^{measured}(stat) * F^{norm}} \right)^2, \quad (5.15)$$

where F^{norm} is the free parameter of the minimization, $(i = 1 \rightarrow n)$ refers to bins at low q'_{cm}. Several features arise from the calculation.
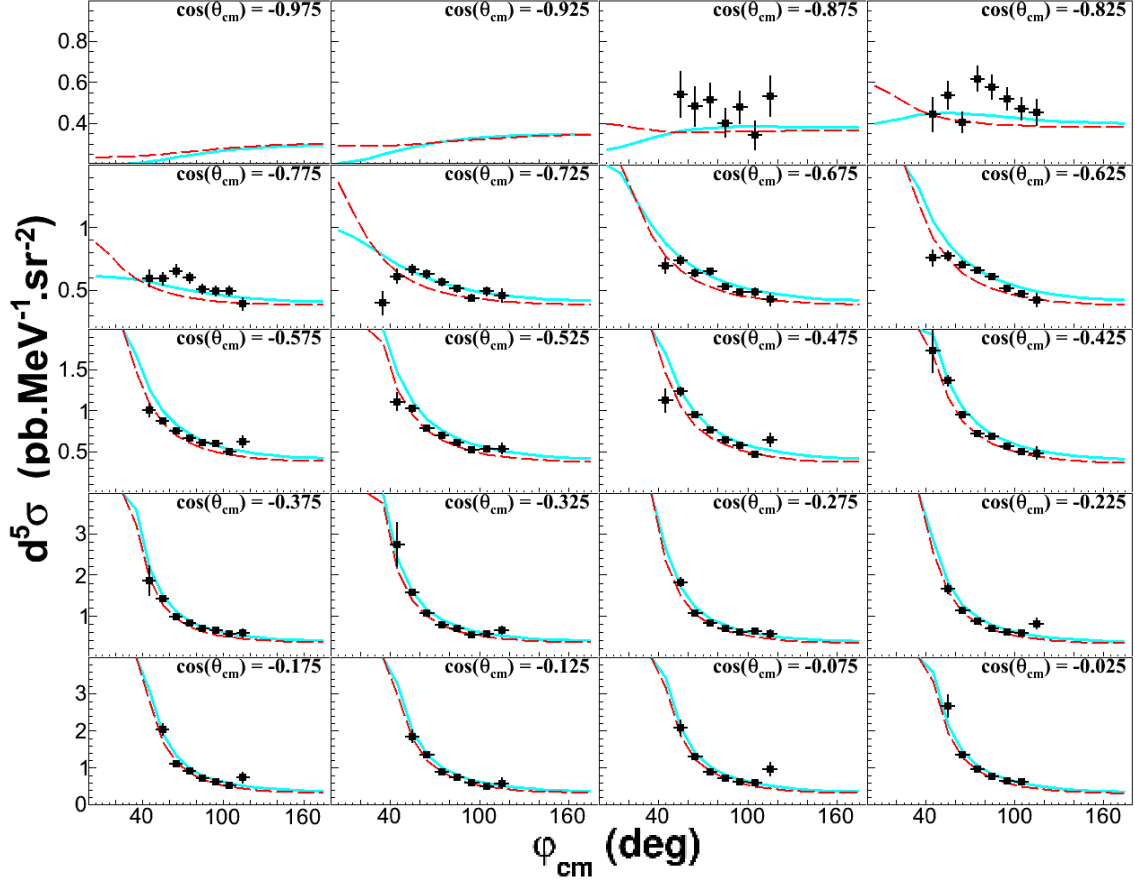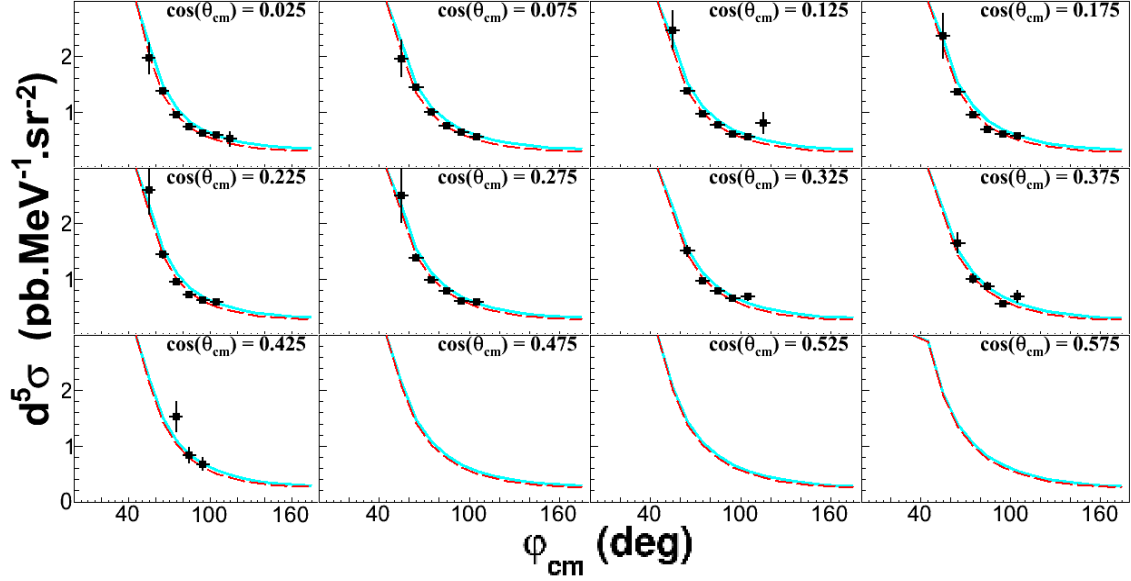
Figure 5.10: Setting OOP: measured $ep \rightarrow ep\gamma$ cross section at fixed $q'_{cm} = 112.5 \ MeV/c$ with respect to φ_{cm} for the second-half of $cos(\theta_{cm})$-bins. The curves follow the convention of figure 5.6.

Firstly, the theoretical cross-section σ_i^{th} has to be as close as possible to the reality, and so, it must include a theoretical GP effect even if it is small at small q'_{cm}. This effect will be calculated thanks to the LEX, following equation 1.38. It will depend on input values of the structure functions $P_{LL} - P_{TT}/\epsilon$ and P_{LT}. Typically the GP effect is of the order of 0.5% and 1.5% of the total cross-section at respectively $q'_{cm} = 12.5 \ MeV/c$ and $q'_{cm} = 37.5 \ MeV/c$. In section 5.4.1 we will present an iterative process that takes care of this dependency.

The second feature concerns the consistency between settings. The data at $Q^2 = 0.2 \ GeV^2$ were all collected in the same conditions and the settings were calibrated by following the same principles. So the need of a renormalization should be identical for all settings. This is checked further for our settings LOW and LOW-bis in section 5.4.2.

The last feature is less straightforward. The theoretical cross section depends on a chosen parametrization of form factors. As stated in section 1.1.2, significant differences exist from a parametrization to another. Actually, the renormalization factor determined by formula 5.15 will depend on the parametrization chosen in σ_i^{th}. We consider three renormalization factors corresponding to three specific form-factor parametrizations:

- F_{FW}^{norm} for the parametrization from J.Friedrich and T.Walcher [17].
- F_B^{norm} for the parametrization from J. C. Bernauer et al. [19].
- F_A^{norm} for the parametrization from J. Arrington et al. [18].

Consequently the renormalized cross section is also form-factor dependent (for instance $\sigma_{FW}^{exp} = \sigma^{measured} * F_{FW}^{norm}$). When no index is specified the quantities refer to our nominal choice, i.e. the parametrization from J.Friedrich and T.Walcher. In section 5.4.3 we will see how the form-factor dependency is exploited positively in our analysis.

5.4.1 The iterative procedure in the LEX analysis

The iterative procedure is the way to take into account the GP-effect dependency from σ^{th} in the estimation of F^{norm}. It consists in extracting the structure functions by the LEX analysis (presented section 5.5) and using the result to compute a new theoretical cross section.

Figure 5.11 is a schematic representation of the iterative procedure. It starts by the χ^2 minimization of F^{norm} with any initial choice of theoretical cross section. The obtained F_0^{norm} is then used to renormalize the measured cross section (equation 5.14). Afterwards these experimental cross sections are used in a LEX fit to extract the structure functions which will be used to compute a new theoretical cross section. This last one is then used for a second determination of the renormalization factor F_1^{norm}, and the procedure continues.

The iterative process stops when the difference $F_{n-1}^{norm} - F_n^{norm} = \pm 0.002$, which is the statistical precision on F^{norm} (deduced from the points corresponding to $\chi^2_{norm} + 1$). Obviously the iterative process has to be done keeping the form-factor parametrization fixed, and the bins selection fixed.
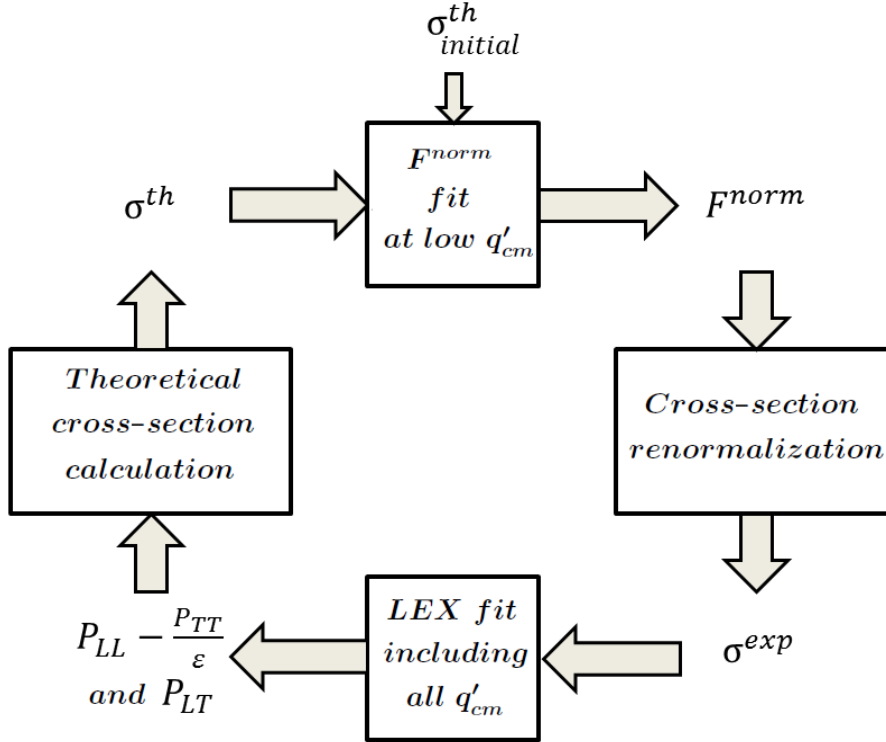
Figure 5.11: Schematic representation of the iterative procedure. The fit of F^{norm} is described by equation 5.15, the LEX fit itself is described in section 5.5 and the theoretical cross section is calculated thanks to equation 1.38.

The initial choice of the theoretical cross section has no impact, the results fully converge after a few iterations. As an illustration figure 5.12 represents the procedure behavior for three different initial starting points: the red points show the steps if one considers no GP effect in the first place, the blue points are for a so-called "absurd" choice of GP effect with $P_{LL} - P_{TT}/\epsilon = 40 \ GeV^{-2}$ and

$P_{LT} = 2 \ GeV^{-2}$ (which is far from our final result). The black cross is obtained with $P_{LL} - P_{TT}/\epsilon = 19.5 \ GeV^{-2}$ and $P_{LT} = -4.0 \ GeV^{-2}$ which are values close to our final result, a so-called "coherent" choice. The renormalization factor F^{norm} at each step is also indicated in this figure.

Figure 5.12: Illustration of three iterative processes. Each point is the structure-function extraction (with statistical errors) obtained from the cross section renormalized by the indicated value of F^{norm}. The colors stand for different starting points of the iterative process as explained in the text. Here all procedures converge to the point $P_{LL} - P_{TT}/\epsilon = 19 \ GeV^{-2}$, $P_{LT} = -3.7 \ GeV^{-2}$ and $F^{norm} = 0.980$.
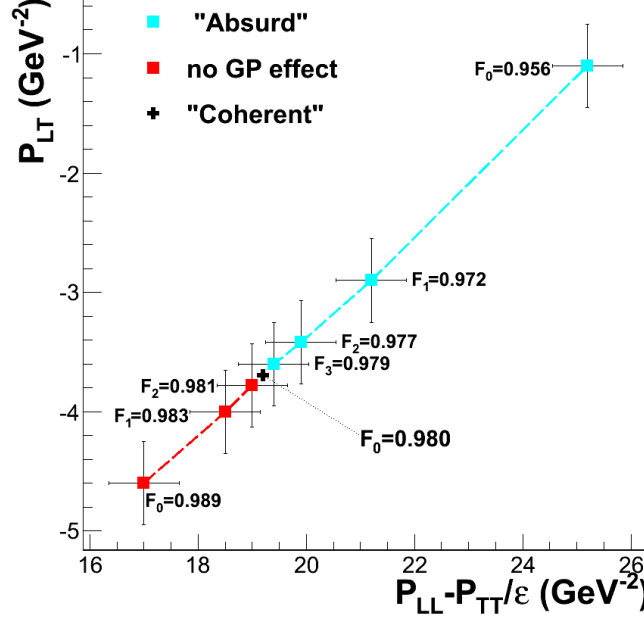
As a check, we tried very different LEX extractions of structure functions (with and without the bins selection described in section 5.5) and we found that it weakly impacts the convergence point of the interations in terms of F^{norm}: $\Delta F^{norm} = \pm 0.002$.

So the iterative procedure is necessary to get the best determination of F^{norm}. However, some VCS experiments did not apply any renormalization, for example because of lack of low-q'_{cm} data [68].

5.4.2 The agreement between settings and between q'_{cm}-bins

In this section we present the consequence on the F^{norm} determination if one considers different groups of data (various settings and bins) in the minimization of χ^2_{norm}. The results presented here are obtained with the Friedrich-Walcher parametrization of form factors. An iterative procedure has been performed and only the final values of F^{norm} are shown. To test the different data groups we can choose between two low-energy settings (LOW and LOW-bis) and each one of

them contains two sets of ≈ 700 low-q'_{cm} bins: one set at $q'_{cm} = 12.5 \; MeV/c$ and the other at $q'_{cm} = 37.5 \; MeV/c$.

Table 5.4.2 gathers the results. The six first lines show an excellent agreement, giving an average value of $F^{norm} = 0.979$.

Bin(s)	Setting(s)	F^{norm}
0+1	LOW+LOW-bis	0.983
0+1	LOW	0.983
0+1	LOW-bis	0.985
*1	**LOW+LOW-bis**	**0.980**
1	LOW	0.985
1	LOW-bis	0.973
0	LOW+LOW-bis	0.997
0	LOW	0.95
0	LOW-bis	1.06

Table 5.4.2: F^{norm} results after iterative process for several combinations of selected bins and settings; "0" stands for the bin at $q'_{cm} = 12.5 \; MeV/c$, "1" is for $q'_{cm} = 37.5 \; MeV/c$ and "0+1" means that the two bins are considered. The statistical error on F^{norm} is ± 0.002.

The data from settings LOW and LOW-bis were calibrated independently. The observed good agreement comforts us in the quality of our calibration principles.

The three last lines of the table illustrate the consequence of selecting bins at the edge of spectrometers acceptance. Indeed the calibration is optimized for the bins at the center of the spectrometers acceptance, i.e. at $q'_{cm} = 37.5 \; MeV/c$ for setting LOW and LOW-bis and at $q'_{cm} = 87.5 \; MeV/c$ and $q'_{cm} = 112.5 \; MeV/c$ for the others. Only data from $q'_{cm} = 37.5 \; MeV/c$-bins were considered for the determination of our final renormalization factor (the starred line in table 5.4.2).

Finally we estimated that the renormalization factor is determined to ± 0.006, corresponding to the maximal spread among the six first lines of table 5.4.2.

5.4.3 Canceling the form-factor dependency in the LEX extraction

Let's now consider several iterative procedures performed with different form-factor parametrizations of σ_i^{th} in equation 5.15. They will inevitably result in different values of F^{norm}.

Table 5.4.3 presents the different F^{norm} obtained for three choices of form-factor parametrizations.

Form-factor parametrization	Friedrich-Walcher [17]	Arrington et al. [18]	Bernauer et al. [19]
F^{norm}	$F_{FW}^{norm} = 0.980$	$F_A^{norm} = 0.969$	$F_B^{norm} = 0.993$

Table 5.4.3: F^{norm} results after different iterative processes, all using $q'_{cm} = 37.5 \; MeV/c$-data but considering different form-factor parametrizations.

Consequently the renormalized cross section will differ from a parametrization to another and so we have three sets of experimental cross section:

$$\sigma_{FW}^{exp} \ / \ \sigma_{A}^{exp} \ / \ \sigma_{B}^{exp}.$$

A priori, the form-factor dependency of the renormalized experimental cross-section appears to be a problem, but, it is actually a strength of the LEX extraction of structure functions.

Indeed the LEX extraction (presented in section 5.5) consists in computing the difference between the renormalized cross section and a theoretical one, and the two are form-factor dependent ($\sigma_{Form-Factors}^{exp}$ and $\sigma_{Form-Factors}^{th}$).

As will be shown below, changing the form-factor parametrization in the (BH+B) cross section roughly rescales it by a global factor. Therefore the LEX fit can adapt itself to such a change if we allow also the experimental cross section to be changed by a global factor. This is the guiding principle of our renormalization procedure.

Influence of form-factor parametrization on the (BH+B) cross section

We computed the following ratio of theoretical BH+B cross-sections in each analysis bin (i):

$$R_i^{A/B} = \frac{\sigma_A^{BH+B}}{\sigma_B^{BH+B}} \quad . \tag{5.16}$$

The index 'A' still refers to the form-factor parametrization from Arrington et al. [18], and 'B' to the one from Bernauer et al. [19]. Figures 5.13 and 5.14 show the ratio for the bins at respectively $q'_{cm} = 37.5 \ MeV/c$ and $q'_{cm} = 112.5 \ MeV/c$. The observed variations are small, i.e. $0.974 < R^{A/B} < 0.982$. So changing the form-factor paramerization does act like a global rescaling of the theoretical cross section, to better than 1% at $q'_{cm} = 112.5 \ MeV/c$, and to better than 0.4% at $q'_{cm} = 37.5 \ MeV/c$.

Conclusion on the renormalization procedure

form-factor parametrizations	Structure functions (GeV^{-2})	LEX extraction before renormalization	F^{norm}	LEX extraction after renormalization
J.Arrington et al. [18]	$P_{LL} - P_{TT}/\epsilon$ P_{LT}	11.7 -6.51	$F_A^{norm} = 0.969$	19.3 -3.3
J.Friedrich T.Walcher [17]	$P_{LL} - P_{TT}/\epsilon$ P_{LT}	14.2 -5.9	$F_{FW}^{norm} = 0.980$	19.3 -3.7
J.Bernauer et al. [19]	$P_{LL} - P_{TT}/\epsilon$ P_{LT}	17.9 -4.3	$F_B^{norm} = 0.993$	19.7 -3.5

Table 5.4.3-c: LEX extraction of structure functions before renormalization ($F^{norm} = 1$) and after ($F^{norm} = F_{form-factor}^{norm}$) for the three selected parametrizations of form factors. For every extraction the statistical errors are $\Delta P_{LL} - P_{TT}/\epsilon = \pm 0.64 \ (GeV^{-2})$ and $\Delta P_{LT} = \pm 0.34 \ (GeV^{-2})$.

Figure 5.13: The ratio $R^{A/B}$ of two theoretical BH+B cross-sections in the $(cos(\theta_{cm}), \varphi_{cm})$-plane at $q'_{cm} = 37.5 \ MeV/c$.
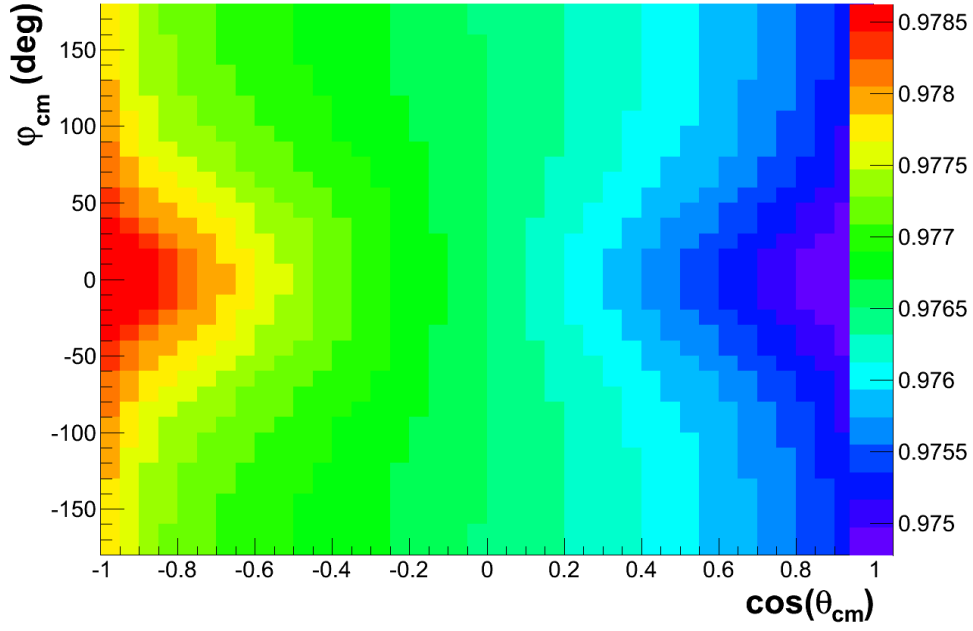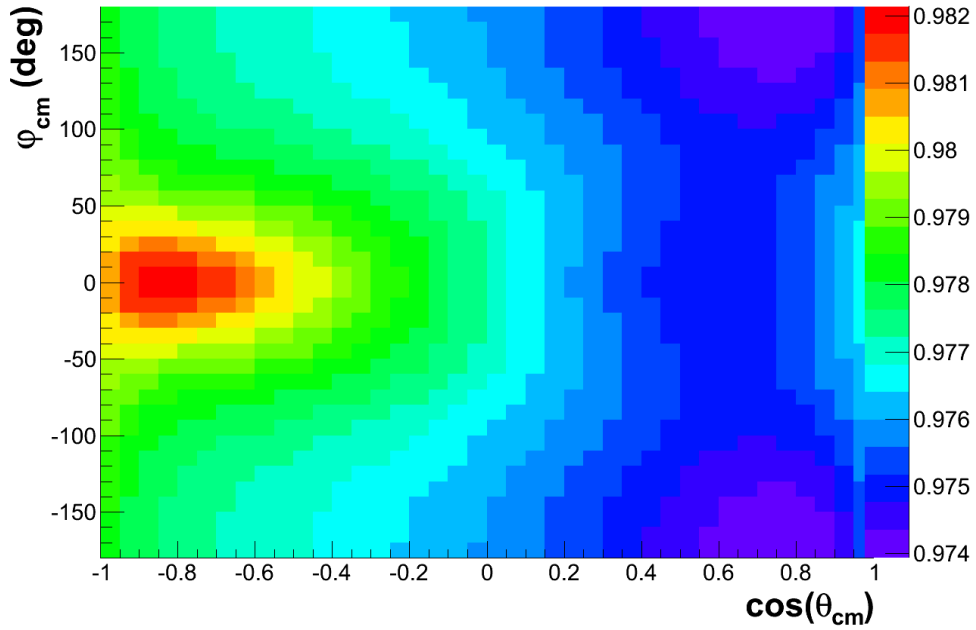

Figure 5.14: The ratio $R^{A/B}$ of two theoretical BH+B cross-sections in the $(cos(\theta_{cm}), \varphi_{cm})$-plane at $q'_{cm} = 112.5 \ MeV/c$.

As a most conclusive test, we realized a LEX extraction with the three different form-factor parametrizations. Table 5.4.3-c shows the structure function extraction

for these three different choices, obtained before and after the renormalization.

With $F^{norm} = 1$, there is no iterative process to do, and the structure functions obtained by the LEX fit are clearly not in agreement within their statistical error bar. After having done the iterative process, leading to the F^{norm} given in the table, the extracted structure functions come to very close agreement. This definitively proves the form-factor independency of our analysis and the need of a renormalization process.

Finally, the extraction presented in the following sections is done with cross-sections renormalized by:

$$F^{norm}_{FW} = 0.980 \pm 0.002_{stat} \pm 0.006_{syst} \pm 0.002_{syst},$$

with the first systematic error which is due to acceptance features and the second one which is a consequence of the use of different conditions for the LEX fit in the iterative procedure which allows to determine F^{norm}.

5.5 The LEX fit

The LEX extraction of structure functions is based on equation 1.38 and consists first to determine (in each analysis bin) the quantity ΔM related to the difference between the experimental cross section and the BH+B one:

$$
\begin{aligned}
\Delta M \quad &= \frac{\sigma^{exp} - \sigma^{BH+B}}{\Phi q'_{cm}} \\
&= [v_{LL}(P_{LL}(q_{cm}) - \frac{P_{TT}(q_{cm})}{\epsilon}) + v_{LT}P_{LT}(q_{cm})] + O(q'^{2}_{cm}),
\end{aligned}
\tag{5.17}
$$

where σ^{exp} is renormalized with the same form-factor parametrization that is used to compute σ^{BH+B}. One defines Ψ_0 as the term independent of q'_{cm}:

$$\Psi_0 = \Delta M(q'_{cm} \to 0) = [v_{LL}(P_{LL} - \frac{P_{TT}}{\epsilon}) + v_{LT}P_{LT}]. \tag{5.18}$$

If $O(q'^{2}_{cm})$ is small enough, ΔM should be independent of q'_{cm}. The q'_{cm}-independency of ΔM can be checked for fixed values of θ_{cm} and φ_{cm} by plotting the experimental ΔM term as a function of q'_{cm} at fixed angles $(\theta_{cm}, \varphi_{cm})$. In appendix D, figure D.1 shows this behavior for selected angular bins. In the ideal case of negligible higher orders our ΔM measurements at fixed $(cos(\theta_{cm}), \varphi_{cm})$ but different q'_{cm} are just several measurements of the same Ψ^{exp}_0. Ψ^{exp}_0 is then deduced by averaging the ΔM terms in a $(cos(\theta_{cm}), \varphi_{cm})$-bin over the q'_{cm} values.

Thereafter, equation 5.18 can be rewritten as:

$$\frac{\Psi_0}{v_{LT}} = \frac{v_{LL}}{v_{LT}}(P_{LL} - \frac{P_{TT}}{\epsilon}) + P_{LT}, \tag{5.19}$$

and so the structure functions are simply the slope and intercept of a linear function that can be determined by a χ^2-minimization:

$$\chi^2_{LEX} = \sum_{i=1}^{n} \left(\frac{\Psi_0^{exp}/v_{LT} - \Psi_0^{th}/v_{LT}}{\Delta(\Psi_0^{exp}/v_{LT})(stat)} \right)^2, \tag{5.20}$$

with Ψ_0^{th}/v_{LT} calculated by equation 5.19 where the structure functions are the free parameters of the fit. Figure 5.15 shows the LEX fit of structure functions, the points (Ψ_0^{exp}/v_{LT}) are fitted with a minimum reduced χ^2 of 1.26 for $n.d.f = 944$.
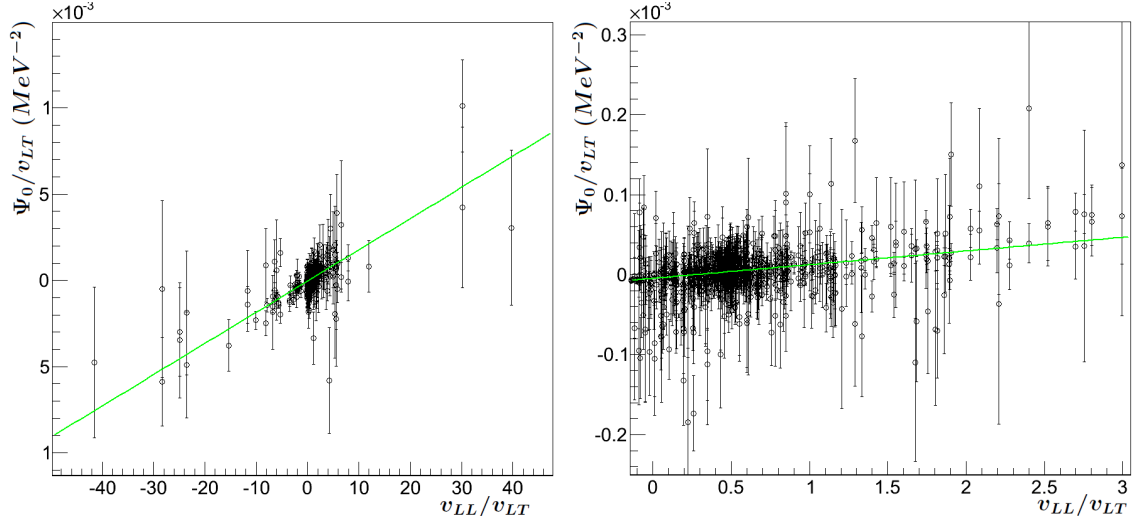

Figure 5.15: Ψ_0^{exp}/v_{LT} with respect to v_{LL}/v_{LT} for the $(cos(\theta_{cm}), \varphi_{cm})$ bins from all settings contributing to the LEX fit. The right figure is obtained after applying a zoom. The green line is the final result of our LEX fit which has $P_{LL} - P_{TT}/\epsilon = 18.10\ GeV^{-2}$ as a slope and $P_{LT} = -3.59\ GeV^{-2}$ as intercept.

It is also possible to extract the structure functions by a more direct fit of the renormalized experimental cross section:

$$\chi^2_{LEX,2} = \sum_{i=1}^{n} \left(\frac{\sigma^{exp} - \sigma^{th}}{\Delta\sigma^{exp}(stat)} \right)^2, \tag{5.21}$$

with σ^{th} the cross-section calculated according to equation 1.38 (with $O(q'^2_{cm}) = 0$) and the structure functions as free parameters of the fit. To minimize χ^2_{LEX} or $\chi^2_{LEX,2}$ leads strictly to the same structure-functions result since both fits are based on the same assumption.

In the following sections we will discuss the bin selections and their impact on the LEX fit.

5.5.1 Bin selection: "gradient cut"

The gradient selection is designed in order to remove the Bethe-Heitler peaks from the analysis. Even if our data are out of this region it is still interesting to build the cut for two reasons. First, this selection was also used to identify where the

radiative corrections can be averaged. Secondly the bins removed by this cut are at the acceptance edges, i.e. where experimental uncertainties are larger.

The selection is detailed in appendix E. It consists in a threshold cut on the cross-section variation from a bin to its neighbour. It is essentially designed that way in order to be close to our acceptance edges as presented in figure E.1. The use of the gradient selection is not essential to the LEX fit and its omission is accounted in the systematic error budget on structure functions (see section 5.7).

The impact of this cut is positive in that it improves the minimum χ^2 of the LEX fit. Also, although this cut removes 20% of the analysis bins, it has only a small impact on the final statistical errors. It increases the errors by 3% and 6% for P_{LT} and $P_{LL} - P_{TT}/\epsilon$ respectively.

5.5.2 Bin selection: "mask selection"

The LEX extraction requires that the higher orders $O(q'_{cm}{}^2)$ are negligible, but this is not true in the whole phase space. The first warning of the importance of higher orders was given by the Bates LEX analysis as discussed in section 2.3.3.

In order to identify where the higher-order terms are small enough to be neglected, we designed a cut based on the DR model, the so-called "mask selection".

The selection uses the estimation of higher orders discussed in section 3.3.3. As a reminder, we have defined $\mathcal{O}^{DR}(q'_{cm}{}^2)$ as the criterion representing the relative importance of higher-order terms in the LEX expansion according to the DR model. Now we consider the following cut:

$$\mathcal{O}^{DR}(q'_{cm}{}^2) = \frac{|\sigma^{LEX} - \sigma^{DR}| * 100}{\sigma^{BH+B}} < K_{thr}, \qquad (5.22)$$

with the cross sections σ^{LEX} and σ^{DR} being purely theoretical and calculated with the same input values of the structure functions. In first approximation K_{thr} may vary from 1-2% to 5-6%. The lower limit is fixed by the magnitude of the systematic error on σ^{exp}. The upper limit is given by the maximum value that $\mathcal{O}^{DR}(q'_{cm}{}^2)$ can reach, presented in figure 3.13.

Figure 5.16 shows the angular bins that satisfy the selection with the following input value of structure functions in equation 5.22 $P_{LL} - P_{TT}/\epsilon = 17.9$ (GeV^{-2}) and $P_{LT} = -3.7$ (GeV^{-2}) and with $K_{thr} = 2.5\%$. Since at low q'_{cm} the GP effect is small equation 5.22 simply comes to comparing the BH+B cross section with itself and removes no bins. At $q'_{cm} = 112.5$ MeV/c the selection becomes very restrictive but we believe this is a necessity if one wants to get rid of higher-orders effect.

Figure 5.17 shows the effect of this selection on the analysis for the $q'_{cm} = 112.5$ MeV/c-bins. Cross sections are measured in every bin (red and blue) on this plot but only the blue ones are kept for the LEX analysis. Three regions corresponding to the three high-q'_{cm} settings are also shown.

This mask selection induces two dependencies that need to be controlled. Firstly, we have to see the effect induced by K_{thr} variations. Secondly the theoretical cross-sections σ^{DR} and σ^{LEX} depend on input values of structure functions and we have to study the impact of changing them within a reasonable range.
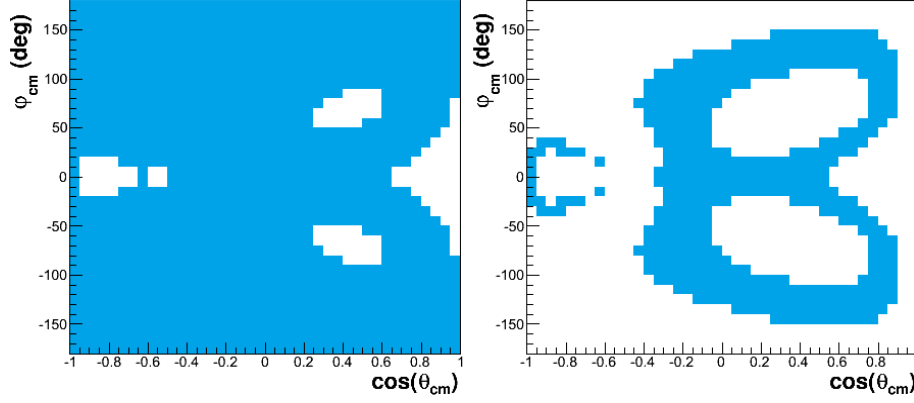
Figure 5.16: Bins (in blue) that satisfy the mask selection in the $(\varphi_{cm}, cos(\theta_{cm}))$-plane when $K_{thr} = 2.5\%$, $P_{LL} - P_{TT}/\epsilon = 17.9\ (GeV^{-2})$ and $P_{LT} = -3.7\ (GeV^{-2})$ at $q'_{cm} = 87.5\ MeV/c$ (left) and $q'_{cm} = 112.5\ MeV/c$ (right).
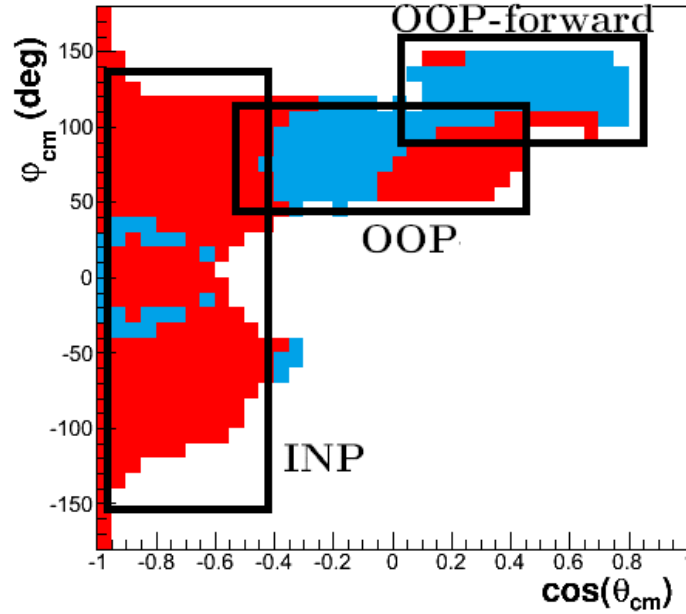
Figure 5.17: Bins, in blue, that satisfy the mask selection in the $(\varphi_{cm}, cos(\theta_{cm}))$-plane at $q'_{cm} = 112.5\ MeV/c$. The bins in red contain data that are rejected by this selection.

The K_{thr} dependency

We tested for a given GP effect ($P_{LL} - P_{TT}/\epsilon = 17.9\ (GeV^{-2})$ and $P_{LT} = -3.7\ (GeV^{-2})$) the consequences on the LEX extraction if one changes the value of the K_{thr} criterion. This is represented in figure 5.18. Two regions arise, one which is unstable for a restrictive $K_{thr} < 2\%$ (especially for P_{LT}) and the second, more stable, for K_{thr} in the range $[2;5]\%$.

The red points are obtained when no mask selection is applied, i.e. $K_{thr} = \infty$. It appears that removing this selection has no effect on P_{LT} but has an important effect on $P_{LL} - P_{TT}/\epsilon$. We observed the same behavior with other structure-

function choices to build the mask criterion.

Figure 5.18: LEX extraction of structure functions with respect to the K_{thr} criterion for input structure functions respectively fixed to $P_{LL} - P_{TT}/\epsilon = 17.9 \ GeV^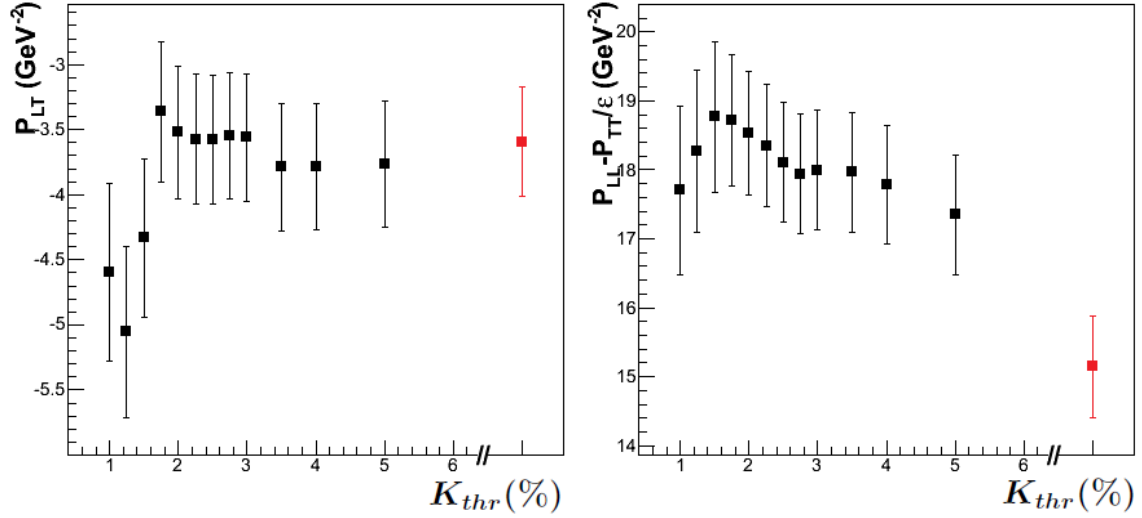{-2}$ and $P_{LT} = -3.7 \ GeV^{-2}$ to build the mask. The red points are obtained when no mask selection is applied. The error bars are statistical.

We finally choose $K_{thr} = 2.5\%$ as a nominal cut.

Theoretical structure functions dependency

We tested the impact of changing the theoretical structure functions when building the mask selection. We started from a given value and made the structure functions vary independently over a large range. Table 5.5.2 gathers the results.

Structure functions	Theoretical inputs	Extracted result
$P_{LL} - P_{TT}/\epsilon \ (GeV^{-2})$	No mask	15.14 ± 0.42
$P_{LT} \ (GeV^{-2})$	selection	-3.60 ± 0.21
$P_{LL} - P_{TT}/\epsilon \ (GeV^{-2})$	22.5	18.47 ± 0.56
$P_{LT} \ (GeV^{-2})$	-2.3	-3.47 ± 0.30
$P_{LL} - P_{TT}/\epsilon \ (GeV^{-2})$	28.2	19.37 ± 0.62
$P_{LT} \ (GeV^{-2})$	-2.3	-3.84 ± 0.33
$P_{LL} - P_{TT}/\epsilon \ (GeV^{-2})$	13.5	17.46 ± 0.53
$P_{LT} \ (GeV^{-2})$	-2.3	-3.07 ± 0.30
$P_{LL} - P_{TT}/\epsilon \ (GeV^{-2})$	22.5	18.91 ± 0.61
$P_{LT} \ (GeV^{-2})$	-5.4	-3.91 ± 0.34
$P_{LL} - P_{TT}/\epsilon \ (GeV^{-2})$	22.5	18.16 ± 0.57
$P_{LT} \ (GeV^{-2})$	-0.5	-3.00 ± 0.32

Table 5.5.2: LEX extraction of structure functions with various theoretical inputs to build the mask selection, and fixing $K_{thr} = 2.5\%$ (except in the first case). The error bars of the extracted results are statistical.

110

Applying a mask selection has an important impact on the extracted structure functions, at least for $P_{LL} - P_{TT}/\epsilon$. Globally, any of the mask selections of table 5.5.2 gives results in agreement within $\pm 1\ GeV^{-2}$ for $P_{LL} - P_{TT}/\epsilon$ and $\pm 0.5\ GeV^{-2}$ for P_{LT}.

To remove this last uncertainty we used another iterative procedure. The structure functions extracted by the LEX are used to build a new mask selection, which is used to redo the LEX fit, and so on. The iterations are performed at constant K_{thr}.

Similar to the iterative procedure relative to the renormalization process, we tested two starting points. Firstly, we used as input the structure functions obtained when no mask selection is applied (line 1 of table 5.5.2). Secondly, we tried to iterate starting from the second line of the table.

The results converge to the following input values of structure functions for the mask selection:

$$P_{LL} - P_{TT}/\epsilon(MASK) = 17.9\ (GeV^{-2})$$
$$P_{LT}(MASK) = -3.7\ (GeV^{-2})$$

which also coincide with the outputs of the LEX fit.

5.5.3 Conclusion

Once one trusts the data calibration and the cross-section renormalization, the main feature of the LEX analysis concerns the handling of higher orders in q'_{cm}.

To this aim, we decided to use a mask selection based on the DR model, even if by doing so we lose a small part of the model-independency of the LEX analysis.

In our experiment we also have a direct hint of higher-order terms at an early level: we observed during the data analysis that some experimental distributions do not follow the simulated ones when we include a GP effect in the weight of simulated events; this is case namely for the φ_{cm}-distribution (cf. figure 4.24). This discrepancy was due to the theoretical GP effect which is badly estimated by the LET and so our data needed to be carefully handled.

LEX extractions can be done by considering different subgroups of settings and bins, and will provide various results. We believe that the best fit is the one which gathers all data in order to increase the sensitivity to the two structure functions, and to increases the lever arm in the v_{LL} and v_{LT} coefficients. In appendix D.2 the consequences of considering subgroups of data are shown.

Nominal LEX results

Finally we performed the nominal analysis thanks to 946 Ψ_0 data points as presented in table 5.5.3.

Settings	LOW and LOW-bis	INP, OOP and OOP-forward
Number of q'_{cm}-bins used	3	3
q'_{cm}-range (MeV/c)	[0;75]	[50;125]

Table 5.5.3: Data used for the final LEX fit. As a reminder, the q'_{cm} values have to be below the pion production threshold.

We found a satisfying reduced χ^2, i.e. 1.26 for n.d.f=944 and the extracted structure functions are[3]:

$$
\begin{aligned}
P_{LL} - P_{TT}/\epsilon \ &= 18.10 \pm 0.56_{stat} \ (GeV^{-2}) \\
P_{LT} \ &= -3.59 \pm 0.31_{stat} \ (GeV^{-2}).
\end{aligned}
\tag{5.23}
$$

Figure 5.19 shows the χ^2_{LEX} variations in the $(P_{LL} - P_{TT}/\epsilon, P_{LT})$-plane. The elliptic shape is due to the linearity of the problem. A small correlation is observed between the two structure-function errors. The inner red ellipse expresses the standard deviation of each structure function separately, these are the errors mentioned in equation 5.23. The outer red ellipse expresses the standard deviation of both structure functions simultaneously [98].
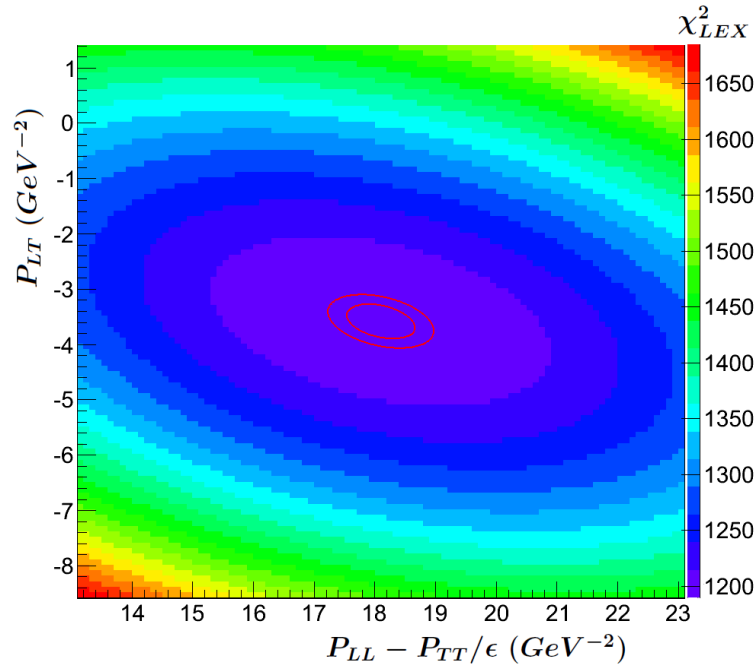
Figure 5.19: χ^2_{LEX} variations in the $(P_{LL} - P_{TT}/\epsilon, P_{LT})$-plane. The red ellipses correspond to contours at $\chi^2_{min} + 1$ and $\chi^2_{min} + 2.41$ (where χ^2_{min} is not reduced).

5.5.4 From structure functions to generalized polarizabilities

Once the structure functions are extracted, the LEX analysis is powerless to give individual GP values. So the next step requires the direct intervention of a model to find the electric and magnetic GPs.

---

[3]These results differ slightly from the ones of Table 5.4.3-c (for the Friedrich-Walcher parametrization), because of different inputs to build the mask.

For this purpose we used the DR model. The method simply consists in using the DR code to find the Λ parameters corresponding to our measured values of the LEX structure functions at $Q^2 = 0.2\ GeV^2$, $q_{cm} = 458\ MeV/c$ and $\epsilon = 0.85$. Then the code is used a second time to find the GPs at $Q^2 = 0.2\ GeV^2$.

The procedure will induce a form-factor dependency, but it is small and impacts the results very weakly.

We found:

$$\alpha_E(Q^2 = 0.2\ GeV^2) = 3.90 \pm 0.14_{stat}\ (10^{-4}fm^3)$$
$$\beta_M(Q^2 = 0.2\ GeV^2) = 1.14 \pm 0.15_{stat}\ (10^{-4}fm^3)\ .$$

5.6 The DR analysis

The second extraction of GPs that we have done is directly based on the DR model. It requires again the experimental cross sections, renormalized by the factor $F_{FW}^{norm} = 0.98$ which corresponds to using the Friedrich-Walcher parametrization of proton form factors.

We did not perform a DR fit for three different form-factor parametrizations, as we did for the LEX fit. It would have required a too long computational time. However, we expect that the DR extraction of GPs will be essentially independent of the form-factor choice, since the principles of the fitting method are the same as for the LEX analysis.

5.6.1 Fit description

Contrary to the LEX fit, the DR fit is not analytical, because the theoretical cross-section σ^{DR} depends on the polarizabilities in a very complex manner. We still compare our experimental cross sections to the DR calculation by a χ^2 method, but the minimum has to be found purely numerically.

We first need to compute a large amount of DR cross sections. Indeed, we need the cross sections to be calculated in the 10080 bins of our analysis (10080/2 actually because the theoretical cross section is perfectly φ_{cm}-symmetric) and we also need them to be calculated for different input values of the GPs.

So for the first step, we built a regular grid of 25 values of $\alpha_E(Q^2 = 0.2\ GeV^2)$ times 24 values of $\beta_M(Q^2 = 0.2\ GeV^2)$ in the range allowed by the model, i.e. 600 grid nodes, and we computed the 10080/2 cross sections for each of the 600 grid points. We calculated a total of $3,024,000$ theoretical cross sections, which represents a long computational time.

The χ^2 is then written as:

$$\chi^2_{DR}(\alpha_E(Q^2), \beta_M(Q^2)) = \sum_{i=1}^{\mathcal{N}} \left(\frac{\sigma_{FW}^{exp}(i) - \sigma_{FW}^{DR}(i, \alpha_E(Q^2), \beta_M(Q^2))}{\Delta\sigma_{FW}^{exp}(i)(stat)} \right)^2. \quad (5.24)$$

The 600 χ^2-values show a clear and unique minimum as represented in figure 5.20, and near the minimum, the χ^2 follows a paraboloid shape.
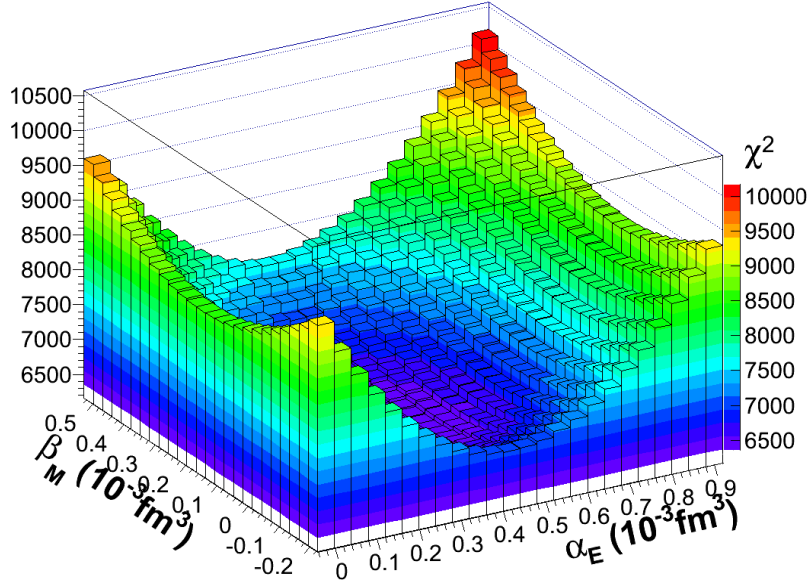
Figure 5.20: χ^2_{DR} of the DR analysis in the 600 $(\alpha_E(Q^2), \beta_M(Q^2))$-bins.

Now we have to identify the minimal χ^2: the value of χ^2_{min} and its precise position in $(\alpha_E(Q^2), \beta_M(Q^2))$ coordinates, which will be the extracted GPs. This is done by fitting the χ^2 to the following paraboloid function:

$$f(x, y) = A(x - B)^2 + C(y - D)^2 + E + F(x - B)(y - D), \qquad (5.25)$$

with A, B, C, D, E and F free parameters of the function and $x = \alpha_E(Q^2)$, $y = \beta_M(Q^2)$. E will be the minimum χ^2, B its position along the x-axis (corresponding to the extracted electric GP) and D its position along the y-axis (corresponding to the extracted magnetic GP). The fitted function also allows to extract the statistical errors on $\alpha_E(Q^2)$ and $\beta_M(Q^2)$ by drawing the contour at $\chi^2_{min} + 1$ [98].

In contrary to the LEX fit that requires supplementary selections, none of them are necessary for the DR fit, which is conceptually much simpler[4]. Each of the 600 χ^2_{DR} was then calculated thanks to 4431 cross-section points[5] distributed in our different settings, as presented in table 5.6.1. Another difference with the LEX fit is that the DR extraction is valid even above the pion production threshold, allowing us to use two more q'_{cm} bins, i.e. bins at $q'_{cm} = 137.5\ MeV/c$ and $q'_{cm} = 162.5\ MeV/c$.

---

[4]the gradient selection was already not mandatory for the LEX fit, for the DR fit its impact is also small in terms of extracted GPs, so we decided to not use it.

[5]we measured 7784 cross sections but some are measured several times by different settings, here the measurements are averaged over settings.

Settings	LOW and LOW-bis	INP, OOP and OOP-forward
Number of q'_{cm}-bins used	4	5
q'_{cm}-range (MeV/c)	[0;100]	[50;175]

Table 5.6.1: Data used for the final DR fit.

Figure 5.21 is a two-dimensional representation of how the paraboloid function fits the χ^2 distribution, the contour at $\chi^2_{min} + 1$ shows the statistical uncertainties on the extracted GPs, the outer black ellipse expresses the standard deviation of both GPs simultaneously. Almost no correlation is observed between the fitted values of $\alpha_E(Q^2)$ and $\beta_M(Q^2)$.
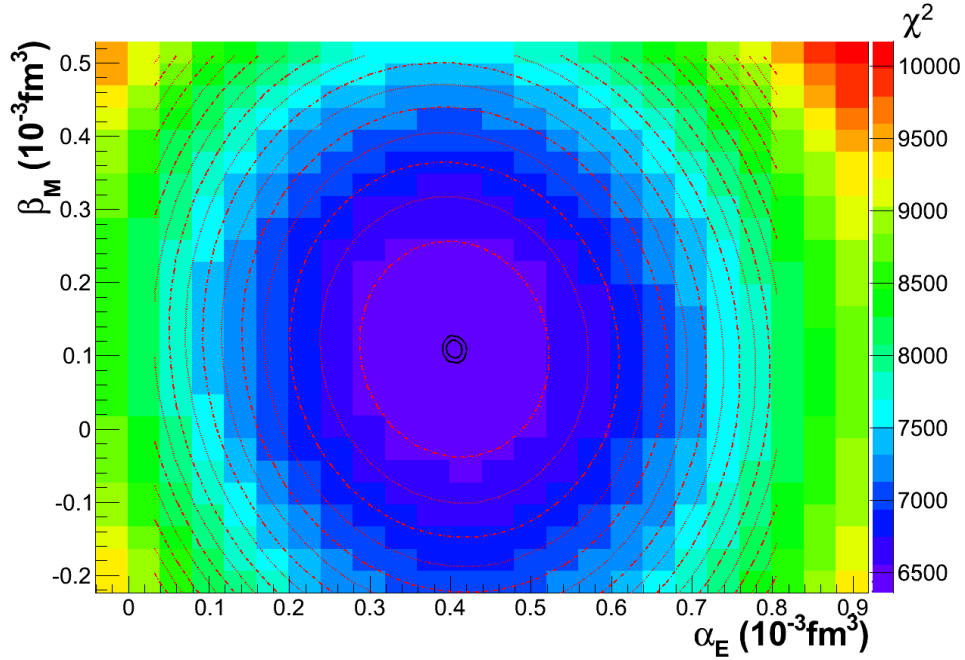
Figure 5.21: Non-reduced χ^2_{DR} in the 600 $(\alpha_E(Q^2), \beta_M(Q^2))$-bins and several fitting-function contours. The two inner black ellipses correspond to the contours at $\chi^2_{min} + 1$ and $\chi^2_{min} + 2.41$.

Once the GPs are extracted we need to use again the DR code to find the corresponding structure functions. By doing that we reintroduce a form-factor dependency, but as in section 5.5.4 it is a very small one.

5.6.2 The results of the DR fit

Finally, we found a reduced χ^2 of 1.43 for $n.d.f = 4429$ and the extracted GPs are:

$$\alpha_E(Q^2) = 4.05 \pm 0.10_{stat} \ (10^{-4}.fm^3)$$
$$\beta_M(Q^2) = 1.08 \pm 0.12_{stat} \ (10^{-4}.fm^3) \ .$$

The corresponding Λ parameters are:

$$\Lambda_\alpha = 0.631 \pm 0.011_{stat} \ (GeV)$$
$$\Lambda_\beta = 0.745 \pm 0.021_{stat} \ (GeV) \ ,$$

which lead to the following structure functions:

$$P_{LL} - P_{TT}/\epsilon = 18.70 \pm 0.38_{stat} \ (GeV^{-2})$$
$$P_{LT} = -3.48 \pm 0.25_{stat} \ (GeV^{-2}) \ .$$

The DR fit hides an undiscussed feature. The model depends on the RCS electric and magnetic polarizabilities used as input in the code. Indeed the RCS polarizabilities appear in equations 2.8 and 2.9. Moreover, the value of $\bar{\beta}_M$ has recently changed ($\bar{\beta}_M = (2.5 \pm 0.4) \cdot 10^{-4} \ fm^3$ [28]) and may change again in the future. So, one can wonder if variations of RCS polarizabilities would impact our DR analysis.

It is likely that a change in the RCS values in equations 2.8 and 2.9 will be compensated in our DR fit by a change of the fitted Λ parameters, leaving finally the GPs and the structure functions unchanged [99]. However, this remains to be verified.

5.7 Systematic errors

In this section we explain the choice that has been made to estimate the systematic errors in our analyses. We describe the two estimation methods that we used for the LEX fit, and we conclude more briefly for the DR fit.

5.7.1 First method: changing the renormalization of the experimental cross section

The first method consists in using the renormalization factor F^{norm} to estimate the systematic errors. In this section we assume that the global systematic error can be obtained by considering a simple change of overall renormalization.

As explained in section 5.4 we believe that the renormalization factor corrects our data from a global bias with a excellent accuracy. However it does not prevent our analysis from inhomogeneous issues which can be due for example to:

- angular distortions caused by bias in optics or local loss of events. By observations of variations between different analyses at different stages of our progress we can estimate this as a ± 0.01 variation of F^{norm}.

- non-homogenous radiative effects that are ignored by our averaging of F^{rad}. This effect shows variations that are equivalent at maximum to a ± 0.007 variation of F^{norm} (cf. section 5.2.2).

- non-homogenous renormalization factor. In section 5.4.3 we have observed that the renormalization factor undergoes variations from a setting to another (cf. table 5.4.2). We consider that they induce a systematic error of ± 0.006 of F^{norm}.

- error induced by applying a renormalization factor determined by low-energy settings to other settings. By doing this we assumed that the main part of systematic errors have a common origin. But we observed a ± 0.006 variation between the LOW and LOW-bis renormalization factors. We can then estimate the systematic error brought by this assumption to be about the same order.

- moreover we can add the systematic error induced by the use of different conditions for the LEX fit in the iterative procedure which allows to determine F^{norm}. It has been shown in section 5.4.3 that it is a ± 0.002 effect on F^{norm}.

Finally by summing quadratically those five systematic-error sources we estimate our total systematic error as an uncertainty of ± 0.015 on the renormalization factor, or, in other terms, a total systematic uncertainty of $\pm 1.5\%$ on each cross-section point. This effect is propagated to the LEX and DR analysis, by simply changing the global renormalization factor that enters in the fits. For the LEX analysis we find that $\Delta F^{norm} \pm 0.015$ induces the following changes in the physics observables:

$$\Delta P_{LL} - P_{TT}/\epsilon = \mp 3.64_{syst} \ (GeV^{-2})$$
$$\Delta P_{LT} = \mp 1.57_{syst} \ (GeV^{-2}).$$

The errors are anti-correlated with respect to ΔF^{norm}.

5.7.2 Second method : multiple LEX analyses

The second method we used to estimate the systematic error is based on multiple analyses of the data. We had the chance to produce independent LEX analyses with different choices, i.e. different: spectrometers optics, target positioning, analysis cuts, renormalization factors, bin selection. So we can estimate the main systematic effects, which are the following:

- using the renormalization factor from another analysis to the nominal one induces structure-function variations of $\Delta P_{LL} - P_{TT}/\epsilon = \pm 2.35 \ (GeV^{-2})$ and $\Delta P_{LT} = \pm 1.02 \ (GeV^{-2})$.

- changing the cut on the reconstructed vertex by ± 6 mm induces structure-function variations of $\Delta P_{LL} - P_{TT}/\epsilon = \pm 0.21 \ (GeV^{-2})$ and $\Delta P_{LT} = \pm 0.30 \ (GeV^{-2})$.

- multiplying the upper cut on the missing-mass squared by 2 or 0.5 induces structure-function variations of $\Delta P_{LL} - P_{TT}/\epsilon = \pm 1.67 \ (GeV^{-2})$ and $\Delta P_{LT} = \pm 0.33 \ (GeV^{-2})$.

- using a theoretical cross-section in VCSSIM that contains a GP effect (based on our final result) induces structure-function variations of $\Delta P_{LL} - P_{TT}/\epsilon = \pm 0.15 \ (GeV^{-2})$ and $\Delta P_{LT} = \pm 0.11 \ (GeV^{-2})$.

- not considering the local target boiling described in section 4.4.2 induces structure-function variations of $\Delta P_{LL} - P_{TT}/\epsilon = \pm 0.1 \ (GeV^{-2})$ and $\Delta P_{LT} = \pm 0.8 \ (GeV^{-2})$.

- considering a supplementary analysis cut in order to remove the unconsistency of figure 4.22 for the setting INP induces structure-function variations of $\Delta P_{LL} - P_{TT}/\epsilon = \pm 1.02 \ (GeV^{-2})$ and $\Delta P_{LT} = \pm 0.92 \ (GeV^{-2})$.

- considering different form-factor parametrizations induces $\Delta P_{LL} - P_{TT}/\epsilon = \pm 0.2 \ (GeV^{-2})$ and $\Delta P_{LT} = \pm 0.2 \ (GeV^{-2})$ (cf. table 5.4.3-c).

- changing the K_{thr} value (defined section 5.5.2) inside the stability plateau of figure 5.18 induces $\Delta P_{LL} - P_{TT}/\epsilon = \pm 0.5 \ (GeV^{-2})$ and $\Delta P_{LT} = \pm 0.1 \ (GeV^{-2})$.

- not using the gradient selection induces structure-functions variations of $\Delta P_{LL} - P_{TT}/\epsilon = \pm 0.4 \ (GeV^{-2})$ and $\Delta P_{LT} = \pm 0.01 \ (GeV^{-2})$.

If we do the quadratic sum we find:

$$\Delta P_{LL} - P_{TT}/\epsilon = \pm 3.14 \ (GeV^{-2})$$
$$\Delta P_{LT} = \pm 1.66 \ (GeV^{-2}) \ ,$$

which agrees well with the previous determination. The correlations of signs cannot be determined by this method of estimation of systematic errors.

Conclusion on systematic errors

For the LEX fit we have been able to estimate the systematic errors on the fitted observables by two methods, and they are in good agreement. We decided to use the first method because of its simplicity of application. The systematic errors for the structure functions, presented in section 5.8, are obtained this way. They are then propagated to the "LEX" GP determination of section 5.5.4.

For the DR fit we have not done such an extensive study, therefore, thanks to its simplicity, we will adopt the first method, i.e. we apply a change $\Delta F^{norm} = \pm 0.015$ in order to find the systematic error on the observables extracted by the DR fit. We find[6]:

$$\Delta \alpha_E(Q^2) = \mp 0.98_{syst} \ (10^{-4}.fm^3)$$
$$\Delta \beta_M(Q^2) = \pm 0.90_{syst} \ (10^{-4}.fm^3) \ ,$$

$$\Delta \Lambda_\alpha = \mp 0.121_{syst} \ (GeV)$$
$$\Delta \Lambda_\beta = \mp 0.188_{syst} \ (GeV) \ ,$$

$$\Delta P_{LL} - P_{TT}/\epsilon = \mp 3.93_{syst} \ (GeV^{-2})$$
$$\Delta P_{LT} = \mp 1.86_{syst} \ (GeV^{-2}) \ .$$

The correlations of sign with ΔF^{norm} observed here are due to the use of the first method and will not be kept in the following.

5.8 Final results

The first fit, based on the LET, is in principle model-independent, technically easy to implement but requires to be done carefully because of higher-orders in q'_{cm}.

While our LEX result for P_{LT} is almost not impacted by the mask selection, our LEX result for $P_{LL} - P_{TT}/\epsilon$ is very sensitive to it: the fitted value changes from $15 \ GeV^{-2}$ (without mask) to $18 \ GeV^{-2}$ (with mask selection), i.e. it changes by $3 \ GeV^{-2}$, which is almost equal to one systematic standard deviation. This can be seen as having introduced some degree of DR-model-dependency in our LEX

---

[6]The systematic errors present a small asymmetry in positive and negative, the upper limit is kept to express the error symmetrically.

fit. The "LEX GPs" extracted in section 5.5.4 depend even more obviously on the DR model.

The second extraction, based entirely on the DR model, is more straightforward but is technically harder to implement because of the computational time.

To perform both extractions we used cross sections corrected from radiative effects, and renormalized. We have shown the importance of the renormalization process which minimizes the systematic effects in our analyses and makes the extractions independent of form-factor parametrizations.

The extracted structure functions are summarized in section 5.8.1 and the extracted GPs are summarized in section 5.8.2.

Thanks to the strength of the renormalization process we were able to quantify the systematic errors for both extractions, LEX and DR. And thanks to the flexibility of the LEX fit we were able to check the systematic errors by doing several independent analyses.

5.8.1 Structure functions

The final extracted values for the LEX fit are:

$$
\begin{aligned}
P_{LL} - P_{TT}/\epsilon \quad (LEX) \quad &= 18.10 \pm 0.56_{stat} \pm 3.64_{syst} \; (GeV^{-2}) \\
P_{LT} \quad (LEX) \quad &= -3.59 \pm 0.31_{stat} \pm 1.57_{syst} \; (GeV^{-2}),
\end{aligned}
$$

and the DR fit gives:

$$
\begin{aligned}
P_{LL} - P_{TT}/\epsilon \quad (DR) \quad &= 18.70 \pm 0.38_{stat} \pm 3.93_{syst} \; (GeV^{-2}) \\
P_{LT} \quad (DR) \quad &= -3.48 \pm 0.25_{stat} \pm 1.86_{syst} \; (GeV^{-2}).
\end{aligned}
$$

These two sets of results are in excellent agreement. The agreement is even more meaningful and satisfying for P_{LT} which, for the LEX extraction, does not depend on the mask selection and so is entirely independent of the DR model. Figures 5.22 and 5.23 show those measurements together with the world data. Figure 5.22 presents a non-simple Q^2 behavior of $P_{LL} - P_{TT}/\epsilon$ which demands to be explored further in the region around $Q^2 = 0.33\,GeV^2$. Our fitted value of P_{LT} is rather small and also not in smooth agreement with the results at $Q^2 = 0.33\,GeV^2$. Also, the picture at $Q^2 = 0\;GeV^2$ may change in the future due to the new measurements of the RCS polarizabilities.

5.8.2 GPs

The final extracted GPs by means of the LEX fit plus DR-subtraction of the spin-flip GPs are:

$$
\begin{aligned}
\alpha_E(Q^2) \quad (LEX) \quad &= 3.90 \pm 0.14_{stat} \pm 0.92_{syst} \; (10^{-4}.fm^3) \\
\beta_M(Q^2) \quad (LEX) \quad &= 1.14 \pm 0.15_{stat} \pm 0.78_{syst} \; (10^{-4}.fm^3).
\end{aligned}
$$

From the DR fit we obtained:

Figure 5.22: World data for $P_{LL} - P_{TT}/\epsilon$ including the present extractions at $Q^2 = 0.2\,GeV^2$ (in black). The data and curve follow the conventions of Figure 2.7. The green crosses are the preliminary results from [72] ($Q^2 = 0.45\,GeV^2$) and [71] ($Q^2 = 0.1\,GeV^2$).

$$\begin{aligned}
\alpha_E(Q^2) \quad (DR) \quad &= 4.05 \pm 0.10_{stat} \pm 0.98_{syst} \ (10^{-4}.fm^3) \\
\beta_M(Q^2) \quad (DR) \quad &= 1.08 \pm 0.12_{stat} \pm 0.90_{syst} \ (10^{-4}.fm^3).
\end{aligned}$$

The two set of results are in excellent agreement. Figures 5.24 and 5.25 allow to compare the present measurements with the world data, and the same comments can be made as for the structure functions.
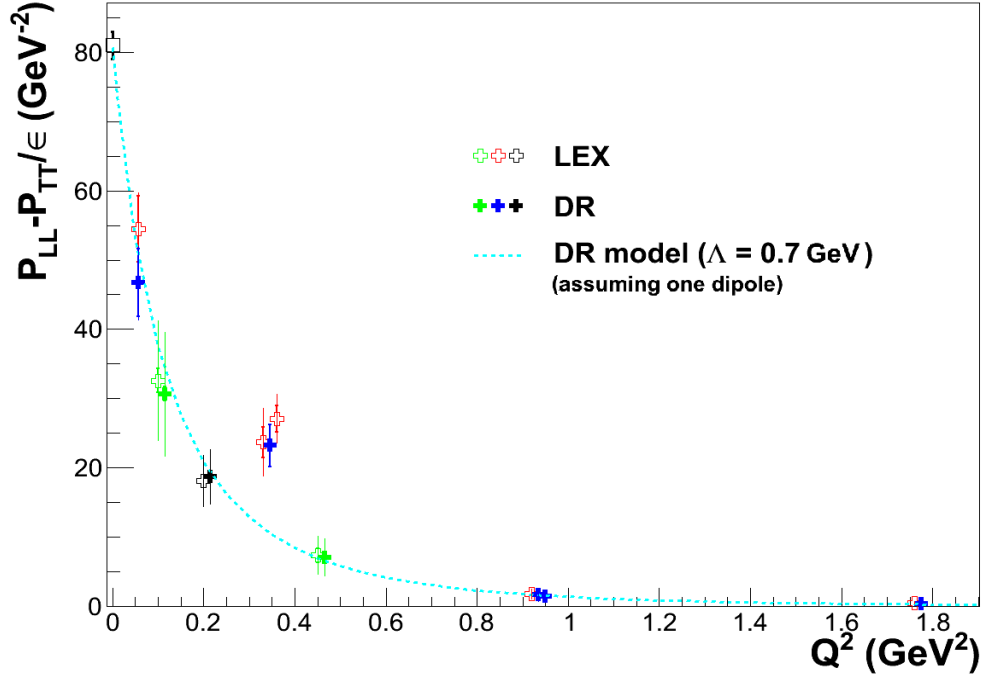
Figure 5.23: World data for P_{LT} including the present extractions at $Q^2 = 0.2\ GeV^2$ (in black). The data and curve follow the conventions of Figure 2.8. The green crosses are the preliminary results from [72] ($Q^2 = 0.45\ GeV^2$) and [71] ($Q^2 = 0.1\ GeV^2$).

Figure 5.24: World data for $\alpha_E(Q^2)$ including the present extractions at $Q^2 = 0.2\ GeV^2$ (in black). The data and curve follow the conventions of Figure 2.7. The green crosses are the preliminary results from [72] ($Q^2 = 0.45\ GeV^2$) and [71] ($Q^2 = 0.1\ GeV^2$).
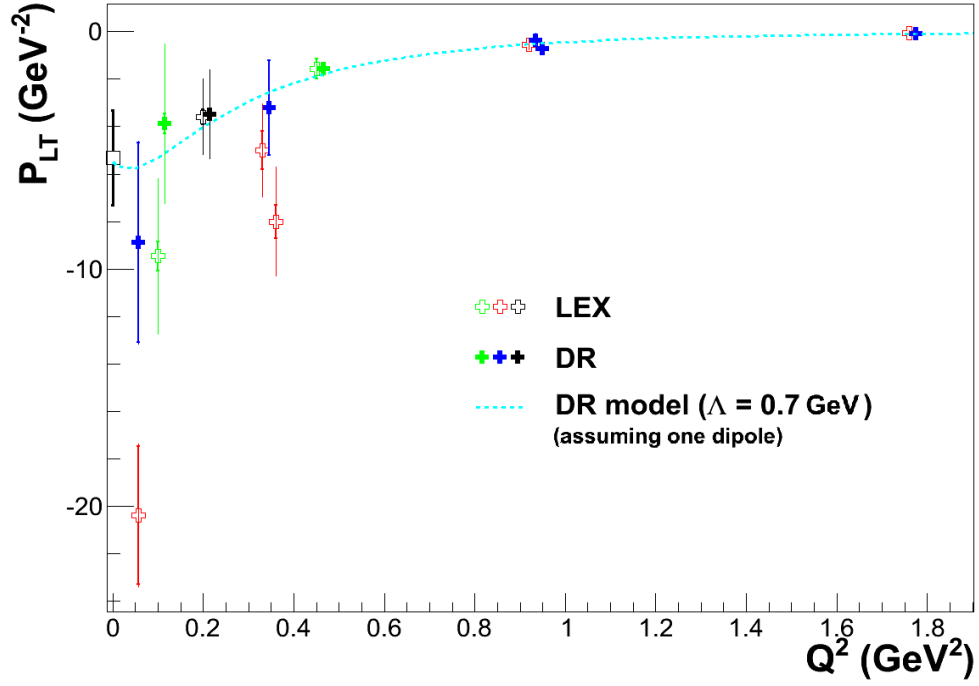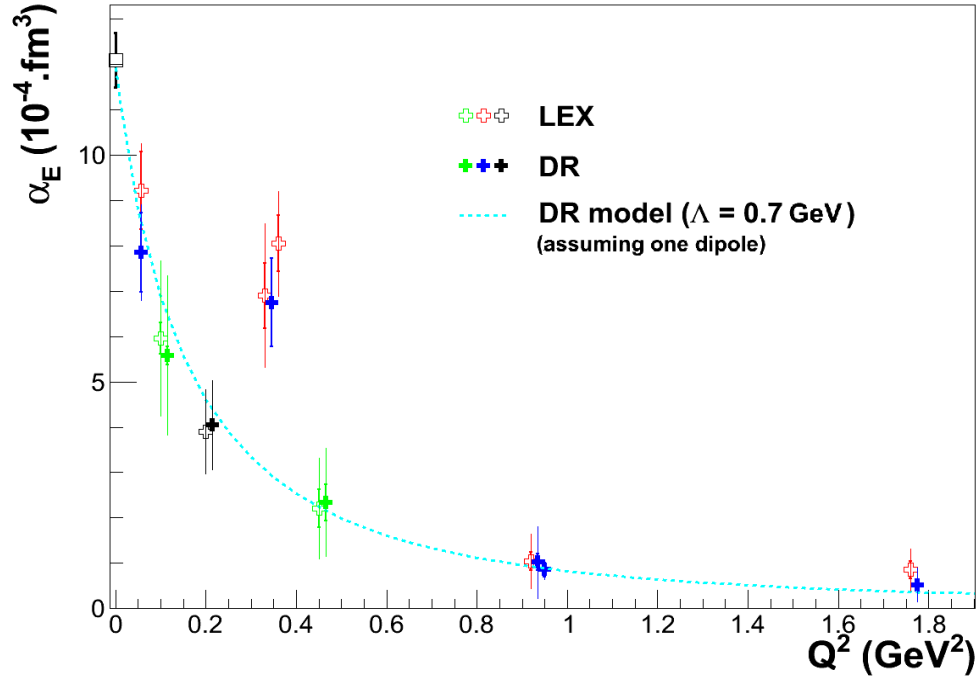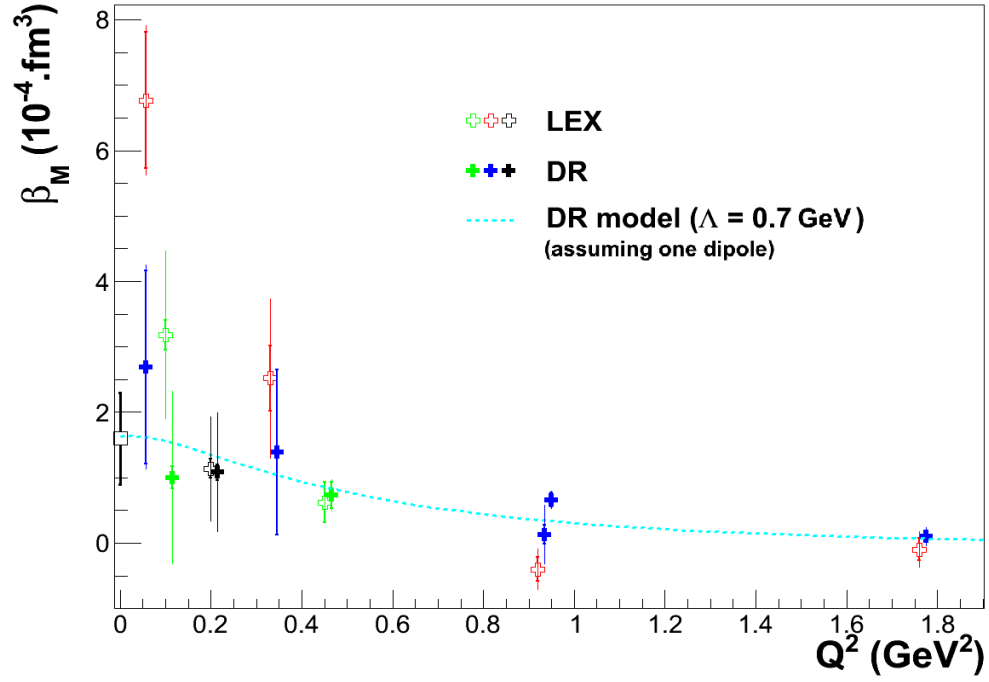
Figure 5.25: World data for $\beta_M(Q^2)$ including the present extractions at $Q^2 = 0.2\ GeV^2$ (in black). The data and curve follow the conventions of Figure 2.8. The green crosses are the preliminary results from [72] ($Q^2 = 0.45\ GeV^2$) and [71] ($Q^2 = 0.1\ GeV^2$).

Conclusion

In this thesis we analysed the data of a photon electroproduction ($ep \to ep\gamma$) experiment at MAMI, at $Q^2 = 0.2\ GeV^2$. We extracted a number of observables characterizing the VCS process at low energy: the structure functions $P_{LL} - P_{TT}/\epsilon$ and P_{LT}, and the electric and magnetic GPs $\alpha_E(Q^2)$, $\beta_M(Q^2)$.

This study was motivated by the previous VCS experiments. Their results have raised questions, namely about the Q^2-behavior of the electric generalized polarizability which demanded to be explored. This work is a part of a more complete experiment that also covered two other Q^2-values: 0.1 and 0.45 GeV^2, in order to obtain a more complete picture of the situation in the region around $Q^2 = 0.33\ GeV^2$.

The first difficulty of such experiments is the smallness of the $ep \to ep\gamma$ cross section, requiring to accumulate enough statistics. Our experiment is a high-statistics one, with $\approx 10^6$ events identified as $ep \to ep\gamma$ when summed over our five settings at $Q^2 = 0.2\ GeV^2$.

The second and main difficulty to extract GPs comes from their small contribution (0-15%) to the photon electroproduction cross-section, requiring to measure this cross section with small systematic uncertainties, of the order of a few percent at maximum. In order to obtain the systematic precision of $\pm 1.5\%$ our experiment had a few strong points. First, we benefited of the MAMI facility and the A1 spectrometers. The high-duty cycle of the accelerator and the high resolution of the spectrometers are mandatory for such experiments. The calibration work was also a determinant part of our analysis. Its relevance was confirmed by the use of a Monte Carlo simulation. The last strong aspect is the renormalization procedure. Indeed our renormalization work highly diminished the impact of the possible experimental inconsistencies and of the theoretical uncertainties, e.g. the blur brought by the limited form-factor knowledge.

We were able to extract the structure functions and the GPs by two different approaches. The first one is based on the LET and was widely explored in this thesis. The second extraction, based on the dispersion relation model, was more straightforward but explored to a less extent. Those two different types of analysis were already done by previous experiments, but our experiment also contains two specificities.

The first one resides in the choice of the analysed phase-space. The measured cross-section points were distributed in different angular regions of interest, thus increasing the sensitivity of our analyses to the structure functions and GPs.

The second original feature is the use of the DR model to select the analysed data in the LEX analysis. The previous observations (from the Bates experiment)

and the ones we did during our analysis are evidences that the higher-order terms in the final photon energy q'_{cm} impact our results. The "mask selection" that we built, based on the estimation of the higher-order terms by the DR model, is then an essential feature of our LEX analysis.

The two different extractions, LEX and DR, are in very good agreement, within their statistical error which is quite small. Actually, the results are dominated by the systematics which are difficult to reduce in VCS experiments.

The parallel analyses at $Q^2 = 0.45 \ GeV^2$ [72] and $Q^2 = 0.1 \ GeV^2$ [71], associated with this one, have established a preliminary behavior of the electric GP. This behavior is not in smooth agreement with the previous MAMI results. Exploring a GP extraction at $Q^2 = 0.33 \ GeV^2$ in a wider angular phase space (namely out-of-plane, as in our experiment) would certainly give more insight in the present puzzle.

The generalized magnetic polarizability of the proton is smaller and by consequence its extraction is more difficult due to the systematic errors. This complicates the observation of an extremun in the $\beta_M(Q^2)$ (or P_{LT}) Q^2-behavior. However one observes also a non-smooth behavior with respect to the previous MAMI results. Because of the recent changes in the RCS magnetic polarizability value, we can anticipate that figure 5.25 will also change at $Q^2 = 0$ in the future.

To conclude, the study of the GP behavior requires more investigations and will be hopefully pushed further [100]. In a near future, our final electric GP result will be confronted to the result of another VCS experiment done at MAMI, in the Δ-resonance region, also at $Q^2 = 0.2 \ GeV^2$ [70].

Bibliography

[1] E. Rutherford. The scattering of alpha and beta particles by matter and the structure of the atom. *Phil. Mag.*, 21:669–688, 1911.

[2] J. Chadwick. Possible Existence of a Neutron. *Nature*, 129:312, 1932.

[3] Enrico Fermi. Quantum theory of radiation. *Rev. Mod. Phys.*, 4:87–132, Jan 1932.

[4] H. Arenhövel and D. Drechsel. Generalized nuclear polarizabilities in (e, e' γ) coincidence experiments. *Nucl. Phys.*, A233:153–163, 1974.

[5] Pierre A. M. Guichon, G. Q. Liu, and Anthony William Thomas. Virtual Compton scattering and generalized polarizabilities of the proton. *Nucl. Phys.*, A591:606–638, 1995.

[6] D. Drechsel, G. Knochlein, A. Metz, and S. Scherer. Generalized polarizabilities and the spin averaged amplitude in virtual Compton scattering off the nucleon. *Phys. Rev.*, C55:424–430, 1997.

[7] J. Roche et al. The First determination of generalized polarizabilities of the proton by a virtual Compton scattering experiment. *Phys. Rev. Lett.*, 85:708, 2000.

[8] H. Merkel et al. A study of the Q^2-dependence of the structure functions and the generalized polarizabilities in VCS at MAMI. *http://wwwa1.kph.uni-mainz.de/A1/publications/proposals/MAMI-A1-1-09.pdf*, 2009.

[9] Gerald A. Miller. Charge Density of the Neutron. *Phys. Rev. Lett.*, 99:112001, 2007.

[10] Marc Vanderhaeghen and Thomas Walcher. Long Range Structure of the Nucleon. *Nucl. Phys. News*, 21:14–22, 2011.

[11] Robert Hofstadter. Electron scattering and nuclear structure. *Rev. Mod. Phys.*, 28:214–254, 1956.

[12] M. N. Rosenbluth. High Energy Elastic Scattering of Electrons on Protons. *Phys. Rev.*, 79:615–619, 1950.

[13] R. Hofstadter. Nuclear and nucleon scattering of high-energy electrons. *Ann. Rev. Nucl. Part. Sci.*, 7:231–316, 1957.

[14] J. C. Bernauer et al. Electric and magnetic form factors of the proton. *Phys. Rev.*, C90(1):015206, 2014.

[15] V. Punjabi, C. F. Perdrisat, M. K. Jones, E. J. Brash, and C. E. Carlson. The Structure of the Nucleon: Elastic Electromagnetic Form Factors. *Eur. Phys. J.*, A51:79, 2015.

[16] M. Mihovilovic and H. Merkel. Initial state radiation experiment at MAMI. *AIP Conf. Proc.*, 1563:187–190, 2013.

[17] J. Friedrich and T. Walcher. A Coherent interpretation of the form-factors of the nucleon in terms of a pion cloud and constituent quarks. *Eur. Phys. J.*, A17:607–623, 2003.

[18] J. Arrington, W. Melnitchouk, and J. A. Tjon. Global analysis of proton elastic form factor data with two-photon exchange corrections. *Phys. Rev.*, C76:035205, 2007.

[19] J. C. Bernauer et al. High-precision determination of the electric and magnetic form factors of the proton. *Phys. Rev. Lett.*, 105:242001, 2010.

[20] P. P. Martel et al. Measurements of Double-Polarized Compton Scattering Asymmetries and Extraction of the Proton Spin Polarizabilities. *Phys. Rev. Lett.*, 114(11):112501, 2015.

[21] D. Babusci, G. Giordano, A. I. L'vov, G. Matone, and A. M. Nathan. Low-energy Compton scattering of polarized photons on polarized nucleons. *Phys. Rev.*, C58:1013–1041, 1998.

[22] D. l'Huillier. Diffusion Compton Virtuelle a basse energie. *PHD thesis, UBP-Clermont-Fd, DAPNIA/SPHN-97-01T*, 1999.

[23] V. Olmos de Leon et al. Low-energy Compton scattering and the polarizabilities of the proton. *Eur. Phys. J.*, A10:207–215, 2001.

[24] F. E. Low. Scattering of light of very low frequency by systems of spin 1/2. *Phys. Rev.*, 96:1428–1432, 1954.

[25] V.A Petrun'kin. *Sov. Phys. JTEP*, 13,808, 1961.

[26] V.I Gol'danski et al. *[Sov. Phys. JETP11, 1223]*, 38, 1960.

[27] A. M. Baldin et al. *Nucl. Phys. 18*, 310-317, 1960.

[28] K.A. Olive et al. Particle data group. *Chin. phys. C*, 38, 090001, 2014.

[29] Stefan Scherer. Compton scattering and generalized polarizabilities. *AIP Conf. Proc.*, 768:110–114, 2005. [,110(2004)].

[30] Stefan Scherer. Chiral perturbation theory: Success and challenge. *Eur. Phys. J.*, A28:59–70, 2006.

[31] M. Gorchtein, C. Lorce, B. Pasquini, and M. Vanderhaeghen. Light-front interpretation of Proton Generalized Polarizabilities. *Phys. Rev. Lett.*, 104:112001, 2010.

[32] A. Metz and D. Drechsel. Generalized polarizabilities of the nucleon studied in the linear sigma model. 2. *Z. Phys.*, A359:165–172, 1997.

[33] Pierre A. M. Guichon and M. Vanderhaeghen. Virtual Compton scattering off the nucleon. *Prog. Part. Nucl. Phys.*, 41:125–190, 1998.

[34] F. E. Low. Bremsstrahlung of very low-energy quanta in elementary particle collisions. *Phys. Rev.*, 110:974–977, 1958.

[35] D. Drechsel, G. Knochlein, A. Yu. Korchin, A. Metz, and S. Scherer. Structure analysis of the virtual Compton scattering amplitude at low-energies. *Phys. Rev.*, C57:941–952, 1998.

[36] Marc Vanderhaeghen. Real and virtual Compton scattering off the nucleon. *Eur. Phys. J.*, A8:455–479, 2000.

[37] B. Pasquini, M. Gorchtein, D. Drechsel, A. Metz, and M. Vanderhaeghen. Dispersion relation formalism for virtual Compton scattering off the proton. *Eur. Phys. J.*, A11:185–208, 2001.

[38] D. Drechsel, B. Pasquini, and M. Vanderhaeghen. Dispersion relations in real and virtual Compton scattering. *Phys. Rept.*, 378:99–205, 2003.

[39] D. Drechsel, G. Knochlein, A. Yu. Korchin, A. Metz, and S. Scherer. Low-energy and low momentum representation of the virtual Compton scattering amplitude. *Phys. Rev.*, C58:1751–1757, 1998.

[40] Lothar Tiator and Sabit Kamalov. Maid analysis techniques. In *Proceedings, 5th International Workshop on Physics of excited nucleons (NSTAR 2005)*, pages 16–25, 2006.

[41] Steven Weinberg. Phenomenological Lagrangians. *Physica*, A96:327, 1979.

[42] Veronique Bernard. Chiral Perturbation Theory and Baryon Properties. *Prog. Part. Nucl. Phys.*, 60:82–160, 2008.

[43] V. Bernard, Norbert Kaiser, and Ulf-G. Meissner. Chiral dynamics in nucleons and nuclei. *Int. J. Mod. Phys.*, E4:193–346, 1995.

[44] Veronique Bernard, Norbert Kaiser, and Ulf G. Meissner. Chiral expansion of the nucleon's electromagnetic polarizabilities. *Phys. Rev. Lett.*, 67:1515–1518, 1991.

[45] Veronique Bernard, Norbert Kaiser, and Ulf G. Meissner. Chiral expansion of the nucleon's electromagnetic polarizabilities. *Phys. Rev. Lett.*, 67:1515–1518, 1991.

[46] Elizabeth Ellen Jenkins and Aneesh V. Manohar. Baryon chiral perturbation theory using a heavy fermion Lagrangian. *Phys. Lett.*, B255:558–562, 1991.

[47] Thomas R. Hemmert, Barry R. Holstein, Germar Knochlein, and Dieter Drechsel. Generalized polarizabilities of the nucleon in chiral effective theories. *Phys. Rev.*, D62:014013, 2000.

[48] Vadim Lensky and Vladimir Pascalutsa. Predictions of chiral perturbation theory for Compton scattering off protons. *PoS*, EFT09:033, 2009.

[49] M. Vanderhaeghen. Virtual Compton scattering study below pion production threshold. *Phys. Lett.*, B368:13–19, 1996.

[50] A. Yu. Korchin and O. Scholten. Nucleon polarizabilities in virtual Compton scattering. *Phys. Rev.*, C58:1098–1100, 1998.

[51] Murray Gell-Mann and M Levy. The axial vector current in beta decay. *Nuovo Cim.*, 16:705, 1960.

[52] A. Metz and D. Drechsel. Generalized polarizabilities of the nucleon studied in the linear sigma model. *Z. Phys.*, A356:351–357, 1996.

[53] Stephen L. Adler. Calculation of the axial vector coupling constant renormalization in beta decay. *Phys. Rev. Lett.*, 14:1051–1055, 1965.

[54] William I. Weisberger. Renormalization of the Weak Axial Vector Coupling Constant. *Phys. Rev. Lett.*, 14:1047–1051, 1965.

[55] M. L. Goldberger and S. B. Treiman. Decay of the pi meson. *Phys. Rev.*, 110:1178–1184, 1958.

[56] O. W. Greenberg and M. Resnikoff. Symmetric Quark Model of Baryon Resonances. *Phys. Rev.*, 163:1844–1851, 1967.

[57] Nathan Isgur and Gabriel Karl. P Wave Baryons in the Quark Model. *Phys. Rev.*, D18:4187, 1978.

[58] G. Q. Liu, Anthony William Thomas, and Pierre A. M. Guichon. Virtual Compton scattering from the proton and the properties of nucleon excited states. *Austral. J. Phys.*, 49:905–918, 1996.

[59] B. Pasquini, S. Scherer, and D. Drechsel. Generalized polarizabilities of the proton in a constituent quark model revisited. *Phys. Rev.*, C63:025205, 2001.

[60] M. Gorchtein A. Metz B. Pasquini, D. Drechsel and . M. Vanderhaeghen. Dispersion relation formalism for virtual Compton scattering and the generalized polarizabilities of the nucleon. *Phys. Rev. C 62, 052201*, 2000.

[61] B. Pasquini, S. Scherer, and D. Drechsel. Generalized Polarizabilities in a Constituent Quark Model. *Talk given at NSTAR2001, Workshop on The Physics of Excited Nucleons, arXiv:nucl-th/0105074v1*, 2001.

[62] N. d'Hose. Virtual Compton scattering at MAMI. *Eur. Phys. J.*, A28S1:117–127, 2006.

[63] G. Laveissiere et al. Measurement of the generalized polarizabilities of the proton in virtual Compton scattering at Q**2 = 0.92-GeV**2 and 1.76-GeV**2. *Phys. Rev. Lett.*, 93:122001, 2004.

[64] H. Fonvieille et al. Virtual Compton Scattering and the Generalized Polarizabilities of the Proton at $Q^2 = 0.92$ and 1.76 GeV^2. *Phys. Rev.*, C86:015210, 2012.

[65] E. J. Brash, A. Kozlov, S. Li, and G. M. Huber. New empirical fits to the proton electromagnetic form-factors. *Phys. Rev.*, C65:051001, 2002.

[66] P. Bourgeois et al. Measurements of the generalized electric and magnetic polarizabilities of the proton at low Q**2 using the VCS reaction. *Phys. Rev. Lett.*, 97:212001, 2006.

[67] P. Bourgeois et al. Measurements of the generalized electric and magnetic polarizabilities of the proton at low Q-2 using the virtual Compton scattering reaction. *Phys. Rev.*, C84:035206, 2011.

[68] P. Janssens et al. A New measurement of the structure functions P(LL) - P(TT)/ epsilon and P(LT) in virtual Compton scattering at Q**2 = 0.33 (GeV/c)**2. *Eur. Phys. J.*, A37:1, 2008.

[69] L. Doria et al. Measurement of the Beam-Recoil Polarization in Low-Energy Virtual Compton Scattering from the Proton. *Phys. Rev.*, C92(5):054307, 2015.

[70] N. Sparveris et al. MAMI A1 Proposal, Proposed experiment to study the nucleon structure by measurement of Virtual Compton Scattering at the Delta resonance at MAMI. PhD Thesis of A.Blomberg, Temple University, Philadelphia (in preparation). *http://quarks.temple.edu/wp-content/uploads/2012/06/MAMI-A1-03-12.pdf*, 2011.

[71] J. Bericic. Measurement of Generalized Polarizabilities of the Proton by Virtual Compton Scattering. *PHD thesis, Univerza V Ljubljani Fakulteta Za Matematiko in Fiziko (Ljubljana)*, 2015.

[72] M. Benali. Structure interne du proton à haute et basse énergie par la diffusion Compton virtuelle. *PHD thesis, UBP-Clermont-Fd*, 2016.

[73] H. Herminghaus, A. Feder, K. H. Kaiser, W. Manz, and H. Von Der Schmitt. The Design of a Cascaded 800-MeV Normal Conducting CW Racetrack Microtron. *Nucl. Instrum. Meth.*, 138:1–12, 1976.

[74] A. Jankowiak. The Mainz Microtron MAMI: Past and future. *Eur. Phys. J.*, A28S1:149–160, 2006.

[75] K. I. Blomqvist et al. The three-spectrometer facility at the Mainz microtron MAMI. *Nucl. Instrum. Meth.*, A403:263–301, 1998.

[76] P. Janssens. Double-polarized virtual Compton scattering as a probe of the proton structure. *PHD thesis, Gent Universiteit*, 2007.

[77] http://wwwa1.kph.uni mainz.de/A1/Welcome.en.html.

[78] J. Roche. Diffusion Compton virtuelle à MAMI. *PHD thesis, UBP-Clermont-Fd, DAPNIA/SPhN-98-06T, DU 1085*, 1999.

[79] Markus Weis Michael O. Distler, Harald Merkel. Data acquisition and analysis for the 3-spectrometer-setup at MAMI. *Proceedings of the 12th IEEE Real Time Congress on Nuclear and Plasma Sciences, Valencia*, 2001.

[80] B.S. Schlimme. Scintillator efficiency computer code. *(Mainz U.)*, private communication.

[81] H. Fonvieille. A study of scintillator efficiencies. *http://wwwa1.kph.uni-mainz.de/users/fonvieil/vcsq2/2014-and-2015-vcsq2-HF-scintillator-efficiency/*, 2015-04-memo-effic-scint-3.pdf.

[82] H. Fonvieille. New optic files for spectrometer b at high momentum. *http://wwwa1.kph.uni-mainz.de/users/fonvieil/vcsq2/2012-12-summary-specB-optim/*, 2013-04-04-memo-v2.ps.

[83] M Mihovilovic. Alignment measurement. *(Mainz U.)*, private communication.

[84] H. Fonvieille. Spec a optic versus magnetic field. *http://wwwa1.kph.uni-mainz.de/users/fonvieil/vcsq2/2015-11-vcsq2-HF-memo-Atheta0-Aphi0-optics-vs-field/*, memo-v4.ps.

[85] L. Correa. Calibration of VDC and snow thickness in view of VCS analyses. *http://wwwa1.kph.uni-mainz.de/users/fonvieil/vcsq2/2013-03-calibr-snow-Bmom-LC/*, calib.pdf.

[86] L. Correa. Method to correct the coincidence dead time from lumi++ ouput files. *http://wwwa1.kph.uni-mainz.de/users/fonvieil/vcsq2/2013-06-lumi-and-deadtime-LC/*, LC-correctdeadtime-june2013.pdf.

[87] H. Merkel. Luminosity computer code. *http://wwwa1.kph.uni-mainz.de/users/fonvieil/vcsq2/2013-new-script-lumi++/*.

[88] P. Janssens et al. Monte Carlo simulation of virtual Compton scattering below pion threshold. *Nucl. Instrum. Meth.*, A566:675–686, 2006.

[89] CERN. Computer code. *https://root.cern.ch/*.

[90] M. Vanderhaeghen. VCS-BHB computer code. *(Mainz U.)*, private communication.

[91] B. Pasquini. VCS-DR computer code, version maid2007. *(Pavia U.)*, private communication.

[92] M. Vanderhaeghen, J. M. Friedrich, D. Lhuillier, D. Marchand, L. Van Hoorebeke, and J. Van de Wiele. QED radiative corrections to virtual Compton scattering. *Phys. Rev.*, C62:025501, 2000.

[93] L. Correa. VCS Experiment - Radiative corrections. *18 p. <in2p3-01010317>, http://wwwa1.kph.uni-mainz.de//users/fonvieil/vcsq2/2014-04-RadCorr-LC, 2014-04-25-RadiativeCorrections.pdf*, 2014.

[94] D. Marchand. Calcul des corrections radiatives à la diffusion Compton virtuelle / Mesure absolue de l'énergie du faisceau d'électrons de Jefferson Lab. (Hall A) par une méthode magnétique : Projet Arc. *PHD thesis, UBP-Clermont-Fd, DAPNIA/SPHN-98-04T, DU. 1008*, 1998.

[95] L. C. Maximon and J. A. Tjon. Radiative corrections to electron proton scattering. *Phys. Rev.*, C62:054320, 2000.

[96] D. R. Yennie, Steven C. Frautschi, and H. Suura. The infrared divergence phenomena and high-energy processes. *Annals Phys.*, 13:379–452, 1961.

[97] H. Fonvieille. Treatment of the statistical error bar related to the VCSSIM simulation. *http://wwwa1.kph.uni-mainz.de/users/fonvieil/vcsq2/2014-12-study-errstat-from-vcssim/*, memo-v2.ps.

[98] F. James. Function minimization and error analysis. *http://root.cern.ch/sites/d35c7d8c.web.cern.ch/files/minuit.pdf/*, 94.1, 1994.

[99] H. Fonvieille and B. Pasquini. Private communication. 2015.

[100] N. Sparveris et al. Jefferson Lab Proposal PR12-15-001, Measurement of the Generalized Polarizabilities of the Proton in Virtual Compton Scattering. *https://www.jlab.org/exp-prog/proposals/15/PR12-15-001.pdf*, 2015.

Appendix A

VCS coefficients in the LEX expansion

In the LET expression, v_{LL} and v_{LT} are angular dependent functions. We recall their expression here, following the notations of [33]:

$$
\begin{aligned}
v_{LL}(\varphi_{cm}, \theta_{cm}, q_{cm}, \varepsilon) &= 2K_2 \varepsilon v_1 \\
v_{LT}(\varphi_{cm}, \theta_{cm}, q_{cm}, \varepsilon) &= 2K_2 (v_2 - \frac{\tilde{q}_{cm}^0}{q_{cm}} v_3) \sqrt{2\varepsilon(1+\varepsilon)}.
\end{aligned}
\tag{A.1}
$$

with q_{cm} and ε fixed in our experiment, and:

$$
\begin{aligned}
K_2 &= e^6 \frac{q_{cm}}{\tilde{Q}^2} \frac{2m_p}{1-\varepsilon} \sqrt{\frac{2E_q}{E_q + m_p}} \\
E_q &= \sqrt{m_p^2 + q_{cm}^2} \\
v_1 &= sin(\theta_{cm})(w'' sin(\theta_{cm}) - k_T w' cos(\theta_{cm}) cos(\varphi_{cm})) \\
v_2 &= -(w'' sin(\theta_{cm}) cos(\varphi_{cm}) - k_T w' cos(\theta_{cm})) \\
v_3 &= -(w'' sin(\theta_{cm}) cos(\theta_{cm}) cos(\varphi_{cm}) - k_T w'(1 - sin^2(\theta_{cm}) cos^2(\varphi_{cm}))) \\
k_T &= \tilde{Q} \sqrt{\frac{\varepsilon}{2(1-\varepsilon)}} \\
w &= \left[-q'_{cm} \left(\frac{1}{\mathbf{p} \cdot \mathbf{q'}} + \frac{1}{\mathbf{k} \cdot \mathbf{q'}} \right) \right]_{q'_{cm}=0} \\
w' &= \left[q'_{cm} \left(\frac{1}{\mathbf{k'} \cdot \mathbf{q'}} + \frac{1}{\mathbf{k} \cdot \mathbf{q'}} \right) \right]_{q'_{cm}=0} \\
w'' &= w q_{cm} - w' \sqrt{\tilde{k}'^2_{cm} - k_T^2}.
\end{aligned}
\tag{A.2}
$$

Appendix B

Spin GPs contribution to the structure functions according to the DR model

From equations 1.37a and 1.37b one observes that $P_{LL} - P_{TT}/\epsilon$ is directly proportional to $\alpha_E(Q^2)$ if one neglects its spin-GP contribution, which is entirely contained in P_{TT}. Figure B.1 shows the P_{TT} value with respect to Q^2 according to the DR model, it reaches a maximum of $\approx -2~GeV^{-2}$ which is, according to our extractions, a small part of $P_{LL} - P_{TT}/\epsilon$. This explains the similar behaviors of $P_{LL} - P_{TT}/\epsilon$ and $\alpha_E(Q^2)$.

According to the DR model, the spin-GP contribution to P_{LT} is more important. In figure B.1 the value of $K_{spin} \cdot P^{(01,01)1}(q_{cm})$ is plotted versus Q^2 (K_{spin} being defined as the coefficient multiplying the spin GP in P_{LT} in equation 1.37c, i.e. $K_{spin} = 3G_M \widetilde{Q} q_{cm}/2\widetilde{q}_{cm}^0$).
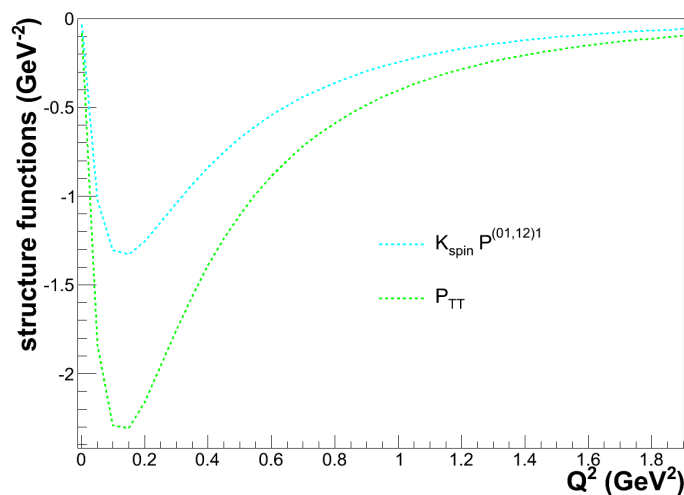

Figure B.1: DR model predicted value of $K_{spin}P^{(01,01)1}(q_{cm})$ and P_{TT}.

Appendix C

Radiative corrections to $ep \rightarrow ep\gamma$

This appendix gathers the mathematical expression of δ-correction terms and the corresponding diagrams. All formulas are taken from [92].

C.1 δ_r: Electron bremsstrahlung

δ_r is the correction term for a supplementary real photon. The considered diagrams are represented in figure C.1.
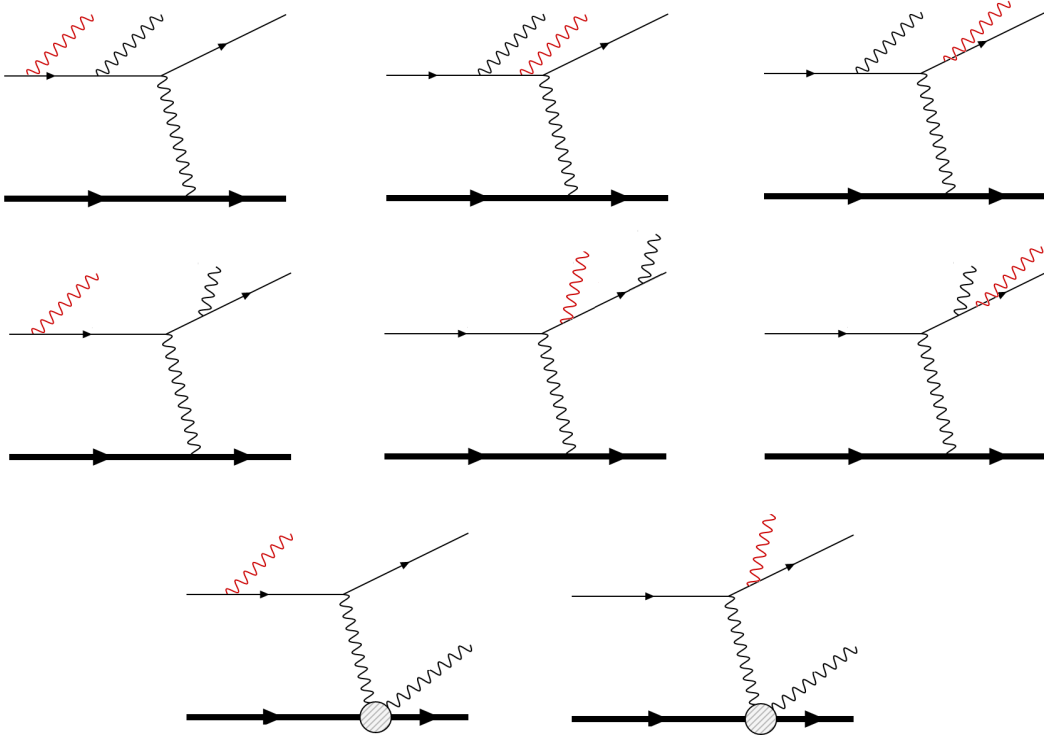

Figure C.1: Diagrams accounted in the δ_r correction term, where one supplementary real photon (red) is produced.

The soft-photon correction term is:

$$\delta_{r2} = \frac{\alpha_{QED}}{\pi}\left(-\frac{1}{2}ln^2\left(\frac{\widetilde{E}_e}{\widetilde{E}'_e}\right) + \frac{1}{2}ln^2\left(\frac{Q^2}{m_e^2}\right) - \frac{\pi^2}{3} + Sp\left(cos^2\left(\frac{\widetilde{\theta}_e}{2}\right)\right)\right), \qquad \text{(C.1)}$$

with $Sp()$ the Spence function. $\widetilde{E}_e$, $\widetilde{E}'_e$ and $\widetilde{\theta}_e$ are respectively the energies of incoming and outgoing electrons and the polar angle of the outgoing electron defined in a particular frame. The considered frame depends on the experiment, i.e. elastic experiment, $(ep \rightarrow ep\gamma)$ with photon-detection experiment or $(ep \rightarrow ep\gamma)$ with proton-detection experiment. In our case:

$$
\begin{array}{lcl}
\widetilde{E}_e & = & \frac{m_p}{M_{m2}}\left(E_e - \frac{Q^2}{2m_p} - \frac{\mathbf{k.p'}}{m_p}\right) \\
\widetilde{E}'_e & = & \frac{m_p}{M_{m2}}\left(E'_e + \frac{Q^2}{2m_p} - \frac{\mathbf{k'.p'}}{m_p}\right) \\
sin^2(\widetilde{\theta}_e/2) & = & \frac{E_e E'_e}{\widetilde{E}_e \widetilde{E}'_e}sin^2(\theta_e/2) \\
M_{m2} = 2 \cdot \Delta E_s.
\end{array}
\qquad \text{(C.2)}
$$

with ΔE_s defined in equation 5.3.

C.2 δ_{vac} and δ_{ver}: supplementary virtual photon
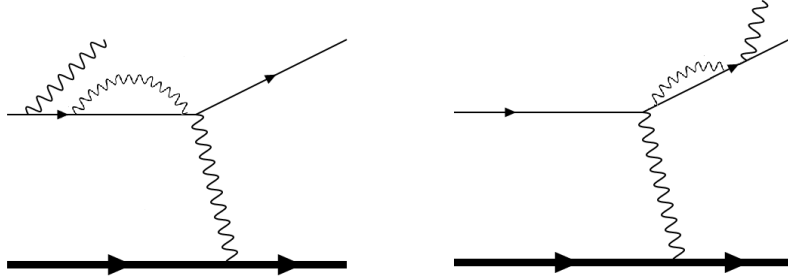

Figure C.2: Electron self-energy diagrams.

The vacuum polarization process, presented in figure 5.2 leads to the following correction term:

$$\delta_{vac} \quad = \quad \frac{\alpha_{QED}}{\pi}\frac{2}{3}\left(-\frac{5}{3} + ln\left(\frac{Q^2}{m_e^2}\right)\right). \qquad \text{(C.3)}$$

The vertex process from figure 5.3 leads to δ_{ver}:

$$\delta_{vertex} \quad = \quad \frac{\alpha_{QED}}{\pi}\left(\frac{3}{2}ln\left(\frac{Q^2}{m_e^2}\right) - 2 - \frac{1}{2}ln^2\left(\frac{Q^2}{m_e^2}\right) + \frac{\pi^2}{6}\right). \qquad \text{(C.4)}$$

C.3 δ_{vac} and δ_{ver}: proton-side correction

This correction is described through two terms which also take into account the two-photon exchange process (direct and crossed) :

$$\delta_1 \quad = \quad \frac{2\alpha_{em}}{\pi}(ln(\frac{4*(\Delta E_s)^2}{Q^2 x})ln(\eta) + Sp(1 - \frac{\eta}{x}) - Sp(1 - \frac{1}{\eta x}) \qquad (C.5)$$

$$
\begin{aligned}
\delta_2^{(0)} \quad = \quad & \frac{\alpha_{em}}{\pi}(ln(\frac{4*(\Delta E_s)^2}{M_N^2})(\frac{E_N'}{|\vec{P}_N'|}ln(x) - 1) + 1 \\
& + \frac{E_N'}{|\vec{P}_N'|}(-\frac{1}{2}ln^2(x) - ln(x)ln(\frac{\rho^2}{M_N^2}) + lnx - Sp(1 - \frac{1}{x^2}) + 2Sp(-\frac{1}{x}) + \frac{\pi^2}{6})) \qquad (C.6)
\end{aligned}
$$

With M_N the mass of the baryon (here proton), E_N' ($|\vec{P}_N'|$) the lab energy (momentum) of the recoiling nucleon and:

$\rho^2 = Q^2 + 4M_N^2$

$x = \frac{(Q+\rho)^2}{4M_N^2}$

$\eta = E_e/E_{el}' = 1 + E_e(1 - cos(\theta_e)/M_N$

where E_e, E_{el}' and θ_e are respectively in the lab frame: the energy of the incoming electron, the energy of the elastic outgoing electron and the angle between the outgoing and incoming electrons.

A third term $\delta_2^{(1)}$ also describes the proton-side processes. It is presented in [92] as being about the same order of magnitude than $\delta_2^{(0)}$, i.e. $\approx 0.02\%$ of F^{rad} in our kinematics. $\delta_2^{(1)}$ was not determined in our analysis but its omission is considered in the error budget on F^{rad}.

Appendix D

Supplementary studies for the LEX fit

D.1   The ΔM stability with respect to q'_{cm}

Figure D.1 shows some typical ΔM behaviors versus q'_{cm}, it allows to check if ΔM is independent of q'_{cm} as required by the LEX fit, and if the points measured by different settings are in agreement.

A Ψ_0 value is obtained by averaging these measurements, if and only if the bins pass the mask selection (described in section 5.5.2).

For the first two plots at the top of figure D.1, none of the measurements satisfy the mask selection and no Ψ_0 is calculated. This signifies that, according to the DR model, the higher orders are not negligible in these bins, and so, one should observe a non-flat q'_{cm} behavior of ΔM.

For the two plots in the middle of figure D.1, the Ψ_0 value is not calculated from all the data, the high q'_{cm} are rejected by the mask selection; the red band corresponds to the averaging of the three different measurements at $q'_{cm} = 62.5 \ MeV/c$.

For the two last plots at the bottom of figure D.1 every measurement passes the mask selection, this signifies that according to the DR model one can neglect the higher orders in those particular bins, and that the different ΔM points should not depend on q'_{cm}.

Globally on these six plots, the points measured by different settings are in good agreement. The absence of q'_{cm}-dependence of ΔM is hard to judge by eye, and for this we rely on the theoretical criterion of our mask selection.

D.2   LEX fits with various subgroups of data

In section 3.3 we explained the importance of choosing the analyzed phase space and we detailed the reasons that motivated our choices. In this section we observe the consequences of ignoring these recommendations, it is illustrated in tables D.2-a and D.2-b.

Table D.2-a presents the results obtained by considering each setting separately. One observes that the setting INP, which is more sensitive to P_{LT} gives a result close to the measured one for this structure function. on the contrary, the setting OOP is more sensitive to $P_{LL} - P_{TT}/\epsilon$ and governs the extraction of this structure
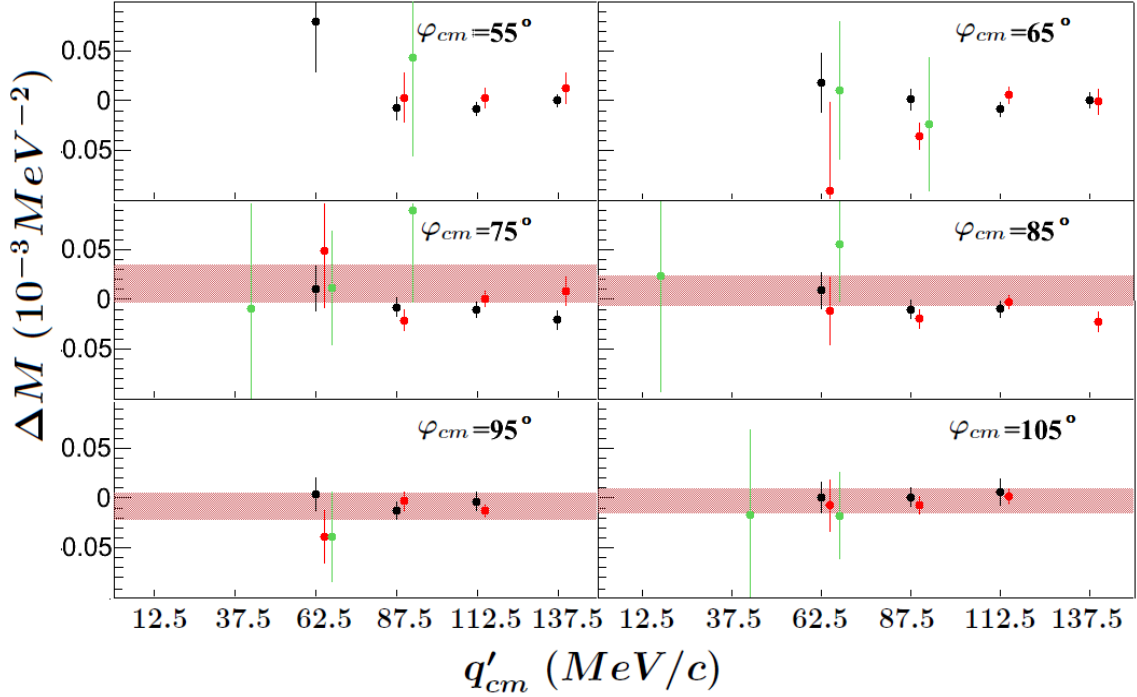
Figure D.1: Measured ΔM with respect to q'_{cm} for six selected bins; $cos(\theta_{cm}) = -0.675$ and $55° \leq \varphi_{cm} \leq 105°$. The points are from different settings: INP (black), OOP(red) and LOW+LOW-bis (green). The light-red area corresponds to the quantity $\Psi_0 \pm \Delta\Psi_0$ fitted in the $(cos(\theta_{cm}), \varphi_{cm})$-bin . Some points are shifted in q'_{cm} for visibility.

function. The OOP-forward setting presents data collected afterwards, with a low statistics and gives results with high statistical errors. The two settings at low q'_{cm} are clearly less sensitive to the GP effect and are individually not relevant for a structure-function extraction.

Settings	LOW	LOW-bis	INP	OOP	OOP-forward
q'_{cm}-range (MeV/c)	[0;75]	[0;75]	[50;125]	[50;125]	[50;125]
n.d.f	931	797	347	265	80
$\chi_{LEX}^{2,reduced}$	1.08	1.03	1.31	1.37	1.01
$P_{LL} - P_{TT}/\epsilon$ (GeV^{-2})	44.51 ± 5.27	22.77 ± 4.98	19.44 ± 1.10	18.00 ± 0.74	18.22 ± 8.11
P_{LT} (GeV^{-2})	-12.38 ± 2.94	-1.20 ± 2.47	-3.41 ± 0.35	-7.81 ± 1.15	-9.68 ± 4.44

Table D.2-a: LEX fits of structure functions for the five settings separately, the q'_{cm}-range is the one covered by each setting. The errors on the structure functions are statistical.

Table D.2-b presents the results obtained by considering each q'_{cm}-bin separately. It illustrates the irrelevance of the low q'_{cm} for a LEX fit and the importance of gathering the high-q'_{cm} data; by taking each q'_{cm} individually the results disagree.

q'_{cm} (MeV/c)	12.5	37.5	62.5	87.5	112.5
Settings used	LOW and LOW-bis	LOW and LOW-bis	All	INP, OOP and OOP-forward	INP, OOP and OOP-forward
n.d.f	447	762	886	447	123
$\chi^{2,reduced}_{LEX}$	1.23	1.35	1.14	1.74	1.14
$P_{LL} - P_{TT}/\epsilon$ (GeV^{-2})	419.34 $\pm$213.49	58.25 $\pm$7.56	25.65 $\pm$1.91	16.56 $\pm$0.86	14.84 $\pm$0.91
P_{LT} (GeV^{-2})	-93.14 $\pm$93.14	-23.31 $\pm$3.53	-6.74 $\pm$0.98	-0.90 $\pm$0.47	-7.38 $\pm$0.56

Table D.2-b: LEX fits of structure functions for the five q'_{cm} bins separately. The value of q'_{cm} is the one at the center of the bin. The errors are statistical.

We believe that the best fit is the one which gathers all data for the reasons explained in section 3.3.

One can do two side remarks about the numbers in table D.2-b:

- for each bin in q'_{cm}, the number of cross-section points in $(cos(\theta_{cm}), \varphi_{cm})$ is given by $n.d.f + 2$. These cross-section points are the ones passing the mask criterion, and they are setting-averaged, as indicated in the table.

- the sum of the five numbers $\sum(n.d.f. + 2)$ is equal to 2675, which is therefore our total number of setting-averaged cross section points. Figure D.1 allows to visualize how several individual data points, at different q'_{cm}, are gathered together in order to yield only one Ψ_0 data point. This explains why our nominal LEX fit (section 5.5.3) uses 946 data points, in terms of Ψ_0.

Appendix E

Gradient selection

The gradient selection is essentially designed to follow the acceptance edges in $(cos(\theta_{cm}), \varphi_{cm})$, which themselves depend on q'_{cm}. To test if a bin (i) is kept we compare its BH+B cross-section with the one of the four direct neighbour-bins ($j = 1 \rightarrow 4$) in the $(\varphi_{cm}, cos(\theta_{cm}))$-plane and with the one of the four bins ($k = 1 \rightarrow 4$) in the diagonal directions. The eight conditions to satisfy are:

$$\frac{\sigma_i^{BH+B} - \sigma_{j=1\rightarrow 4}^{BH+B}}{1} < 0.4 \ (pb.MeV^{-1}.sr^{-2})$$
$$\frac{\sigma_i^{BH+B} - \sigma_{k=1\rightarrow 4}^{BH+B}}{\sqrt{2}} < 0.4 \ (pb.MeV^{-1}.sr^{-2}) \tag{E.1}$$

This design is the best if one wants to respect our specific acceptance; applying a cut on relative cross-section differences would generate complicated and unwanted shapes. Figure E.1 shows the effect of the selection on the data.
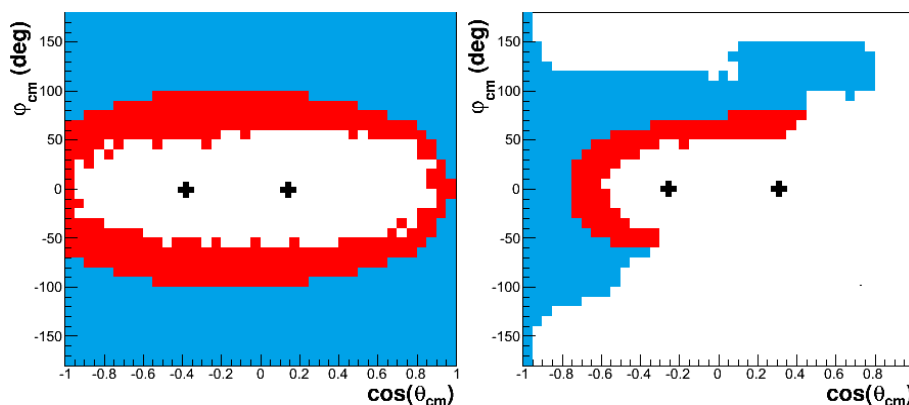

Figure E.1: Bins, in blue, that satisfy the gradient selection in the $(\varphi_{cm}, cos(\theta_{cm}))$-plane at $q'_{cm} = 37.5 \ MeV/c$ (left) and $q'_{cm} = 112.5 \ MeV/c$ (right). The bins in red are rejected by the selection, they are close to the acceptance edges. The black crosses show the exact position of the Bethe-Heitler peaks.